

Heat and mass transfer improvement using self-rewetting nanofluids

Ibrahim Zaaroura

▶ **To cite this version:**

Ibrahim Zaaroura. Heat and mass transfer improvement using self-rewetting nanofluids. Thermics [physics.class-ph]. Université Polytechnique Hauts-de-France; Institut National des Sciences Appliquées Hauts-de-France, 2020. English. NNT : 2020UPHF0024 . tel-03383929

HAL Id: tel-03383929
https://uphf.hal.science/tel-03383929

Submitted on 18 Oct 2021

HAL is a multi-disciplinary open access archive for the deposit and dissemination of scientific research documents, whether they are published or not. The documents may come from teaching and research institutions in France or abroad, or from public or private research centers.

L'archive ouverte pluridisciplinaire **HAL**, est destinée au dépôt et à la diffusion de documents scientifiques de niveau recherche, publiés ou non, émanant des établissements d'enseignement et de recherche français ou étrangers, des laboratoires publics ou privés.

Thèse de Doctorat

Présentée pour obtenir le grade de Docteur de L'UNIVERSITE POLYTECHNIQUE HAUT-DE-FRANCE Et L'INSA HAUTS-DE-FRANCE

Mécanique-Thermique-Energétique-Acoustique

Présentée et soutenue par **Ibrahim ZAAROURA**

Le 25 /11/2020, à l'UPHF

Ecole doctorale :

Sciences Pour l'Ingénieur (SPI)

Equipe de recherche, Laboratoires :

Laboratoire d'Automatique, de Mécanique et d'Informatique Industrielles et Humaines (LAMIH-UMR CNRS 8201)

Institut d'Electronique de Microélectronique et de Nanotechnologie (IEMN-UMR CNRS 8520)

Heat and mass transfer improvement using self-rewetting nanofluids

JURY

Président du jury

- Khellil SEFIANE, Professeur, Université d'Edinbourg (UK).

Rapporteurs

- Rachid BENNACER, Professeur à l'ENS de Paris-Saclay Cachan.
- Gilles DESPAUX, Professeur à l'université de Montpellier.

Examinateurs

- Khellil SEFIANE, Professeur, Université d'Edinbourg (UK).
- Vincent THOMY, MCF HDR, IEMN – Université de Lille.
- Souad HARMAND, Professeur, UPHF (**Directeur de thèse**)
- Julien CARLIER, Professeur, UPHF (**Co-directeur de thèse**)

Invites

- Bertrand NONGAILLARD, Professeur émérite, IEMN/UPHF.
- Aurèlie FASQUELLE, Dr. Ingénieur aérothermique, Jeumont Electric.

Thèse de Doctorat

Présentée pour obtenir le grade de Docteur de L'UNIVERSITE POLYTECHNIQUE HAUT-DE-FRANCE Et L'INSA HAUTS-DE-FRANCE

Mécanique-Thermique-Energétique-Acoustique

Présentée et soutenue par **Ibrahim ZAAROURA**

Le 25 /11/2020, à l'UPHF

Ecole doctorale :

Sciences Pour l'Ingénieur (SPI)

Equipe de recherche, Laboratoires :

Laboratoire d'Automatique, de Mécanique et d'Informatique Industrielles et Humaines (LAMIH-UMR CNRS 8201)

Institut d'Electronique de Microélectronique et de Nanotechnologie (IEMN-UMR CNRS 8520)

Amélioration du transfert de chaleur et de masse à l'aide de nanofluides auto-réhumidifiants

JURY

Président du jury

- Khellil SEFIANE, Professeur, Université d'Edinbourg (Royaume-Uni).

Rapporteurs

- Rachid BENNACER, Professeur à l'ENS de Paris-Saclay Cachan.
- Gilles DESPAUX, Professeur à l'université de Montpellier.

Examinateurs

- Khellil SEFIANE, Professeur, Université d'Edinbourg (Royaume-Uni).
- Vincent THOMY, MCF HDR, IEMN – Université de Lille.
- Souad HARMAND, Professeur, UPHF (**Directeur de thèse**)
- Julien CARLIER, Professeur, UPHF (**Co-directeur de thèse**)

Invites

- Bertrand NONGAILLARD, Professeur émérite, IEMN/UPHF.
- Aurèlie FASQUELLE, Dr. Ingénieur aérothermique, Jeumont Electric.

Abstract

Thermal management is currently a major issue in many sectors of industry. Heat transfer devices (like Heat Pipes, Heat exchangers…) are integrated systems that use transfer modes by convection, evaporation and condensation. The efficiency of heat exchange can be improved by using a new nanotechnology method known as nanofluids. Nanofluids are suspensions of nano-size particles (from 2 to 100nm) in the fluids. This improvement is due to the significant increase in the effective conductivity in the range 10-50% as well as their convective heat transfer coefficients. However, limitations related to the phenomena of nanoparticle, sedimentation and aggregation appear during different phases. In this project, in order to optimize the performance and stability of nanofluids, two different methods were used: an optical one coupled to an infrared thermography method and a high frequency acoustic method. The selection of nanoparticles was based on their thermal performance during evaporation of sessile droplets using a Kruss system, under same conditions and at different concentrations. Thus, high frequency acoustic waves, at the surface, make it possible to analyze the stabilities of nanoparticles during its evaporation where these particles are in suspension with base fluids such as ionized water, self-rewetting binary mixture (To improve the circulation of fluids inside heat pipes thanks to their physical properties like thermal Marangoni, concentration Marangoni, capillary...). The selected nanofluids will be used later to analyze experimentally their performance on two-phase capillary fluid loop heat transfer devices and in micro-channel heat exchangers by finding and calculating the thermal resistance of the system, convection heat transfer coefficient and wall temperature.

Keywords: Thermal management, Heat pipes, Micro Heat Exchangers, Self-rewetting nanofluids, Heat transfer, Droplets Evaporation, Acoustic field,

Résumé

La gestion thermique est actuellement un enjeu majeur dans de nombreux secteurs industriels. Les dispositifs de transfert de chaleur (comme les caloducs) sont des systèmes intégrés qui utilisent des modes de transfert par convection, évaporation et condensation. L'efficacité de l'échange thermique peut être améliorée en utilisant une nouvelle méthode de nanotechnologie connue sous le nom de nanofluides. Les nanofluides sont des suspensions de particules nanométriques (de 2 à 100 nm) dans les fluides. Cette amélioration est due à l'augmentation significative de la conductivité effective dans la plage de 10 à 50% ainsi qu'à leurs coefficients de transfert de chaleur par convection. Cependant, des limitations liées aux phénomènes de nanoparticules, de sédimentation et d'agrégation apparaissent au cours de différentes phases. Dans ce projet, afin d'optimiser les performances et la stabilité des nanofluides, deux méthodes différentes ont été utilisées: une optique couplée à une méthode de thermographie infrarouge et une méthode acoustique à haute fréquence. La sélection des nanoparticules a été basée sur leurs performances thermiques lors de l'évaporation de gouttelettes sessiles à l'aide d'un système Kruss, dans les mêmes conditions et à des concentrations différentes. Ainsi, des ondes acoustiques haute fréquence, en surface, ont permis d'analyser la stabilité de nanoparticules lors de l'évaporation où ces particules sont en suspension avec des fluides de base tels que l'eau ionisée, des mélanges binaires auto-réhumidifiant (Pour améliorer la circulation des fluides à l'intérieur caloducs grâce à leurs propriétés physiques comme les phénomènes Marangoni thermique, Marangoni de concentration, capillaires ...). Les nanofluides sélectionnés seront utilisés par la suite pour analyser expérimentalement leurs performances sur les dispositifs de transfert de chaleur à boucle de fluide capillaire biphasé et dans les échangeurs de chaleur à micro-canaux en trouvant et en calculant la résistance thermique du système, le coefficient de transfert de chaleur par convection et la température de paroi.

Mots clés: Gestion thermique, Caloducs, Micro échangeurs de chaleur, Nanofluides auto-réhumidifiants, Transfert de chaleur, Évaporation des gouttes, Champ acoustique,

Acknowledgments

The author would like to acknowledge all the people who supported him throughout his PhD study.

Before presenting my work, I would first like to thank all members of the jury for having agreed to judge and attend the presentation of this work. Thank you to the rapporteurs, Professors Rachid Bennacer and Gilles Despaux for having carefully analyzed my work. Thanks to professors Souad Harmand, Khellil Sefiane, Bertrand Nongaillard, Vincent Thomy, Julien Carlier and Aurélie Fasquelle for reviewing my work.

The author wishes to express his appreciation to his major directors, Prof. S. Harmand, Dr. J. Carlier, Dr. M. Toubal and Prof. B. Nongaillard for their extensive advice, guidance, and support throughout his doctoral program. They have been a professors, advisers and a friends. Dr. A. Fasquelle, from Jeumont Electric Company, should be acknowledged for this contribution which can be seen in various work because of their financial support for this PhD project as well as the French government, FEDER and the Haut-de France region.

The author also wishes to gratefully acknowledge Mr. J. Schiffler and Mr. F. Delcourt for their helps with the experimental installation at LAMIH laboratory. Also wishes to Dr. R. Boukherroub, Dr. D. Guerin, Dr. V. Thomy and Dr. P. Tilmant for their contributions and training inside the Clean Room based in Lille at IEMN laboratory.

Appreciation is also extended to the authors' brother (Mohammad), sisters (Yasmeen and Dana), relatives and friends for their love and encouragement.

Finally this study is dedicated to the author's parents, Mr. and Mrs. Ghaleb and Nadia Zaaroura. Without their continued love, emotional support, understanding and prayers, this project could not have been completed.

Table of contents

ABSTRACT ..... **i**

ACKNOWLEDGMENTS ..... **ii**

TABLE OF CONTENTS ..... **iv**

LIST OF TABLES ..... **vii**

LIST OF FIGURES ..... **viii**

NOMENCLATURE ..... **xiii**

GENERAL INTRODUCTION **1**

GENERAL INTRODUCTION 2
RESEARCH OBJECTIVES AND THESIS OUTLINE 4

CHAPTER .I LITERATURE REVIEW **6**

I.1 NANOFLUIDS OVERVIEW 7
I.1 Definition *7*
I.2 PROPERTIES 8
I.2.1 Thermal conductivity *8*
I.2.2 Dynamic viscosity *9*
I.2.3 Density and specific heat *9*
I.3 TYPES OF NANOPARTICLES 10
I.4 NANOFLUID PREPARATION 10
I.5 INFLUENCE OF NANOFLUIDS ON THERMOPHYSICAL PROPERTIES 10
I.5.1 Effect of the volume concentration of nanoparticles *11*
I.5.2 Effect of the type of nanoparticles *11*
I.5.3 Effect of temperature *12*
I.6 ADVANTAGES AND DISADVANTAGES OF NANOFLUIDS 13
I.6.1 Advantages of nanofluids [47-49] *13*
I.6.2 Disadvantages of nanofluids [50-53] *13*
I.7 NANOFLUIDS FIELDS OF APPLICATION 14
I.7.1 Heat transfer mechanism associated with cooling systems *14*
a- Conductive transfer 14
b- Convective transfer 15
c- Droplets evaporation-liquid/vapor phase change 15
I.7.2 Main cooling systems used in power electronics *18*
1- Active cooling systems 18
1.1 Active direct cooling 18
1.2 Active indirect cooling 20
2- Passive cooling systems 20
2.1 Passive direct cooling 21
2.2 Passive indirect cooling 22
I.7.3 Passive phase change cooling systems - Heat pipes *23*
1.7.4 Definition and operating principle *23*

1.7.5 Types of heat pipes *24*
I.8 HEAT PIPES PERFORMANCE USING NANOFLUIDS 26
1.9 CONCLUSION 30

CHAPTER .II NANOFLUIDS SYNTHESIS AND THERMOPHYSICAL PROPERTIES: ACOUSTIC AND THERMOGRAPHY METHODS 32

II. 1 INTRODUCTION 33
II. 2 INFRARED AND ACOUSTIC METHOD TO TRACK THE DYNAMIC DEPOSITION OF COPPER OXIDE NANOPARTICLES 34
II.2.1 Methodology and experimental setup *35*
II.2.1.1 Infrared and optical measurements 35
II.2.1.2 Acoustic measurements 38
II.2.2 Experimental results *43*
II.2.2.1 Calibration of the acoustic measurement method: Water as a reference liquid 44
II.2.2.2 Optical, infrared and acoustic measurements of CuO-water droplet at ambient temperature 45
II.2.2.3 Effect of substrate temperature on nanoparticles deposition 51
II. 3 DYNAMIC VISCOSITY MEASUREMENTS OF GOLD NANOFLUIDS USING HIGH FREQUENCY ACOUSTIC METHOD (≈1GHz) 56
II.3.1 Experimental setup *57*
II.3.2 Results and discussion *61*
II.3.2.1 Calibration of the acoustic measurements method: Water as a reference liquid 61
II.3.2.2 Values of dynamic viscosity of gold nanofluid during the evaporation of 4%Cv Au-water droplet .62
II.3.2.3 Viscosity measurements as function of gold nanoparticles concentrations 65
II. 4 CONCLUSION 67

CHAPTER .III EXPERIMENTAL STUDIES ON EVAPORATION KINETICS OF GOLD NANOFLUIDS DROPLETS 69

III.1 INTRODUCTION 70
III.2 METHODOLOGY AND EXPERIMENTAL SETUP 71
III.2.1 Infrared and optical measurements *72*
III.2.2 Acoustic measurements *73*
III.3 EXPERIMENTAL RESULTS 74
III.3.1 Infrared and optical investigations *74*
III.3.1.1 Au nanofluid (1% C_v; 0.1mM PBS, reactant free)-Water mixture, Particle size effects 74
III.3.1.2 Au nanofluid (1% C_v; Citrate Capped-PBS)-Water mixture, Citrate effects 79
III.3.2 Acoustic investigations: Gold nanoparticles stability during droplet evaporation at ambient temperature *82*
III.4 CONCLUSION 86

CHAPTER .IV THERMAL PERFORMANCES OF TWO-PHASE HEAT TRANSFER AND MICRO HEAT EXCHANGERS DEVICES USING SELF-REWETTING NANOFLUIDS 88

IV.1 INTRODUCTION 89
IV.2 THERMAL PERFORMANCE OF TWO-PHASE HEAT TRANSFER DEVICES 90
IV.2.1 Experimental setup *90*
IV.2.1.1 Working fluids: 90
IV.2.1.2 Procedure: 91
IV.2.1.3 Error analysis 92
IV.2.1.3 Porous media properties 93

IV.2.1.4 Thermal resistance: 93
IV.2.2 Experimental results and discussion 93
IV.2.2.1 Heat transfer characteristics 93
IV.2.2.2 Vapor pocket dynamics 95
IV.3 THERMAL PERFORMANCES OF A MICRO HEAT EXCHANGERS USING NANOFLUID AND SELF-REWETTING FLUID 99
IV.3.1 Experimental method 99
IV.3.1.1 Polydimethylsiloxane (PDMS) - based microchannel device, microfabrication and experimental facility 99
IV.3.1.2 Microfabrication of Polydimethylsiloxane (PDMS) microchannel 100
IV.3.1.3 Surface emissivity measurements of ITO coated glass and PDMS for infrared thermography 101
IV.3.1.4 Working fluids used in the experiment 103
IV.3.2 Data reduction 105
IV.3.3 Results and discussion 107
IV.3.3.1 System calibration: Water as a reference 109
4.2 Gold nanofluid and Butanol self-rewetting liquid as a working fluids 110
IV.4 CONCLUSION 114
CHAPTER .V GENERAL CONCLUSION AND PERSPECTIVES 116
V.1 CONCLUSION AND PERSPECTIVES 117
REFERENCES 120
ANNEX A 131
ANNEX B 134
ANNEX C 136
LIST OF PUBLICATIONS: 137

List of tables

Table I.1. Comparison of thermal conductivities of some fluids and materials at 20 ° C. [31] 7
Table I.2. Maxwell and Hamilton-Crosser models, "f" for the fluid and "p" for the particles. 8
Table I.3. Models used to calculate the viscosity of nanofluids. 9
Table II.1. Physical properties of water, copper oxide and silicon at 22 °C. 45
Table II.2. Volume fraction percentage of CuO nanoparticles as a function of the acoustic reflection coefficient. 49
Table II.3. Influence of the substrate temperature on the intensity density of the deposited nanoparticles and their deposition time. 52
Table II.4. Lifetime of the convection cells as a function of the substrate temperature. 54
Table II.5. Physical properties of silicon and water at ambient temperature. [110] 56
Table II.6. Percentage of deposited particles above the transducer as a function of time. 66
Table III.1. Properties of prepared gold nanofluids. 71
Table III.2. Lifetime of the convection cells at 77 °C substrate temperature of pure water, 5 nm Au-water and 10 nm Au-water nanofluids. 78
Table IV.1. Working fluids with concentrations used. 91
Table IV.2. Porous media properties. 93
Table IV.3. Thermal conductivity of gold nanofluid at different temperatures. 97
Table IV.4. Contact angle measurements. 98
Table IV.5. Characteristics dimensions of the different components of the microchannel device. 100
Table IV.6. Thermophysical properties of the working fluids at ambient temperature. [126, 127] 103
Table IV.7. Summary of measurements uncertainties. 107
Table IV.8. Thermal conductivity of water and gold nanofluids as a function of volume concentrations and at different temperatures. 112

List of figures

General Introduction

Figure 1. (a) LHP design (b) Capillary evaporator. 3

Chapter. I

Figure I.1. The effect of volume concentration on thermal conductivity of Al_2O_3 /water nanofluids. [44] 11

Figure I.2. Effect of particle types on the thermal conductivity of nanofluids. [45] 12

Figure I.3. Effect of temperature on the thermal conductivity of nanofluids. [46] 13

Figure I.4. Contact angle of a liquid droplet wetted to a rigid solid surface. [59] 16

Figure I.5. The evolution of parameters ((i) contact angle (ii) drop diameter (iii) drop volume) during evaporation of a water-ethanol mixture drop as a function of time. [60] 16

Figure I.6. (a) Liquid flow patterns in an evaporating droplet on a heated substrate. A stable Marangoni flow forms in the droplet. (b) Liquid flow patterns in an evaporating droplet on an unheated substrate. Evaporation induced radial flow is the dominant flow. [62] 17

Figure I.7. Classification of active cooling systems. 18

Figure I.8. Principle of cooling by spraying with dielectric liquid. [67] 19

Figure I.9. Principle of jet cooling. [68, 4] 19

Figure I.10. Classification of passive cooling systems. 21

Figure I.11. Principle of free boiling cooling. [69] 22

Figure I.12. Heat pipe working principle. [71] 24

Figure I.13. Diagram illustrating a micro-pipeline. [73] 25

Figure I.14. Schematic diagram of the two-phase capillary pumping loop. [75] 26

Figure I.15. Photograph of the four miniature heat pipes. 28

Figure I.16. Wall temperature distributions of heat pipes by air cooling. 29

Figure I.17. Thermal resistance of heat pipes by air cooling. 29

Chapter. II

Figure II.1. (a) Schematic illustration of the experimental setup for optical and infrared measurements. (b) Contrast image analysis of the CuO nanoparticles on the top side of the glass substrate using ImageJ software. 37

Figure II.2. Multilayer diagram of a piezoelectric transducer. 38
Figure II.3. Transducer fabrication process flow chart. 39
Figure II.4. Image of a network of transducers of different diameters obtained by optical microscopy. .. 39
Figure II.5. Parameter S11 measured with the network analyzer, (a) real part (b) imaginary part. 40
Figure II.6. Impulse response S_{11} (t). 41
Figure II.7. Zoom around the longitudinal acoustic wave resonance of the transducer. 42
Figure II.8. Schema of the experimental setup of acoustic measurements. 43
Figure II.9. Contact angle evolution of 0.05wt % CuO-water nanofluid droplet on a non-heated substrate at 22°C. 44
Figure II.10. Reflection coefficient evolution of a 6 µL pure droplet of water during evaporation process at 22°C. 45
Figure II.11. Mean values of the precipitated CuO nanoparticles on the hydrophobic glass substrate at 22°C. 46
Figure II.12. Dried deposits of 0.05wt % CuO-water nanofluid droplet on a non-heated substrate (22°C) with the distribution surface profile using ImageJ software. 47
Figure II.13. Reflection coefficient evolution of 0.05wt % CuO-water nanofluid droplet on a non-heated substrate (T=22°C). 47
Figure II.14. Dried deposits of 0.05wt % CuO-water droplet during acoustic measurements. 48
Figure II.15. Volume fraction percentage of CuO nanoparticles on the transducers during evaporation process 49
Figure II.16. (a) Periodic unit cell at the interface; (b) Unit cell representation of matrix periodic structure (water and copper oxide particles). 50
Figure II.17. Comparison between the kinetics of the Young Modulus $\boldsymbol{Eeff}$ obtained from a finite element model and the Young modulus $\boldsymbol{Enf}$ calculated from the simple mixed rules. 51
Figure II.18. Mean values of the CuO nanoparticles precipitation on the hydrophobic glass substrate during droplet evaporation at different surface temperatures (60, 80 and 90°C). 51
Figure II.19. $\boldsymbol{t} *$ the percentage of time that CuO nanoparticles begin to deposit on a substrate for different substrate temperatures. 52
Figure II.20. Snapshots from an infrared video of the evaporation process of a CuO-water nanofluid droplets at different substrate temperatures (a) 60°C (b) 80°C (c) 90°C, along with droplet surface temperature distribution profiles. 54

Figure II.21. (a) Dried deposits of 0.05wt % CuO-water nanofluid droplet at different substrate temperatures 60, 80, and 90°C with the CuO distribution using ImageJ software, scale bar from 0 to 256 pixels; (b) Nanoparticles area distribution as surface temperature increased. 55

Figure II.22. Schema of the experimental setup of acoustic measurements. [111] 58

Figure II.23. Rf. magnetron sputtering system with additional blind between substrate and target..... 59

Figure II.24. Parameter S_{11} (f) measured with the network analyzer. 59

Figure II.25. Corresponds to the impulse response $\boldsymbol{S11(t)}$, the time delays $\Delta t/L=1\Delta f/L=92$ ns and $\Delta t/S=1\Delta f/S=133$ ns between them corresponds to the propagation delays of the longitudinal and transverse wave travelling twice the thickness of the wafer. (a) f = [0.3-2 GHz], (b) f = [0.3-0.6 GHz]. 60

Figure II.26. Longitudinal reflection coefficient modulus evolution of pure water droplet during evaporation process at 22°C. 61

Figure II.27. Phase angles evolution of pure water droplet during evaporation process at 22 °C. 62

Figure II.28. Modulus reflection coefficient (r_{LL} and r_{TT}) evolution of 4% C_v Au-water nanofluid droplet on a silicon substrate at room temperature. 63

Figure II.29. Phase angle variation for the longitudinal and shear incident waves of 4 % Cv Au-water nanofluid droplet on a silicon substrate at room temperature. 64

Figure II.30. Shear viscosity variation during the evaporation of 4% C_v Au-water nanofluid droplet on a silicon substrate at room temperature. 65

Figure II.31. Comparison of experimental viscosity of Au-water nanofluid (by acoustic method) to Brinkman and Brownian models at room temperature (±2%). 67

Chapter. III

Figure III.1. Gold nanofluids of different sizes (2, 5 and 10 nm) and coating solutions (PBS and Citrate). 71

Figure III.2. Schema of the experimental setup..... 73

Figure III.3. Schema of the experimental setup of acoustic measurements. 74

Figure III.4. Evolutions of the volume for water and gold nanofluid, with different particle sizes under substrate temperatures (a) at ambient, (b) 55 °C and (c) 77 °C (Annex A), versus time. 75

Figure III.5. Normalized contact angle for water and gold nanofluids during evaporation, with different sizes (5 and 10 nm), at ambient temperature..... 76

Figure III.6. Snapshots from an infrared video of the evaporation process of (a) pure water (b) 5 nm Au-water and (c) 10 nm Au-water nanofluids at 50 % relative humidity and 77 °C surface temperature, 1%C_v. 78

Figure III.7. Evolutions of the volume for water and gold nanofluid (Citrate capping-PBS), with different particle sizes (2.2, 5 and 10 nm) under substrate temperatures (a) at ambient, (b) 55 °C and (c) 77 °C (Annex A), versus time. 79

Figure III.8. Evaporation rate of the citrated gold nanoparticle sizes at different surface temperatures... 80

Figure III.9. Snapshots from an infrared video of the evaporation process of (a) Citrated capping 5 nm Au-water and (b) Citrated capping 10 nm Au-water nanofluids at 50 % relative humidity and *77* °C surface temperature, 1%C_v. 82

Figure III.10. Reflection coefficient evolution of pure droplet (black), Au-PBS and Au-Citrate-PBS during evaporation process at 23°C. 83

Figure III.11. Gold Nanofluid Droplet deposited on silicon substrate and above the transducer (a) At starting point (b) Au-10nm- PBS (c) Au-5nm- PBS (d) Au-2.2nm-Citrate PBS (e) Au-5nm-Citrate PBS (f) Au-10nm-Citrate PBS (Nano particles Final shape pattern on the 250 µm transducer diameter). 85

Figure III.12. Thickness distribution of 5nm gold nanoparticles with 4% C_v, (a) PBS solvent (b) Citrate coating with PBS solvent. 86

Chapter. IV

Figure IV.1. Experimental setup of the evaporation part. 91

Figure IV.2. Experimental setup in real state. 92

Figure IV.3. Wick image. 93

Figure IV.4. Casing temperatures variation for water, self-rewetting fluid (butanol) and gold nanofluid at each input power. 94

Figure IV.5. Thermal resistance for water, butanol self-rewetting and gold nanofluids. 95

Figure IV.6. Comparison of the vapor pocket for water, gold nanofluid and self-rewetting nanofluid. ... 96

Figure IV.7. Surface tension measurements for water, butanol (3% C_v), gold (1% C_v), and a mixture of butanol self-rewetting gold nanofluid (Bu 3%-Au 1% C_v) using KRUSS Pendant method. 98

Figure IV.8. PDMS microchannel, bonded to ITO coated glass. 100

Figure IV.9. Schematic view of integration steps of the PDMS microchannel with the inlet and outlet flow. 101

Figure IV.10. (a) Setup for calibration of surface emissivity and (b) Thermal image from the IR used to measure the emissivity of ITO coated glass and PDMS in reference to the emissivity of the black paint. 102

Figure IV.11. Surface emissivity measurements of ITO/glass and PDMS with increasing temperature. 103

Figure IV.12. Schematic of experimental apparatus. 105

Figure IV.13. Wall temperature measurements obtained by infrared camera for 4 mm thick glass as function of input power. 108

Figure IV.14. Thermal image of the microchannel using infrared camera without liquid flow. 108

Figure IV.15. Axial microchannel temperatures, without fluid, at different input powers (a) T_w=50 °C (b) T_w=70 °C and (c) T_w=90°C. 109

Figure IV.16. Variation of local convective heat transfer coefficient of gold nanofluid (1 and 8% C_v), Butanol (3% C_v) compared to pure water base fluid at each input power along the microchannel length. 112

Figure IV.17. Sequence of optical images that reveal the typical flow regimes of the microchannel. (a) The optical images for pure water flow at P_1 input power (b) The optical images for 1% gold/water nanofluid flow at P_1 input power. 113

Figure IV.18. Variation of local convective heat transfer coefficient of pure water along the microchannel length..... 114

Nomenclature

%wt	Weight Concentration, %
$\overline{ID}$	Mean Intensity Density
$\lvert R \rvert$	Amplitude reflection coefficient
Z	Mechanical Impedance, kg·s.m−2
nf	Nanofluid
p	Particles
w	Water
Z_{nf}	Mechanical Impedance of Nanofluid, kg·s.m−2
Z_s	Mechanical Impedance of Silicon, kg·s.m−2
CA°	Droplet Contact Angle, °
γ	Surface tension, mN·m−1
ρ_{nf}	Density of Nanofluid, kg·m−3
ρ_p	Density of CuO particles, kg·m−3
ρ_ω	Density of water, kg·m−3
E_{nf}	Young Modulus of Water, Gpa
E_{eff}	Effective Young Modulus, Gpa
C	Acoustic Velocity, m·s−1
C_{n_f}	Acoustic Velocity of Nanofluid, m·s−1
∅ %	Particles Volume Fraction Concentration, %
t^*(%)	Nanoparticles Relative Time Percentage to Deposit, %
D*(%)	Percentage Area Distribution of Dried Nanoparticles, %
%Cv	Volume concentration, %
r*	Reflection coefficient
r_{LL}	Longitudinal reflection coefficient
r_{TT}	Shear reflection coefficient

C_L	Longitudinal acoustic velocity, $m.s^{-1}$
C_T	Shear acoustic velocity, $m.s^{-1}$
ω	Pulsation of the incident wave
α_T	Shear attenuation
α_L	Longitudinal attenuation
k_T^*	Complex shear wave number, m^{-1}
k_L^*	Complex longitudinal wave number, m^{-1}
μ_s	Shear viscosity, Pa.s
S_{11}^{el}	Electric reflection
K_{11}	Coupling coefficient of the piezoelectric transducer
S_{11}^{ac}	Contribution of the whole acoustic reflections
Δ_t	Time delay
T_{atm}	Atmospheric Temperature, °C
DSA	Drop shape Analyzer
Au	Gold Nanoparticles
CuO	Copper oxide
PBS	Phosphate-Buffered Saline
PFTS	Perfluorodecyltrichlorosilane
Vi	Initial Volume
CHP	Capillary Heat Pipe
LHP	Loop Heat Pipe
r_p	Pore radius, m
Δh	Hydrostatic pressure, m
φ	Applied power, W
V	Voltage, U
I	Current, A
T_c	Casing temperature, °C
$T_{w,in}$	Inlet wick temperature, °C
R_T	Thermal resistance, °C/W
H	Humidity, %

W_{ch}	Channel width, m
H_{ch}	Channel height, m
L_{ch}	Channel length, m
a	Aspect ratio
ITO	Indium tin oxide
PDMS	Polydimethylsiloxane
ε	Thermal Emissivity
B_i	Biot number
τ_w	Channel wall thickness, m
Q_{eff}	Effective heating power, W
T_w	Outer wall temperature, °C
T_f	Fluid temperature, °C
q(x,y)	Average heat flux, W/m^2
$\dot{m}$	Mass flow rate, kg/s
A	Channel surface area, m^2
$T_{l,out}$	Inlet liquid temperature, °C
$T_{f,out}$	Outlet liquid temperature, °C
T_l	Local liquid temperature, °C
h_{cv}	Convection coefficient, W/k m^2
Nu	Nusselt number
Re	Reynolds number
t	Time, s

General Introduction

General Introduction

Heat transfer engineering is playing an increasingly important role in the advancement of electronics industries, electric motors, batteries, nuclear and automotive (development of electric vehicles and hybrid vehicles) [1-4]. Optimizing the performance of electronic thermal management systems requires to control the heat exchanger conditions in cooling system with internal two-phase flow. In order to satisfy the junction temperature requirements in terms of performance and reliability, improvements in cooling technologies are required.

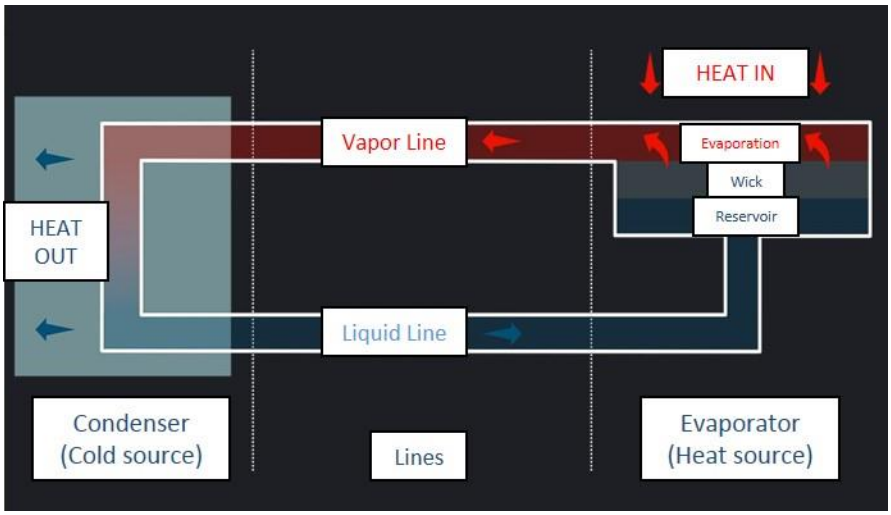
For that reason, a new nanotechnology is used to enhance and improve the heat transfer for better cooling efficiency. This nanotechnology is known as Nanofluids where nanoparticles (such as Copper oxide, Graphene, Silver, Diamond and so on), of nanometric dimensions (1 to 100 nm), are suspended in various base fluids (water, minerals oil, binary mixtures) [5-7]. These nanoparticles have the advantage of improving the heat transfer by absorbing rapidly the high heat fluxes and evacuating them outside the system. This improvement is due to their thermophysical properties which have shown special advantages, such as better stability, greater thermal conductivity, and lower pressure drop [8-11].

Since 1990, several research projects indicated that the addition of small amounts of nanoparticles in liquids could increase significantly the effective conductivity in the range of 10-50% as well as their convective heat transfer coefficients [12-15]. Hence, thermal conductivity has therefore received the closest attention in improving thermal systems. One of the most important applications under investigation nowadays is the study of the characteristics of nanofluids for heat pipes [16-18]. The life time of an integrated circuit (IC) used in electronic devices depends on its operating temperature. This creates a trade-off situation either to enlarge the package to accept additional cooling or to sacrifice the IC lifetime. Among other cooling techniques, heat pipes emerged as the most appropriate technology and cost effective thermal design solution due to its excellent heat transfer capability (high effective thermal conductivity), high efficiency, passive operation and structural simplicity (lower costs).

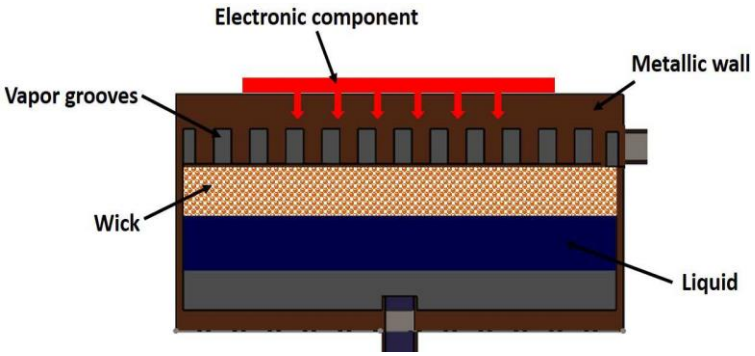
The heat pipe is a vapor-liquid phase change device that transfers heat from a hot side to a colder side using capillary forces generated by a wick or porous material and a working fluid [19, 20].

They are made of a tube, generally a metal one, to achieve the highest thermal conductivity, and partially charged with an operating fluid.

The two main parts of the heat pipes are the evaporator and the condenser, see **Fig. 1**. Two different loops of heat pipes can be used for cooling electronic devices, Capillary Pumped Loop (CPL) and Loop Heat Pipe (LHP). These devices are using the fluid circulation and the vaporization phenomena inside the porous wick to transport large heat load without the need for a mechanical pump [21].



(a)



(b)

Figure 1. (a) LHP design (b) Capillary evaporator.

The evaporator, as shown in Fig. 1(b), which is the major element of such devices, is responsible for the fluid circulation in the complete loop thanks to the capillary pressure generated inside the porous wick.

Research objectives and Thesis outline

Since nanofluids exhibit unprecedented heat transfer properties, they are considered as potential working fluids to use in high heat flux systems. The main objective of this thesis is to find out the best nanoparticles to be used as working fluid in the two-phase heat transfer systems. Nanofluids can increase the thermal conductivity of the fluids compared to the base fluids like water or coolant liquids. Self-rewetting fluids that are binary mixtures can also influence the evaporation performance inside heat pipes. Also, they provide an additional mechanism for the return liquids from the condenser to the evaporator due to the Marangoni forces in addition to capillary forces and gravitational effect. The novelty of this work is to observe the impact of combining both fluids (nanofluids and self-rewetting fluids).

A combination of optical, infrared and acoustic techniques are applied to investigate the performance of different types of nanoparticles. The investigated nanoparticles are copper oxide and gold nanoparticles. The evaporation of sessile droplets, containing copper oxide and gold nanoparticles, has been studied to observe their performance for different sizes, concentrations and surface temperature of the substrate over which the droplet is deposited. Also, the effect of the particle coating is investigated so that to analyze its effect on droplet evaporation. Beside the great impact of nanoparticles on thermal conductivity, their stability showed an important parameter in enhancing heat transfer. For this reason, an acoustic method was used for the first time to analyze the dynamic deposition of nanoparticles over the substrate, during the process of evaporation. This method has also the ability to measure the shear viscosity of nanofluids at different concentrations. These two complementary methods will clarify our research to have enough information of our thermal system.

This dissertation consists of 5 chapters. Chapter 1 summarizes the researcher works on thermal performance by using nanofluids. Chapter 2 introduces a novel combined method of optical, infrared and acoustic techniques to analyze the dynamic deposition of copper oxide nanoparticles during droplet evaporation. The dynamic viscosity of gold nanofluids was measured using acoustic

waves generated by a high frequency transducer. In Chapter 3, an experimental investigation of gold nanofluids, during droplet evaporation, is presented to study the effect of nanoparticles size and coating on thermal performance. While Chapter 4, shows the thermal performance of two-phase heat transfer devices using gold nanofluid and self-rewetting fluid (Butanol solution). Also, Chapter 4 presents the thermal performance inside a micro-exchangers using gold and butanol fluids. Finally, the last part concludes the accomplished experimental works and research discoveries, and proposes the perspectives in future work.

Chapter .I Literature review

I.1 NANOFLUIDS OVERVIEW 7
I.1 Definition *7*
I.2 PROPERTIES 8
I.2.1 Thermal conductivity *8*
I.2.2 Dynamic viscosity *9*
I.2.3 Density and specific heat *9*
I.3 TYPES OF NANOPARTICLES 10
I.4 NANOFLUID PREPARATION 10
I.5 INFLUENCE OF NANOFLUIDS ON THERMOPHYSICAL PROPERTIES 10
I.5.1 Effect of the volume concentration of nanoparticles *11*
I.5.2 Effect of the type of nanoparticles *11*
I.5.3 Effect of temperature *12*
I.6 ADVANTAGES AND DISADVANTAGES OF NANOFLUIDS 13
I.6.1 Advantages of nanofluids [47-49] *13*
I.6.2 Disadvantages of nanofluids [50-53] *13*
I.7 NANOFLUIDS FIELDS OF APPLICATION 14
I.7.1 Heat transfer mechanism associated with cooling systems *14*
a- Conductive transfer 14
b- Convective transfer 15
c- Droplets evaporation-liquid/vapor phase change 15
I.7.2 Main cooling systems used in power electronics *18*
1- Active cooling systems 18
1.1 Active direct cooling 18
1.2 Active indirect cooling 20
2- Passive cooling systems 20
2.1 Passive direct cooling 21
2.2 Passive indirect cooling 22
I.7.3 Passive phase change cooling systems - Heat pipes *23*
1.7.4 Definition and operating principle *23*
1.7.5 Types of heat pipes *24*
I.8 HEAT PIPES PERFORMANCE USING NANOFLUIDS 26
1.9 CONCLUSION 30

Heat transfer fluids are often involved in the applications of cooling such as heat exchangers, electronic cooling system and cooling for internal combustion engines (car engines, refrigerators). The heat transfer fluid is chosen according to its physical and chemical properties (viscosity, thermal conductivity, thermal capacity, etc.). However, these fluids have very low thermal conductivities which limits these heat transfer capacities. Introducing, as a new nanotechnology, nanoparticles into these fluids may be a solution. This Chapter corresponds to a descriptive study of nanofluids, their properties, their composition and their methods of synthesis.

I.1 Nanofluids overview

I.1 Definition

A nanofluid is the suspension of nanometric size particles (the diameter is typically less than 100 nm) in the base liquid such as water, ethylene glycol and oil [22-26]. This new generation of these fluids was introduced in order to improve the properties of basic fluids, in particular thermal conductivity, by introducing nanoparticles with very high conductivity [27-30]. The table below presents the comparison of the thermal conductivities of some fluids and materials.

Materials and Fluids	Thermal conductivity ($W/m.k$)
Water	0.599
Copper, pure	386
Gold, pure	318
Motor Oil	0.14
Silver, pure	418
Carbon nanotube	3000-6000
Butanol	0.15

Table I.1. Comparison of thermal conductivities of some fluids and materials at 20 ° C. [31]

I.2 Properties

I.2.1 Thermal conductivity

The thermal conductivity generally is an important property, mainly in our study because it plays a very important role in the phenomenon of heat transfer, it can clearly indicate the efficiency of the heat transfer of the fluid or the solid. The conductivity of the nanofluids depends on the temperature, nature of the base liquid, nature of the material constituting the nanoparticles, size, shape, volume concentration of the nanoparticles, presence of additives and the PH of the mixed.

Different authors propose thermal conductivity calculation models generally based on mixing laws (fluid-nanoparticles). The most common models are those of Maxwell (1873) and Hamilton-Crosser (1962). The following table shows the two models:

Model	Thermal conductivity	Remark
Maxwell model [32]	$\frac{k_{nf}}{k_f} = \frac{k_p + 2k_f - 2\emptyset(k_f - k_p)}{k_p + 2k_f + \emptyset(k_f - k_p)}$	Particles of spherical shape
Hamilton-crosser [33]	$\frac{k_{nf}}{k_f} = \frac{k_p + (n-1)k_f + (n-1)\emptyset(k_p - k_f)}{k_p + (n-1)k_f - \emptyset(k_p - k_f)}$	Where *n* is the empirical shape factor

Table I.2. Maxwell and Hamilton-Crosser models, "f" for the fluid and "p" for the particles.

I.2.2 Dynamic viscosity

Viscosity can be defined as a property of a fluid so that it resists deformation when it is set in motion. We can therefore speak of viscosity as a measure of the internal friction of a fluid. A very viscous liquid is a liquid that has high internal friction. The dispersion of nanoparticles in a liquid has an effect on the dynamic viscosity of the latter. The viscosity obtained becomes the dynamic viscosity of the nanofluid which can be greatly influenced by the quality of the dispersion of the nanoparticle in the base fluid and the temperature, this dynamic viscosity can be calculated from the dynamic viscosity of the base fluid and the volume fraction of the nanofluid. The most used viscosity calculation models are summarized in the table below:

Model	Dynamic viscosity	Remark
Einstein (1906) [34]	$\mu_{nf}/\mu_f = (1 + 2.5\emptyset)$	$\emptyset < 0.05$; Particle volume fraction
Brinkman (1952) [35]	$\mu_{nf}/\mu_f = \frac{1}{(1-\emptyset)^{2.5}}$	Particles of spherical and non-spherical shape
Corcione [36]	$\mu_{nf}/\mu_f = \frac{1}{1 - 34.87(d_p/d_f)^{-0.3}\emptyset^{1.03}}$	d_f is the equivalent diameter of a base fluid molecule, $d_f = 0.1\left(\frac{6M}{N\pi\rho_f}\right)^{1/3}$
Rudyak [37]	$\mu_{nf}/\mu_f = 1 + (2.5 + 13.43e^{-0.013d_p/d_f})\emptyset + (7.35 + 38.33e^{-0.013d_p/d_f})\emptyset^2$	

Table I.3. Models used to calculate the viscosity of nanofluids.

I.2.3 Density and specific heat

The calculation of the density ρ and the specific heat capacity C_p of the nanofluids is carried out by mixing laws [38]:

$$\rho_{nf} = \rho_p \emptyset + (1 - \emptyset)\rho_f \quad (1)$$

$$Cp_{nf} = Cp_p \emptyset + (1 - \emptyset)Cp_f \quad (2)$$

I.3 Types of nanoparticles

A nanoparticle is an assembly of around a hundred to a few thousand atoms. Practically the nanoparticles are between the microscopic scale and the atomic or molecular scale. Nanoparticles can be classified as follows: [40-42]

- Nanoparticles based on metals (Aluminum, Copper, Gold, Silver, Iron, etc.).
- Nanoparticles of metal oxides (CuO, Al_2O_3, SiO_2, T_iO_2…).
- Non-metallic nanoparticles such as carbon nanotubes (CNT) and titanium nanotubes.

I.4 Nanofluid preparation

Nanofluids are prepared by mixing nanoparticles and the base fluid. Therefore there are two basic methods for producing nanofluids: [42, 43]

1- The two-step method

It is a method which consists first of producing nanoparticles in the form of dry powder, then of dispersing them in a basic fluid. In order to have a good dispersion, strong mechanical action using a rotary agitator (ultrasonic path). In addition, to eliminate the agglomeration due to attraction forces between particles, electrostatic forces are used by changing the surface of the particles by adjusting the pH.

2- The one-step method

This technique consists in dispersing the nanoparticles directly in a base fluid (vaporization of a solid material in a vacuum reactor, then direct condensation in the fluid). It is only used for certain types of nanofluids.

I.5 Influence of nanofluids on thermophysical properties

I.5.1 Effect of the volume concentration of nanoparticles

The group of researchers worked on particles of AL_2O_3 suspended in water to monitor the effect of the volume concentration of particles on the thermal conductivity of the nanofluid.

The graphs below, **Fig. I.1** show the effect of the volume concentration on the thermal conductivity of the nanofluid (Al_2O_3 / Water) for different researchers using this correlation $\frac{k_e}{k_m} = 1 + 0.764\emptyset + 0.0187(T - 273.15) - 0.462$ where k_e is the effective thermal conductivity, k_m is the thermal conductivity of base fluid, $\emptyset$ nanoparticles volume fraction and T is the temperature in Kelvin.

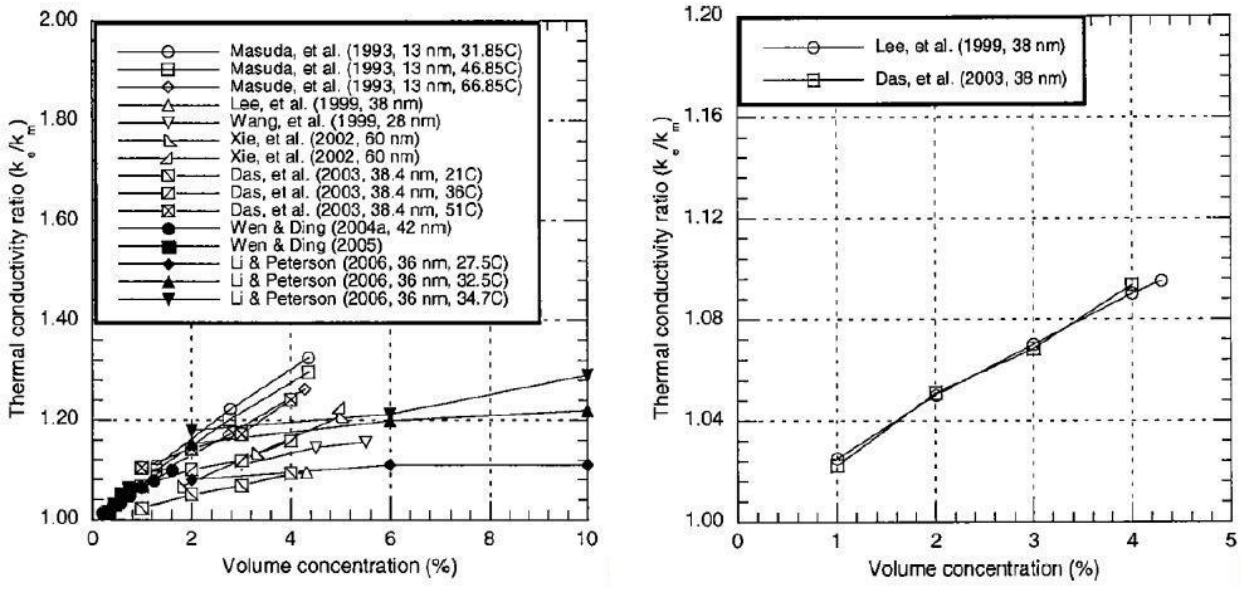


Figure I.1. The effect of volume concentration on thermal conductivity of Al_2O_3 /water nanofluids. [44]

From the graphs we see that the thermal conductivity increases as a function of the volume fraction of the particles and that the concentrations of metal oxide particles give an improvement in thermal conductivity of up to 30%.

I.5.2 Effect of the type of nanoparticles

The researchers took two types of nanoparticles, one is a metal oxide and the second is a metal, both are diluted in water with the temperature and shape of the particle are considered constant. These graphs, **Fig. I.2**, show the effect of particle types on the thermal conductivity of nanofluids.

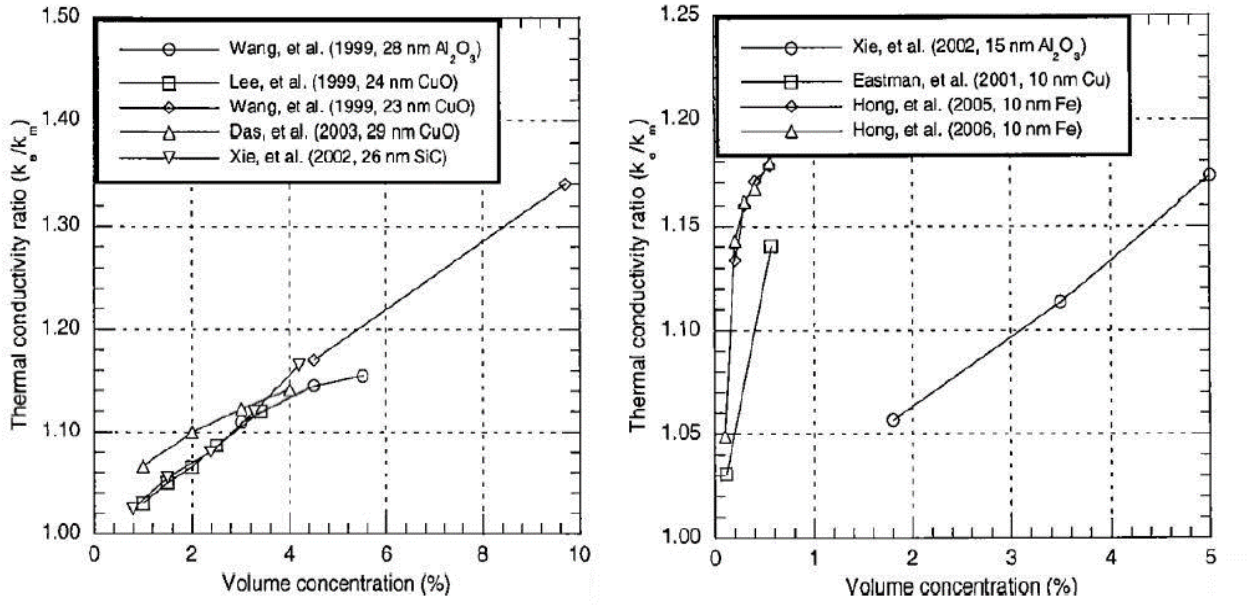


Figure I.2. Effect of particle types on the thermal conductivity of nanofluids. [45]

I.5.3 Effect of temperature

Thermal conductivity sensitive to temperature. The two graphs, **Fig. I.3**, below present the results of two researchers Das and Col for a temperature range from 28 ° C to 51 ° C using the nanofluids Al_2O_3 and CuO.

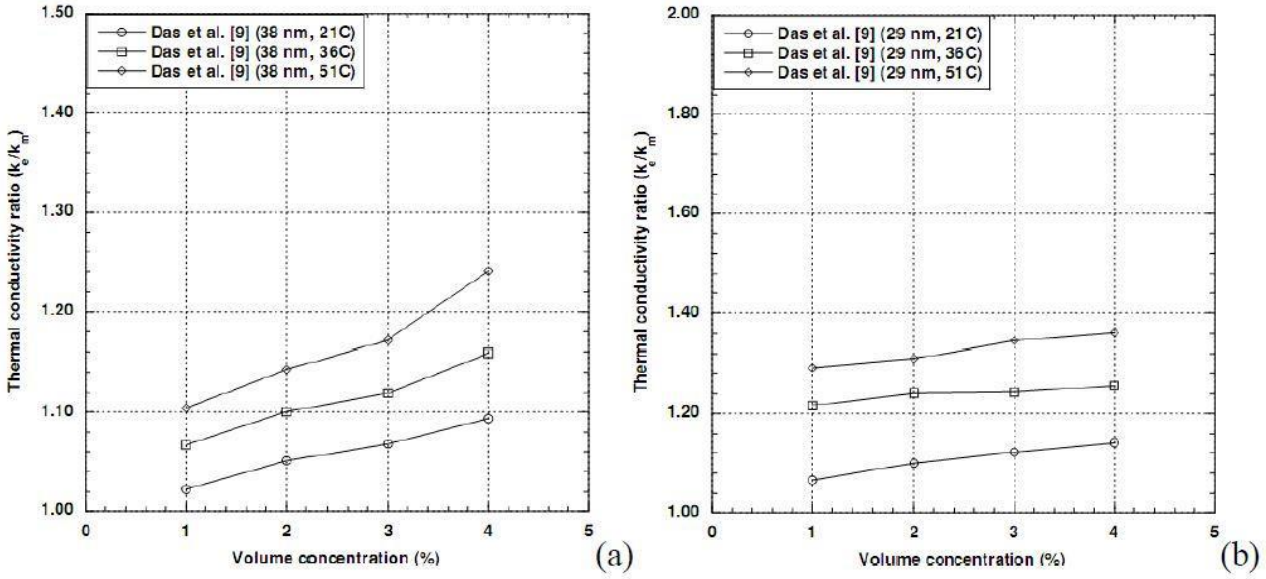


Figure I.3. Effect of temperature on the thermal conductivity of nanofluids. [46]

It is observed that the thermal conductivity increases when the temperature increases. But it is higher for copper oxide compared to aluminum oxide.

I.6 Advantages and disadvantages of nanofluids

I.6.1 Advantages of nanofluids [47-49]

- A large heat transfer surface between particles and fluids.
- Adjustable properties, including thermal conductivity and wettability of the surface, by varying particle concentrations according to different applications.
- Reduce the use of ventilation in cooling systems while maintaining performance.

I.6.2 Disadvantages of nanofluids [50-53]

- Stability of nanoparticles in dispersion.
- Increased pressure drop and pumping power.
- Lack of theoretical understanding of the mechanisms responsible for property changes.
- The high cost of nanofluids.
- Very delicate nanoparticle manufacturing process.

I.7 Nanofluids fields of application

Generally, nanofluids are used to improve heat transfer and energy efficiency in various thermal systems. These nanofluids could be used in a wide range of industrial applications such as electronics, transport, nuclear… [54-57]. Nanofluids are used as cooling fluids in integrated circuits. For this, several researchers have carried out studies. On the one hand, the two researchers Tsai and Col have fabricated a nanofluid in a water-based microcomputer to cool a central unit. On the other hand, Mal and Cal studied the effect of the nanofluid on the possibilities of heat transport from an oscillation heat pipes. Furthermore, the mixture of ethylene glycol and water are used as coolant in vehicle engines and the addition of nanoparticles in these liquids improves the cooling rate. Nanofluids are also found in the nuclear energy industry due to their performance in cooling nuclear systems. For space applications, the group of researchers has carried out studies to show that the presence of nanoparticles in the coolant in general electronics plays a very important role in space applications.

I.7.1 Heat transfer mechanism associated with cooling systems

a- Conductive transfer

It is the transport of energy in matter without displacement of matter. This transport can be carried out by electrons (conductor) or by photons (insulator).

It depends on the thermal conductivity of the material used, assuming that the geometric dimensions of the solid element are adequate. Optimizing conductive transfer therefore means using the most conductive materials possible with certain constraints, however: mechanical / thermal resistance and cost.

b- Convective transfer

Defined as the transport of energy or excess heat by the flow of fluids (gas, fluid) across a surface. It is the most efficient and therefore the most used heat transfer mechanism. Convection can also be subdivided into natural or forced monophasic convection, and into natural or forced biphasic convection. Industrial cooling systems based on forced convection of a two-phase fluid.

Convective exchanges are influenced by three factors:

- The coefficient of exchange between the fluid and the wall (or the element to be cooled).
- The nature of the fluid used in terms of its thermophysical properties (thermal conductivity, density, specific heat, dynamic viscosity).
- The exchange area.

c- Droplets evaporation-liquid/vapor phase change

Droplet evaporation plays a vital role in various fields of natural science and engineering such as burning liquid-fuels, biological crystal growth and painting. Moreover, the high heat transfer rates associated with evaporation suggests its use in contexts with a variety of thermal applications, such as spray-cooling or in the electronics industry for cooling of integrated circuits with high heat dissipation rates.

The evaporation of a sessile droplet is a fundamental heat and mass transfer process in the nature. When a droplet is deposited on a solid surface, its profile is determined by the equilibrium of gas, liquid and solid phases. Three interfacial tensions (solid/liquid, liquid/vapor and solid/vapor) were described by Young in 1805 [58], presented in the following equation:

$$\gamma_{SV} - \gamma_{SL} = \gamma_{LV}.cos\theta_c \qquad (3)$$

Where γ_{SV}, γ_{SL}, γ_{LV} are surface tension od solid /vapor, solid/liquid, liquid/vapor interfaces respectively, θ_c s the contact angle which is the droplet angle between liquid/solid and liquid/vapor interfaces. The wettability of solid substrate with droplet depends on the physical properties of liquid and the surface characteristics of substrate, which can classify substrate into

two types by the measurements of contact angle: hydrophobic when contact angle is above 90° and hydrophilic when contact angle falls in range of 0° ~ 90°.

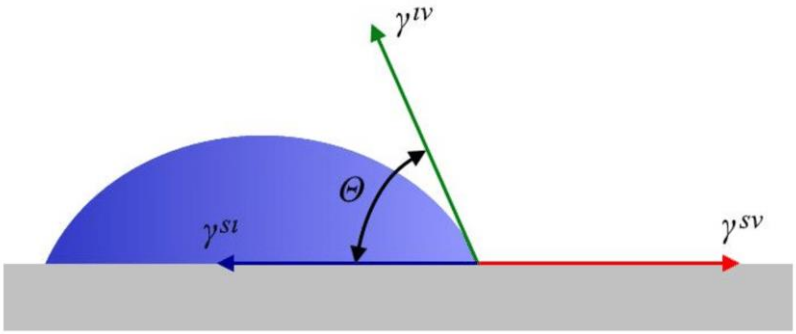


Figure I.4. Contact angle of a liquid droplet wetted to a rigid solid surface. [59]

The droplet profile evolution can be identified in three different regimes (**Fig. I.5**): (1) constant contact line regime (CCL), when the wetted area of droplet stays unchanged and the contact angle decreases gradually; (2) constant contact angle regime (CCA), when the contact angle remains constant during the reduction of contact area; (3) mixed regime, when the profile evolution jump from CCL to CCA, vice versa or both contact angle and contact line decrease simultaneously. CCL regime is often observed in the evaporation of sessile droplet on hydrophilic substrate while the evaporation on hydrophobic substrate frequently behaves in CCA regime.

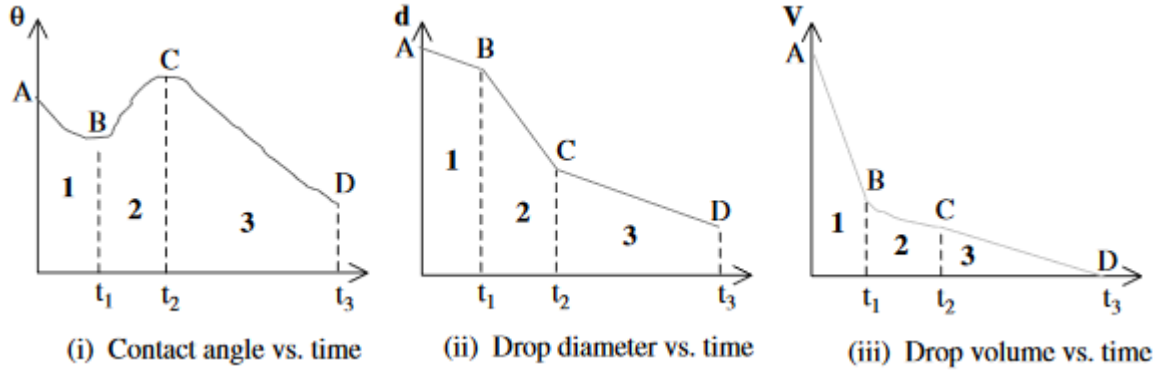


Figure I.5. The evolution of parameters ((i) contact angle (ii) drop diameter (iii) drop volume) during evaporation of a water-ethanol mixture drop as a function of time. [60]

i- Marangoni effect

When concerning about the flows inside a sessile single or multi droplets on a heated substrate, a surface tension difference driven impact assumes a significant role in evaporation kinetics. This impact is named as Marangoni effect, named after Italian physicist Carlo Marangoni who firstly reported this surface phenomenon in 1855. [61]

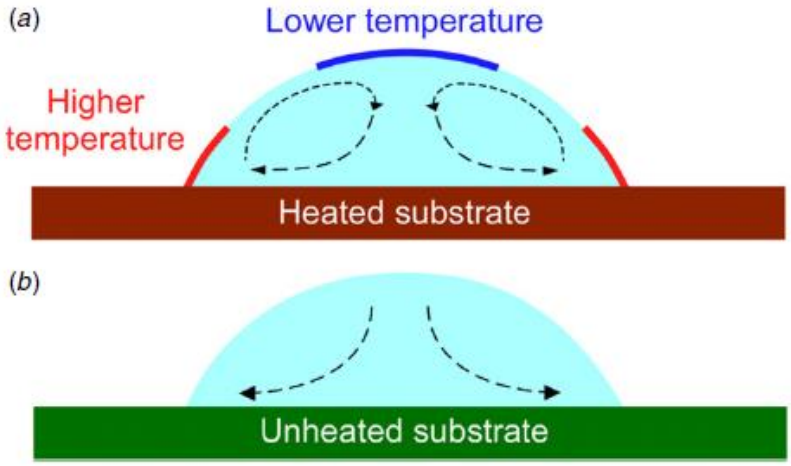


Figure I.6. (a) Liquid flow patterns in an evaporating droplet on a heated substrate. A stable Marangoni flow forms in the droplet. (b) Liquid flow patterns in an evaporating droplet on an unheated substrate. Evaporation induced radial flow is the dominant flow. [62]

Surface tension of basic fluids has a monotonically diminishing relationship with increment of temperature. Some fluids have a natural inclination of moving from low surface area spot to high surface tension place. At the point where the droplet is deposited on an unheated substrate, most of evaporation happens at vicinity of contact angle. If the substrate is heated, heat is conducted from solid/liquid interface (low surface tension) to liquid/vapor interface (high surface tension). Also, the temperature at vicinity of contact line is higher than that at the top of droplet and it named as capillary flow. The induced flow is called thermal Marangoni flow or thermo-capillary flow.

For heat transfer aspect, Savino and Fico [63] analyzed the evaporation performance of pendant drops containing silicone oil and hydrocarbon by experimental and numerical methods, and the results revealed that the Marangoni flow induced by non-uniform evaporation can improve homogeneity of temperature distribution on drop surface as well as overall evaporation rate. Also, Buffone and Sefiane [64] observed intense Marangoni convection inside the liquid meniscus formed in capillary tube. The evaporative cooling effect is considered as the driving mechanism

of surface tension gradient induced convection which effectively enhances the heat and mass transfer from the pore.

I.7.2 Main cooling systems used in power electronics

Cooling systems extend the life of components and guarantee uninterrupted operation. As a result, several researches have been carried out in order to develop these systems. Cooling techniques can be classified into two main categories: [65, 66]

1- Active cooling systems

They are based on heat transfer by forced convection. The use of a mechanical pump is necessary to ensure the circulation of heat transfer fluid. In addition, these systems must have an external circuit to dissipate heat to the outside.

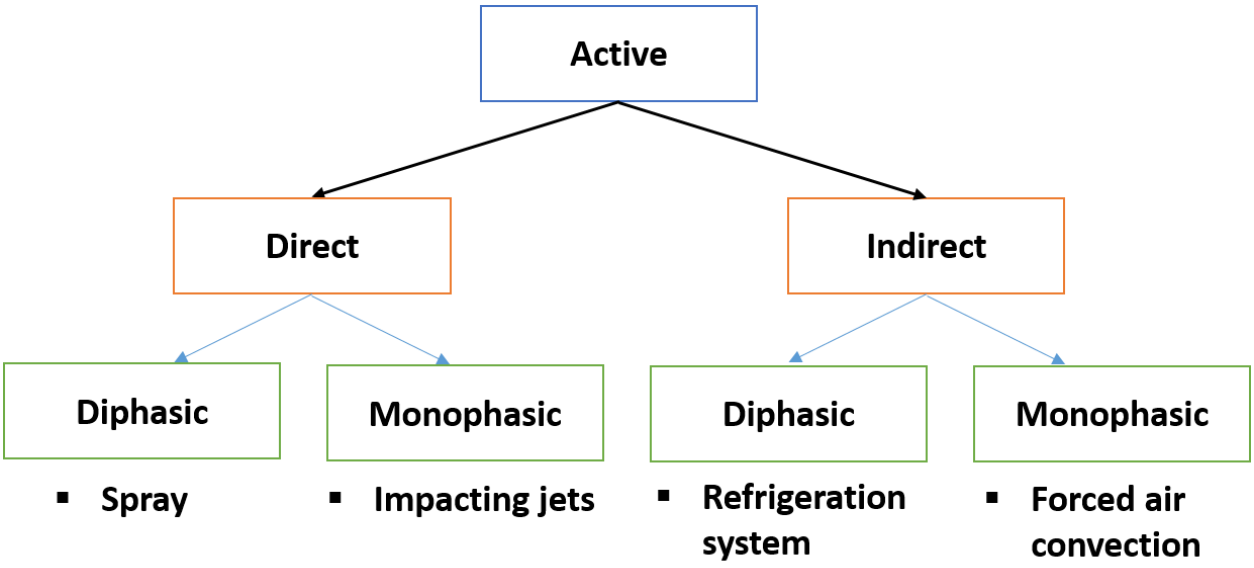


Figure I.7. Classification of active cooling systems.

1.1 Active direct cooling

a- Diphasic

We can cite the example of spray cooling. It consists in using a heat transfer fluid which will be sprayed in drops and in sending these drops to the surface to be cooled.

After contact with the hot surface, these drops will evaporate while recovering the power dissipated by the component (to be cooled). The spray cooling technique is complex, **Fig. I.8**, since it depends on several parameters (such as the angle of impact, the roughness of the surface, etc.).

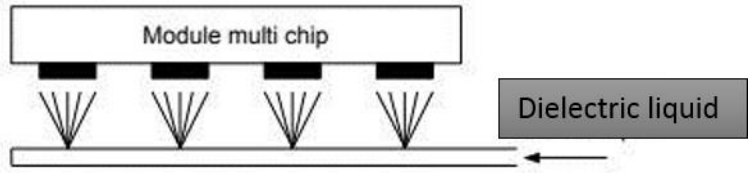


Figure I.8. Principle of cooling by spraying with dielectric liquid. [67]

b- Monophasic

For this type, we can cite the example of jet cooling which is widely used in industrial applications such as aeronautics where it is used to cool large areas (engine combustion chambers, turbine blades). The element to be cooled is then brought into contact with an exchanger whose walls by the impacting jets as shown in the figure below:

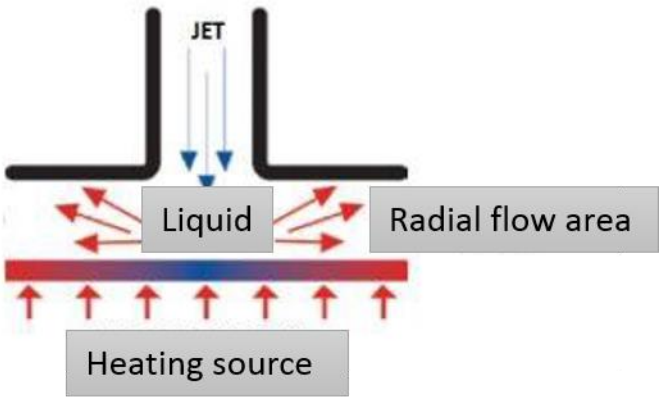


Figure I.9. Principle of jet cooling. [68, 4]

1.2 Active indirect cooling

a- Diphasic

For this type of cooling, the most common devices are refrigeration systems. These refrigeration devices are used for thermal control. However, the working temperature influences the performance of this cooling system.

b- Monophasic

We can cite forced convection in air, this method is the most used in cooling electrical components whose principle consists in blowing forced air thanks to fans. Otherwise, cooling using a piezoelectric fan behaves like another cooling technique based on air blowing, the principle of which is to supply electric current to a ceramic blade which will oscillate at high frequencies. Then, an air passage can increase the convective exchange coefficient by up to 100% compared to a convective exchange by conventional fan. [68]

2- Passive cooling systems

It includes all of the cooling devices that do not consume any energy to operate, which reduces energy consumption. Passive cooling can itself be classified into two sections: direct or indirect depending on whether the heat transfer fluid is or is not in contact with the electronic components.

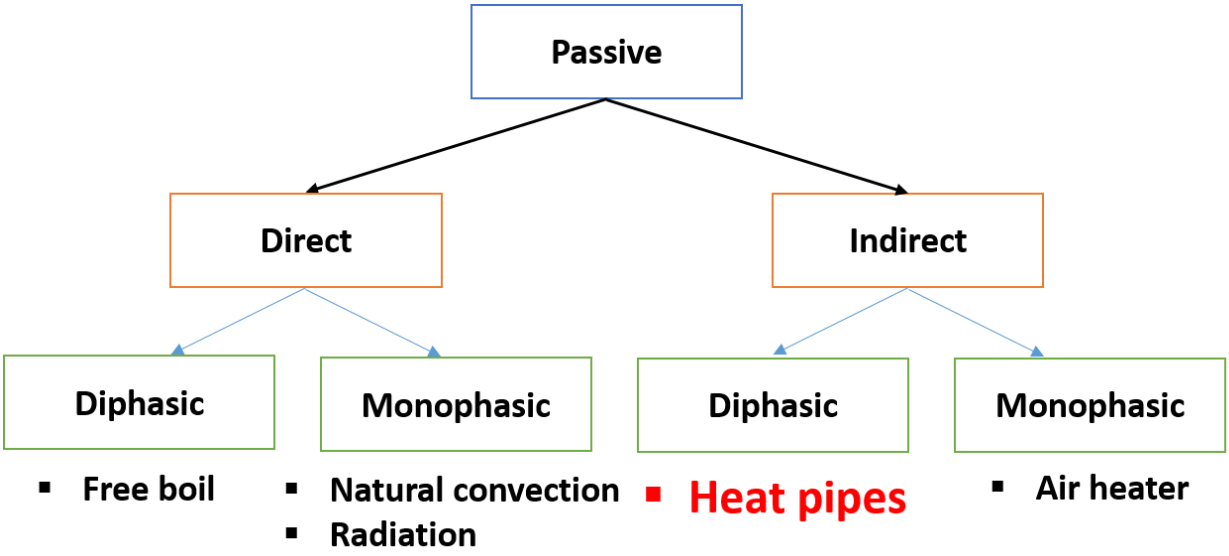


Figure I.10. Classification of passive cooling systems.

2.1 Passive direct cooling

a- Diphasic

The only technique to be classified in this category is free boiling cooling. It consists of immersing electronic power dissipating components in a dielectric liquid, see **Fig. I.11**. Depending on the heat flux or the temperature difference between the hot surface and the liquid saturation temperature, bubbles begin to appear, cooling the hot surface in passing. This technique involves the use of large quantities of fairly expensive dielectric liquid and poses maintenance and leakage problems for servers.

The nucleated boiling regime is particularly effective, the vapor bubbles creating micro-convection. This technique requires a condenser in which a heat transfer liquid circulates to obtain a thermally stable system, but its cost is relatively low compared to the expected gain.

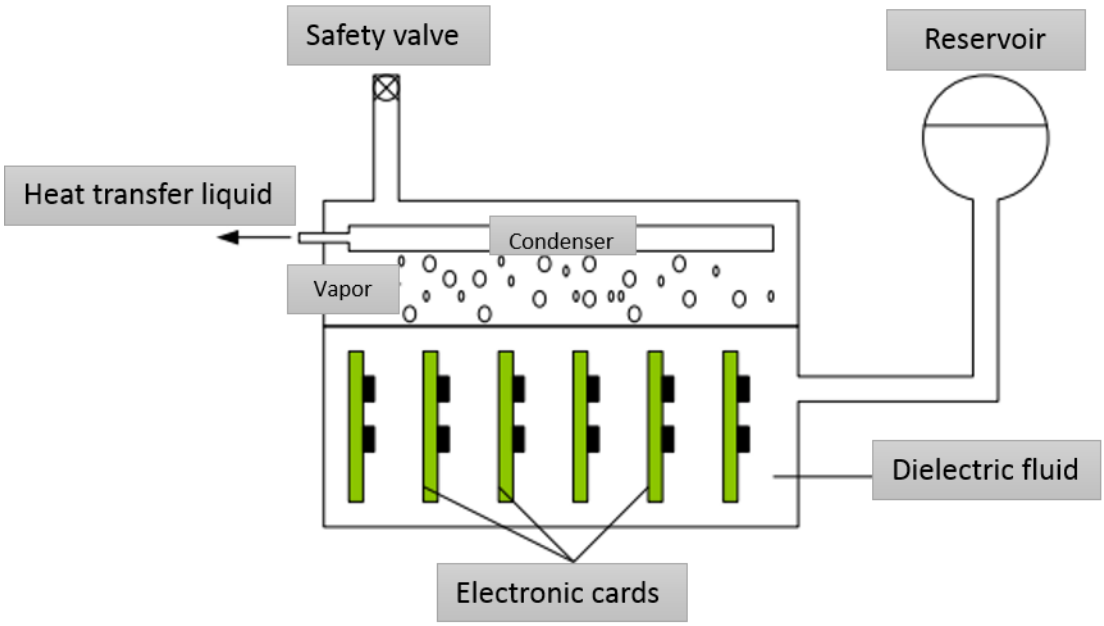


Figure I.11. Principle of free boiling cooling. [69]

b- Monophasic

This is the case with natural convection and the radiation with surrounding surfaces is generally sufficient to ensure the correct cooling of the dissipating components less than 5 Watt. These two most simple and trivial techniques of cooling electronic components.

2.2 Passive indirect cooling

a- Diphasic

This category includes any system based on the transfer of energy by latent heat in indirect contact with the components to be cooled. All heat pipe systems of all types are included: LHP, thermo siphon, capillary network heat pipe, etc.

In electronics, heat pipes can have two roles in cooling electronic components: acting as a heat sink to eliminate any hot spots that may appear, or moving the heat dissipated by the components

to the cold source. All the physics of the operation of heat pipes will be well detailed in the next part of this manuscript.

b- Monophasic

When the power density of the electronic components to be cooled is too low to use fans and it is too high for direct passive cooling, the use of radiators is common, the aim being to offer a larger surface area exchange between air and hot surface.

I.7.3 Passive phase change cooling systems - Heat pipes

The appearance of miniaturized systems, especially in electronics, increasingly involves the use of passive cooling techniques by phase change of the heat transfer fluid (nanofluids for microsystems), since they are characterized by good performance thanks to the absence of mechanical fluid pumping systems. [70]

Among these passive two-phase cooling devices, heat pipes (micro-pipes, two-phase capillary pumped heat pipe loops, etc.). In this manuscript, we will focus on the heat pipes which will be detailed in the next part.

1.7.4 Definition and operating principle

A heat pipe is a passive phase change cooling system. The advantage of using this technique is to transfer heat with a very low temperature gradient between two sources. The operating principle of a heat pipe resides in the movement of the heat transfer fluid in a closed loop. It is illustrated in **Fig. I.12** below: [71]

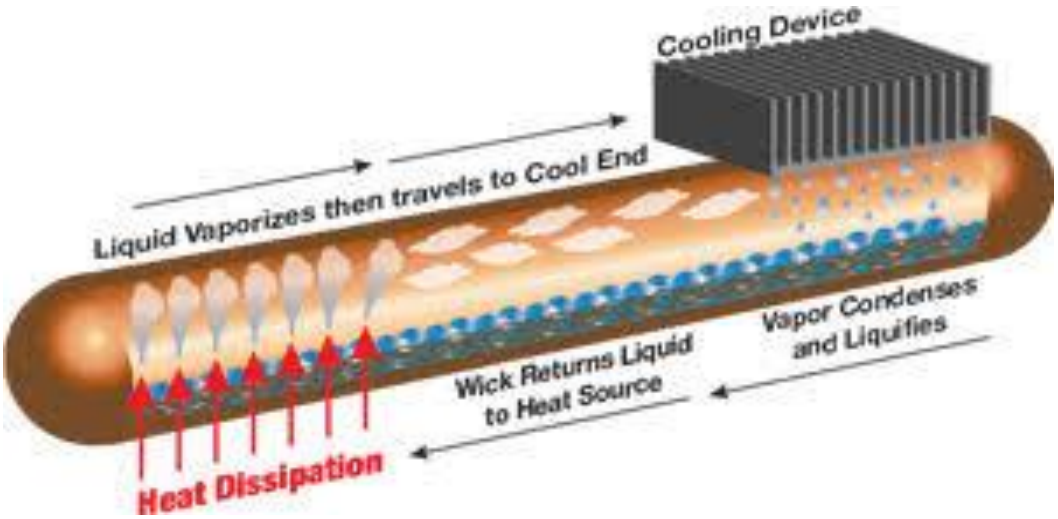


Figure I.12. Heat pipe working principle. [71]

Under the effect of heat flow, the fluid will be vaporized at the level of the evaporator (zone of the heat source), which will subsequently create a circulation of vapor along the adiabatic section. During the passage of this vapor in the part of the condenser (cold zone), it condenses. The capillary structure of the heat pipe preserves the return of liquid to the evaporator. In fact, the capillary pressure is inversely proportional to the radius of curvature of the liquid-vapor interface.

The difference in saturation therefore generates a pressure difference in the capillary structure of the heat pipe between the evaporator and the condenser, this explains the flow of the fluid thanks to this pressure. [72]

1.7.5 Types of heat pipes

a- Micro heat pipe

The micro-heat pipe is defined as a heat pipe in which the mean curvature of the liquid/vapor interface is comparable in magnitude to the reciprocal of the hydraulic radius of the total flow channel. In practice, this device consists of a non-circular channel with a diameter between 10 and 500 μm and a length between 10 and 20mm. The operating principle of the micro-pipe is the same as that of heat pipes, see **Fig. I.13**. [73]

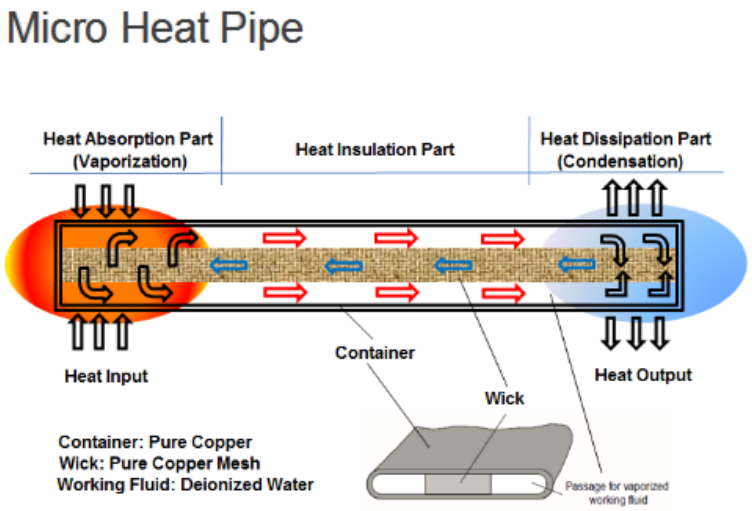


Figure I.13. Diagram illustrating a micro-pipeline. [73]

b- Two-phase capillary pumping loops

Capillary Pumped Loop (CPL) are widely used for space applications [74]. These loops have been developed to avoid interactions between the liquid and vapor phases through separation by different conduits, since in conventional heat pipes, the vapor and the liquid are in contact and circulate in opposite directions. The advantage of these loops is the possibility of fixing the pressure and regulating the evaporation temperature thanks to the presence of a temperature-controlled tank. In addition, the flow in separate pipes makes it possible to have greater reliability than that of the heat pipes in terms of distance between the hot source and the cold source. [75]

The operating principle is the same as that of the heat pipe, however, for a capillary pumping loop, the paths of the liquid and the vapor are decoupled. It is well illustrated in the figure below:

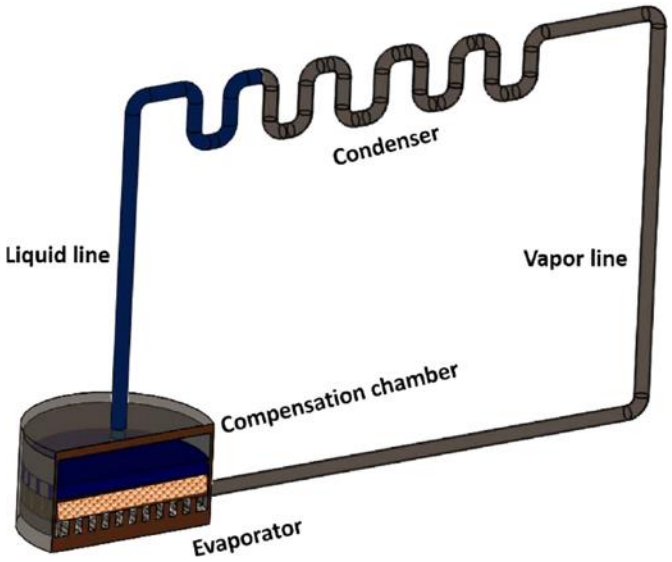


Figure I.14. Schematic diagram of the two-phase capillary pumping loop. [75]

I.8 Heat pipes performance using nanofluids

As we know, heat pipes are used extensively in various applications, for achieving high rates of heat transfer utilizing evaporation and condensation processes [76–85]. Heat pipes have been used in space crafts, computers, solar systems, heat and ventilating air conditioning systems and many other applications. Most heat pipe analysis is based on the steady state operation of the device. However, in a number of applications start-up characteristics are quite important. Improper start-up can cause damage to the heat pipe. As such it is important to analyze the start-up process for the heat pipes [86]. Several transient models for the start-up of the heat pipes have been presented in the literature such as the ones by Tournier and El-Genk [87] and Chang and Colwell [88]. However, these works were all based on a regular cylindrical based geometry.

The thermophysical properties of a liquid, specifically, the thermal conductivity and heat capacity can significantly affect the heat transfer process in the liquids. Both of these properties can be augmented by dispersing the liquid with solid nanoparticles. The new liquid which now has better characteristics in transferring heat is called nanofluid [89, 90]. The other properties of this liquid such as density and viscosity also change as a function of concentration of nanoparticles [75, 76, 90, 91]. So, some researchers has been showed the thermal performance of heat pipe using different types of nanofluid [92, 93]. P. Gunnasegaran et al. [94] present the effect of Al_2O_3-water

nanofluids on heat transfer in a loop heat pipe. The results showed the positive influence of nanofluid utilizing as a heat pipe working fluid on the system thermal performance. It is found that the thermal resistance of LHP decreases when particle mass concentration of Al_2O_3-water nanofluid increases. Also, the LHP charged with Al_2O_3-water nanofluid yields lower wall temperature difference between evaporator and condenser and reaches its steady state faster than LHP charged with pure water.

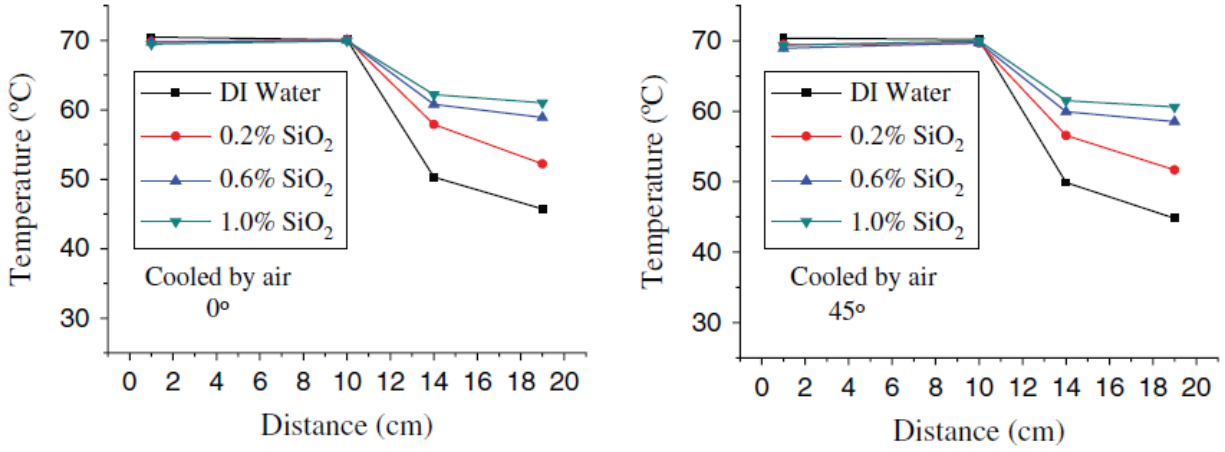
Furthermore, other types of nanofluids were studied to present their performance in heat pipe systems. K. Alizad et al. [95] discussed and analyzed the thermal performance of a flat-shaped heat pipes using three different types of nanofluids such as CuO, Al_2O_3 and TiO_2. The results illustrated enhancement in the heat pipe performance while achieving a reduction in thermal resistance for both flat-plate and disk-shaped heat pipes throughout the transient process. Thus, it showed a higher concentration of nanoparticles increases the thermal performance of the two heat pipes shape.

The study of the thermal performances of heat pipes using nanofluids, as indicated above, can be carried out by measuring the wall temperature and by finding the thermal resistance of the evaporator. From these measurements, we can obtain and observe the enhancement in heat transfer of heat pipes. In this work, Y.F. Niu et al. [96], an experimental investigation of thermal performance of miniature heat pipe using SiO_2-water nanofluids is presented. The four miniature heat pipes, see **Fig. I.15**, filled with DI water and SiO_2-water nanofluids containing different volume concentrations (0.2%, 0.6% and 1.0%) are experimentally measured on the condition of air and water cooling.



Figure I.15. Photograph of the four miniature heat pipes.

At the same of inlet heat water temperature in the heat system, it is observed that the total wall temperatures on the evaporator section are almost retaining constant by air cooling and the wall temperatures at the front end of the evaporator section are slightly reduced by water-cooling. However, the wall temperatures at the condenser section using SiO_2-water nanofluids are all higher than that for DI water on the two cooling conditions, **Fig. I.16**. As compared with the heat pipe using DI water, the decreasing of the thermal resistance in heat pipe using nanofluids is about43.10%~74.46% by air cooling and 51.43%~72.22% by water cooling. These indicate that the utilization of SiO_2-water nanofluids as working fluids enhances the performance of the miniature heat pipe.



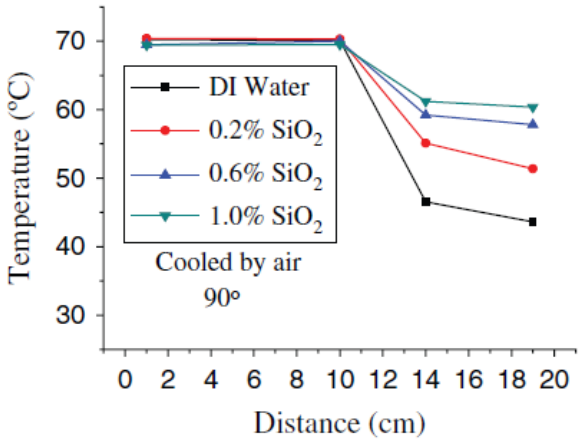


Figure I.16. Wall temperature distributions of heat pipes by air cooling.

Also, thermal resistance was calculated to quantitatively evaluate the thermal performance of heat pipes using SiO_2-water nanofluids, the corresponding thermal resistances of the four heat pipes was calculated compared to base water fluid at different heat inputs, see **Fig. I.17**.

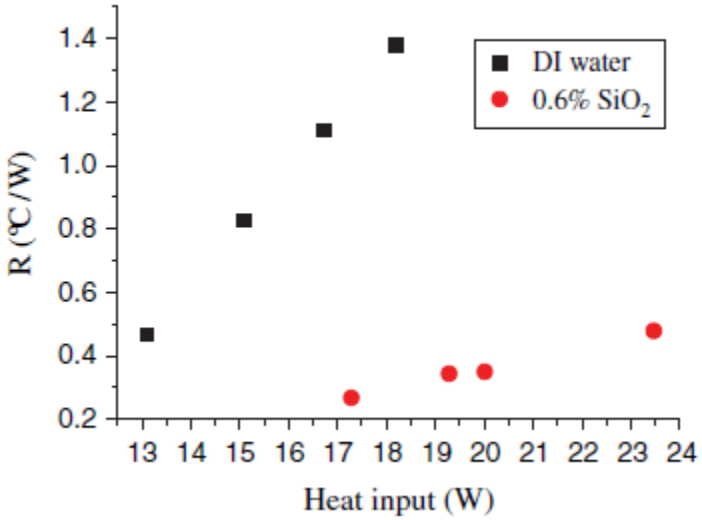


Figure I.17. Thermal resistance of heat pipes by air cooling.

1.9 Conclusion

To assess the impact of the introduction of nanoparticles on the efficiency of nanofluids as well as the most favorable materials, we carried out a literature search on heat transfer nanofluids used in passive phase change cooling systems (heat pipes). In the first part, we started with the definition of nanofluids and nanoparticles and their properties, the effect influencing the thermophysical properties of nanofluids. Then we detailed the preparation techniques. We also reserved the second part to explain the different technologies of industrial cooling systems more specifically phase change cooling systems (heat pipes). The last part concerns the most efficient materials (nanoparticles) used in nanofluids to see the difference in reliability of these materials used as nanoparticles dispersed in heat transfer fluids.

Industrial cooling systems have three main components: a cold source, a hot source and an energy carrier. Recent research consists in modifying or improving the performance of the energy vector. This Chapter talks about nanofluids that allowed us to understand their effectiveness in improving energy expenditure and heat transfers. The analysis could be performed by direct application of the nanofluids in the heat transfer to study the performance of this system.

There is no denying that a good nanofluid gives a boost to the efficiency of any liquid cooling system. Indeed, in the case of miniaturized space, aeronautical and above all electronic systems, where the mass of the system holds a significant part of the cost, the transfer by forced convection of the nanofluids is therefore penalized. It is then possible to use passive phase-change systems (heat pipes) to extract heat from the component to the exchangers. It should be noted that the effectiveness of the new heat transfer liquids is linked to the essential choice of the basic nanoparticle-fluid couple.

The present work takes place within the framework of a thesis project program and it is a collaboration between LAMIH and IEMN laboratories as well as Jeumont Electric enterprise based in France. This project is focused on a new technology and strategies to improve the efficiency of heat pipes and all heat exchanger devices for cooling system. As is known, in order to improve heat transfer, it would be desirable to identify additional mechanisms capable of improving the circulation of the fluid in the heat pipes. This technology is based on a self-rewetting nanofluids fluids as working liquids to improve the thermal management of exiting devises. Since then, the

use of these types of fluids (Nanofluid and self-rewetting fluids) has had a significant impact on heat transfer performance. The main goal is to study the best performance of nanofluids and self-rewetting fluids to be used later. The selection was based on their thermophysical properties such as thermal conductivity, viscosity, droplet evaporation…Thus, a new method was used for the first time, based on high frequency acoustic waves, to optimize the stability of nanoparticles inside the fluid. This method open access to calculate the viscosity of nanofluids at different concentrations. Evaporation of droplets containing different types of nanoparticles, at different volume concentrations and different sizes was performed using a Drop Shape Analyzer (KRUSS software) under control conditions. Later, the selected nanoparticles will be used in the two phase heat transfer devices, as working fluids, to observe their thermal performance.

In this thesis, Chapter 2 introduces a combination of infrared and acoustic technique to track the dynamic deposition of copper oxide and gold nanofluids during droplet evaporation at different surface temperatures. For nanofluids, the biggest challenge is the balance between suspension stability and thermal conductivity. Thus, Chapter 2 provides a new method to calculate the effective shear viscosity of gold nanoparticles during droplet evaporation because the acoustic waves generated by the transducer, through the substrate, has the capacity to analyze what is happening at the solid/liquid interface. An experimental evaporation performance of gold nanoparticles are investigated to show their sizes and coating effect on thermal performance. Experimental results and analysis are available in Chapter 3. In Chapter 4, applying the selected nanofluid and self-rewetting fluids to use them as a working fluids in the two-phase heat transfer device and micro heat exchangers.

Chapter .II Nanofluids synthesis and thermophysical properties: Acoustic and Thermography methods

II. 1 INTRODUCTION 33
II. 2 INFRARED AND ACOUSTIC METHOD TO TRACK THE DYNAMIC DEPOSITION OF COPPER OXIDE NANOPARTICLES 34
II.2.1 Methodology and experimental setup *35*
II.2.1.1 Infrared and optical measurements 35
II.2.1.2 Acoustic measurements 38
II.2.2 Experimental results *43*
II.2.2.1 Calibration of the acoustic measurement method: Water as a reference liquid 44
II.2.2.2 Optical, infrared and acoustic measurements of CuO-water droplet at ambient temperature 45
II.2.2.3 Effect of substrate temperature on nanoparticles deposition 51
II. 3 DYNAMIC VISCOSITY MEASUREMENTS OF GOLD NANOFLUIDS USING HIGH FREQUENCY ACOUSTIC METHOD (≈1GHZ) 56
II.3.1 Experimental setup *57*
II.3.2 Results and discussion *61*
II.3.2.1 Calibration of the acoustic measurements method: Water as a reference liquid 61
II.3.2.2 Values of dynamic viscosity of gold nanofluid during the evaporation of 4%Cv Au-water droplet 62
II.3.2.3 Viscosity measurements as function of gold nanoparticles concentrations 65
II. 4 CONCLUSION 67

This Chapter is based on the published work in the International Journal of Heat and Mass Transfer (2018) and a second part to be published on viscosity measurements using acoustic methods. The author of this thesis contributed to the Infrared method part by designing and performing experiments, analyzing experimental results and writing the section of the manuscript concerning visual investigation. Dr. J. Carlier, Dr. M. Toubal and Pro. B. Nongaillard took charge of Acoustic method part experiment design and execution, experimental results analysis and manuscript writing. Prof. S. Harmand supported the author of this thesis for the writing of the manuscript and gave approval to the final version.

II. 1 Introduction

In this Chapter, we investigated the precipitation of 0.05%wt copper oxide nanoparticles in a sessile droplet during the evaporation process. We used two complementary methods to analyze the precipitation process of the nanoparticles at the solid/liquid interface: an optical one coupled to an infrared thermography method and an acoustic method. From the optical observation, using a Keyence microscope on the rear side of a transparent glass substrate coated with a silane layer, the precipitation process of the nanoparticles was successfully monitored by measuring the mean intensity density ($\overline{ID}$) above the substrate by using ImageJ software. The acoustic method, based on a high frequency echography principle, allowed to monitor the deposition phenomenon of the particles above a non-transparent silicon substrate having similar silane coating as the glass substrate at room temperature. These waves, represented by the modulus of the longitudinal reflection coefficient, are generated using a transducer located at the bottom of the silicon substrate which is fabricated under specific conditions. The time from which the nanoparticles begin to settle at the bottom of the substrate, obtained from the acoustic method, corroborated the one obtained from the optical one. Moreover, an estimate of the particles concentration throughout the process was deduced. The effect of substrate temperature and substrate wettability have also been studied experimentally and investigated using only the optical method and the infrared thermography one. An infrared camera from the top was employed to observe the temperature effect on the precipitation of the nanoparticles.

Furthermore, when the substrate temperature exceeded 60°C, co-existence of the thermal Marangoni flows was observed. It is expressed as a temperature gradient at the droplet liquid/air interfaces. The result showed the effect of these cells due to Marangoni effect on the nanoparticles' stability.

Moreover, knowing physical properties of nanofluids such as viscosity play key role in practical heat transfer situations. So, the same high-frequency acoustic measurement (1 GHz) done at ambient temperature has the ability to measure the dynamic viscosity of gold nanofluids during droplet evaporation. The attenuation, due to viscoelastic losses, of the sound energy produced by the nanofluid depends on the liquid's viscosity (one of the causes of attenuation- Attenuation in the fluids about 220dB/mm) and generate a complex form for the mechanical impedance of the nanofluid sessile droplet. The measurements were based on the phase of the shear reflection coefficient which gives direct access to the dynamic viscosity in real time at solid/liquid interface. Since, the complexity of the nanofluid for the shear signal wave has a relation between the attenuation and the viscosity, as a result, an online variation in shear viscosity of a droplet contains 4% C_v gold nanoparticles were extracted throughout the evaporation process.

II. 2 Infrared and acoustic method to track the dynamic deposition of copper oxide nanoparticles

In this work, the studied nanofluid consists of copper(II) oxide (CuO) nanopowder (Sigma Aldrich, molecular weight = 79.55, diameter <50 nm with a mass concentration of 0.05 wt%) dissolved in distilled water using the two-step method [97] and then stabilized through ultrasonication (Elma, S 10/H) for at least 1 h before use.

To analyze the dynamic of the droplet evaporation and particles deposition, two different methods are used, one using optical and infrared thermography measurements and the other one using acoustic reflection coefficient measurements at room temperature. For the optical observation, a transparent substrate is required (Glass substrate) whereas a silicon substrate is used for the acoustics measurement. The two substrates were modified with a perfluorodecyltrichlorosilane (PFTS) layer to achieve hydrophobic surfaces. In that case the two substrates were at the same surface temperature.

Then, optical measurements were achieved by increasing the substrate temperature. First, the substrates are cleaned through ultrasonication in acetone and ethanol for 5 min each then the polished face was cleaned by ozonolysis for 15 min in a UV/ozone cleaner to remove all the physisorbed organic molecules. This step gives a zero contact angle. The silanization of the cleaned substrates with PFTS was carried out in a glove box under nitrogen atmosphere.

The cleaned substrates were immersed for 2 h at room temperature in a hexane solution of PFTS (50 µL of PFTS in 50 mL hexane). The substrates were then removed, rinsed with hexane and blown with dry nitrogen. The droplet contact angle on each substrate treated with the silane is measured using a drop shape analyzer 'Kruss System'.

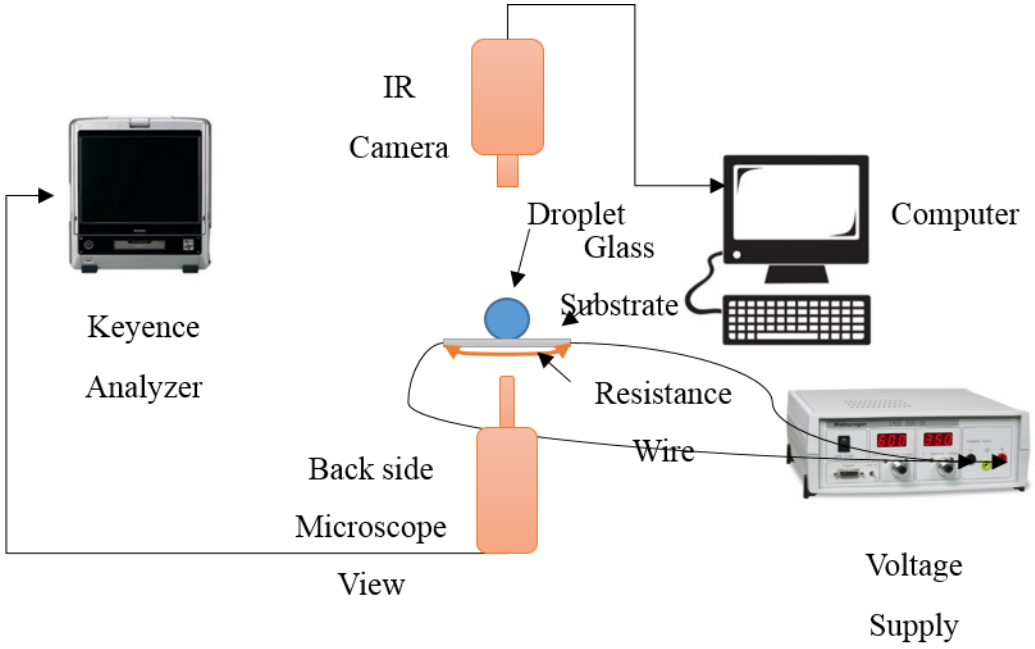
II.2.1 Methodology and experimental setup

II.2.1.1 Infrared and optical measurements

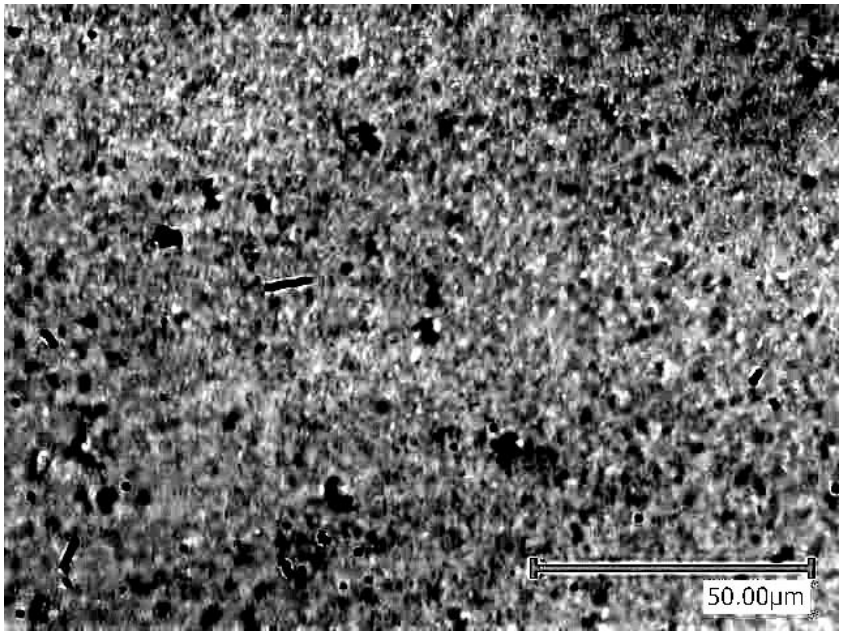
This experimental setup allows to monitor the nanoparticles' precipitation during a drop evaporation. The substrate is heated using two resistance wires surrounding the glass substrate from the edges to homogenize the heating medium using joule effect. The two wires are connected to the voltage supplier to control the temperature, **Fig. II.1**.

Calibration was performed after adjusting the voltage setting for each surface temperature. The infrared camera (FLIR, SC7200, and MW G1 L0905) is installed on the top to undertake an infrared thermal mapping and also to visualize the thermal instabilities on the droplet surface [98]. The evaporation process of droplets is observed and recorded using a high speed camera (Keyence, VW600C) mounted on an optical microscopic lens, connected to a backlight lighting, (Keyence, VH-Z100R, magnification zoom from 100× to 1000×) from the rear side of the substrate in order to monitor the nanoparticles' deposition.

Video editing/analysis software (Keyence, VW-9000 Motion Analyzer) was used to visually track the nanoparticles deposition during the evaporation process. The microscope was focused on the top side of the glass substrate (Glass/Droplet Interface) as shown in **Fig. II.1** during all the experiments then images of dried deposits were taken by the same optical microscopic lens (900× Zoom lens) for different substrate temperatures.



(a)



(b)

Figure II.1. (a) Schematic illustration of the experimental setup for optical and infrared measurements. (b) Contrast image analysis of the CuO nanoparticles on the top side of the glass substrate using ImageJ software.

For these experiments, we used a transparent glass substrate treated with silane (PFTS) molecules. Measurements are recorded at temperatures of 22, 60, 80 and 90°C with a mean humidity of approximately 50%.

Sequential images of all videos recorded during a drop evaporation were analyzed by ImageJ software in order to measure the evolution of intensity density ($\overline{ID}$) during nanoparticles' precipitation. The mean values of *ID* are obtained by measuring the change in the contrast from the images (See Fig. 1.b) at various surface temperatures (22, 60, 80, and 90°C) as a function of time. These values are directly related to the intensity density since the analysis is performed on the same surface area, according to Equation (1):

$$\overline{ID} = ID \text{ /Surface area} \quad (1)$$

The intensity density measurements are completed by analyzing and visualizing the thermal instabilities at the droplet surface.

II.2.1.2 Acoustic measurements

Measurements are made under a controlled atmosphere using an air-conditioning system. A Cascade PM8 prober system is used to control the position of the S/G (signal/ground) probe backside the micro scale level on a piezoelectric transducer as small as 250 µm in diameter to achieve electrical measurements (see **Fig. II.2**).The specificity of the probe is the possibility to achieve an electrical contact at the backside of the wafer on which the piezoelectric transducer was fabricated [99]. These probes are connected to a Rhode & Schwarz ZVA8 Vector Network Analyzer.

We will present the fabrication of ZnO piezoelectric transducers for the purpose of our study (Lille at clean room). These transducers will be able to generate both longitudinal and shear waves as we will see, and they will be characterized according to their electrical and acoustic responses. ZnO is used as a piezoelectric material, sandwiched between two very thin metal electrodes, deposited on a silicon substrate (**Fig. II.2**), using thin film technologies (deposition, lift-off). ZnO has been chosen because of its ease of preparation, compared to the bounding and thinning process of monocrystalline elements such as LiNbO3.

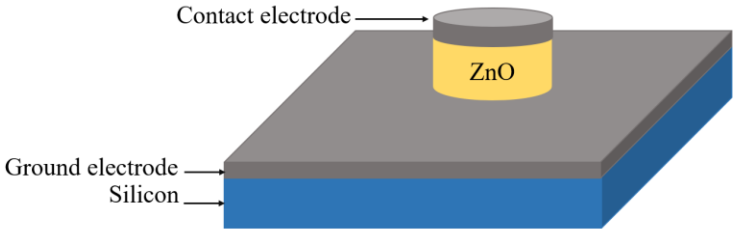


Figure II.2. Multilayer diagram of a piezoelectric transducer.

The process of fabrication of the ZnO piezoelectric transducer first start with the deposition of 10 nm of titanium layer and 80 nm of platinum successively by cathode sputtering on the surface 400 µm thick silicon wafer. These two first layers will act as the lower electrode. Then a lithography process is performed to make the transducers pattern, where a thick 8 µm layer of PMGI SF19 (Microchem Corporation) is then dispensed by spin coating on the lower electrode before a layer of 1.5µm of S1828 (Shipley Corporation) is added.

After UV exposure using a mask, we use a commercial developer MF 319 (Microposit) to obtain a pattern of different diameters in the PMGI layer. After that, 2 µm thin layer thickness of ZnO for the upper electrode of the ZnO transducer are deposited. Finally, we get the transducers through a lift-off process using the solvent SVC 14 to get the transducers pattern. The microfabrication process is shown in **Fig. II.2**.

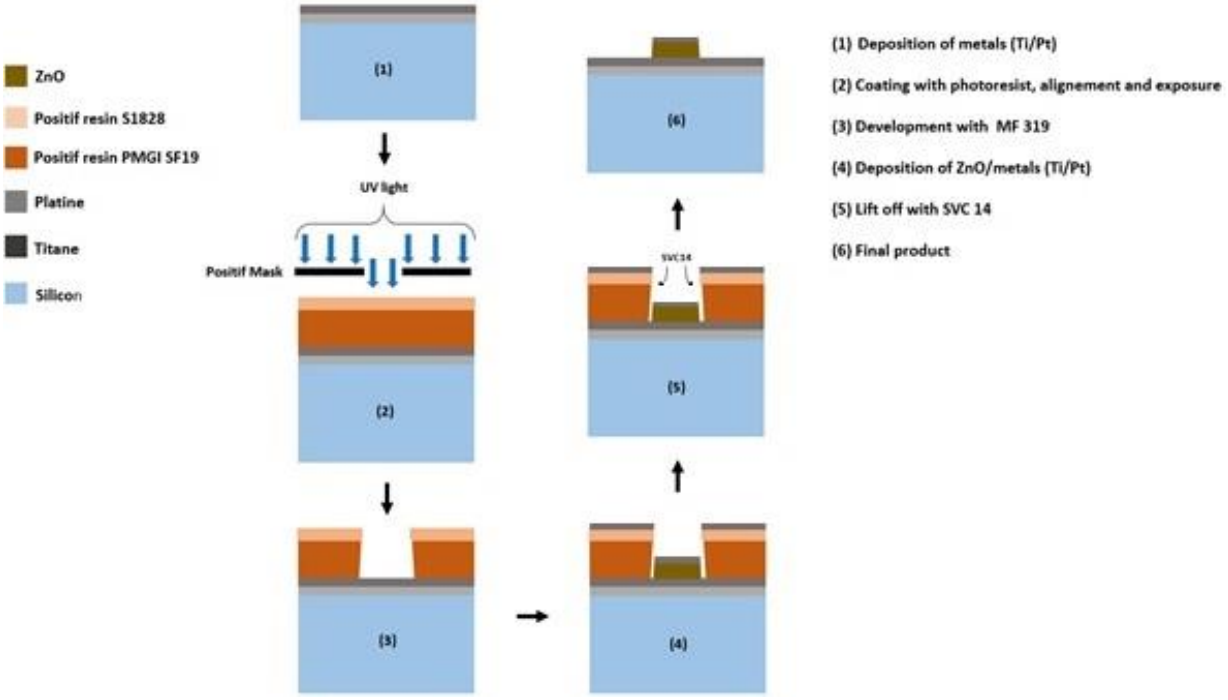


Figure II.3. Transducer fabrication process flow chart.

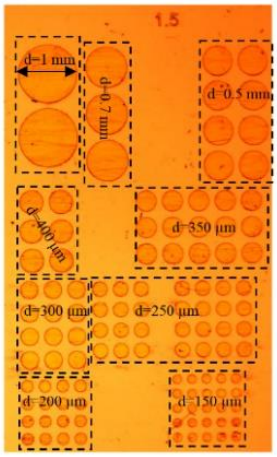


Figure II.4. Image of a network of transducers of different diameters obtained by optical microscopy.

The characterization of the ZnO transducers is carried out using a Rohde & Schwarz Vector Network Analyzer (ZVA8: 300 kHz-8 GHz). It consists of a radio-frequency measuring tip Z-probe, GS type (with a pitch of 1.25 mm) connected by a coaxial cable to the network analyzer. Since we are working with high frequencies of order of Gigahertz, a calibration must be done before each measurement to ensure a good quality of the measurements. The silicon sample on which the transducers are fabricated is placed and maintained by suction (using a vacuum pump) on a circular plate.

The parameter S_{11} shown in **Fig. II.5** as function of the frequency is the output measured by the transducer. This parameter as described by **Eq. 2** is composed of two contributions [100, 101]. The first contribution comes from the direct reflection of the electric wave on the transducer (S_{11}^{el}). The second is a result of all the acoustic wave reflections on the opposite side of the substrate. These acoustic reflections are then converted into electrical signal by the transducer.

$$S_{11}(f)=S_{11}^{el}+K_{11}S_{11}^{ac} \quad (2)$$

The coefficient K_{11} called the coupling coefficient of the piezoelectric transducer used to convert acoustic energy into electrical one, S_{11}^{el} the electric reflection wave while S_{11}^{ac} is the contribution of the whole acoustic reflections before returning to the transducer to be converted into electrical ones. This parameter can be used to estimate the acoustic characteristics of a material.

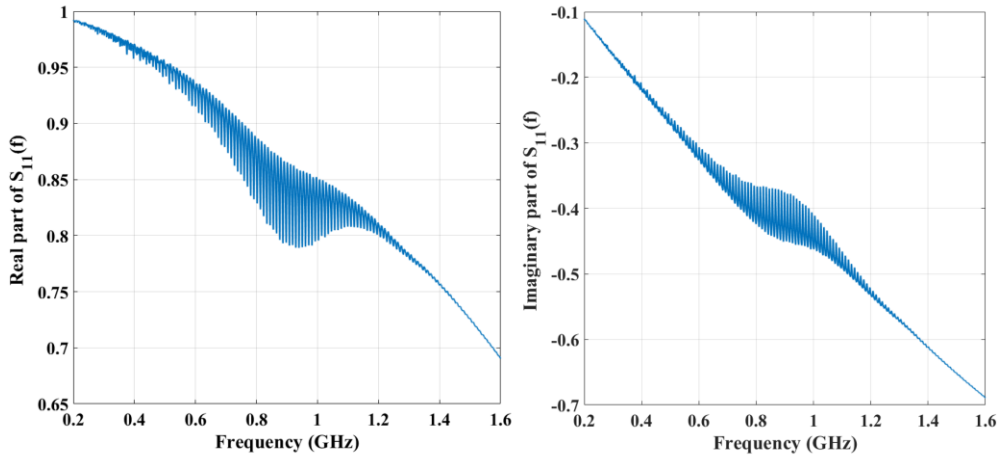


Figure II.5. Parameter S_{11} measured with the network analyzer, (a) real part (b) imaginary part.

The reflection transfer function of our system is represented by S_{11}. To obtain the temporal response an inverse Fourier Transform is performed (**Fig. II.6**). We can see in the time domain, the electrical term response is shortly after the excitation of the transducer while the acoustic term comes later in time.

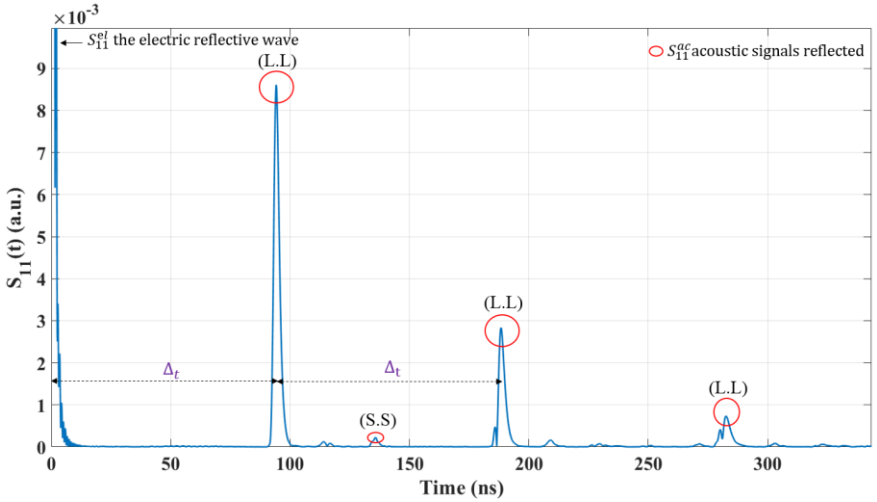


Figure II.6. Impulse response S_{11} (t).

The response shown in **Fig. II.7** demonstrating the rapid oscillation of S_{11} (f) as a function of frequency, showing a peak oscillation around a central frequency of 0.9 GHz. For each emitted wavelength, given the thickness of the wafer, the superposition of the incident and reflected waves occurs with a variable phase shift according to the frequency. As a result, the amplitude of the total vibration measured by the transducer (amplitude of the sum of the incident and reflected wave) is greater for two waves (incident and reflected) in phase and lower for two waves in opposition of phase. This phenomenon is characterized by the SWR standing wave ratio (ratio of the maximum and minimum values of the total vibration). The frequency periodicity of these fast oscillations is $\Delta_f = c_{Si}/2e_{Si}$, where e_{Si} and c_{Si} are the thickness and the celerity of the acoustic wave in the silicon. **Fig. II.5** shows multiple echoes, the first one corresponds to S_{11}^{el}. This electrical echo (reflection) is a direct effect of the non-electrical matching of the transducer to the power line. This delay then corresponds to the electromagnetic wave in the cable portion between the probe and the network analyzer. The other different echoes shown in **Fig. II.5** then, correspond to the reflections back and forth in the silicon of the equivalent pulse S_{11}^{ac}.

The time delay $\Delta_t = 1/\Delta_f = 94$ ns between them corresponds to the propagation delay of the wave travelling twice the thickness of the wafer e_{Si}.

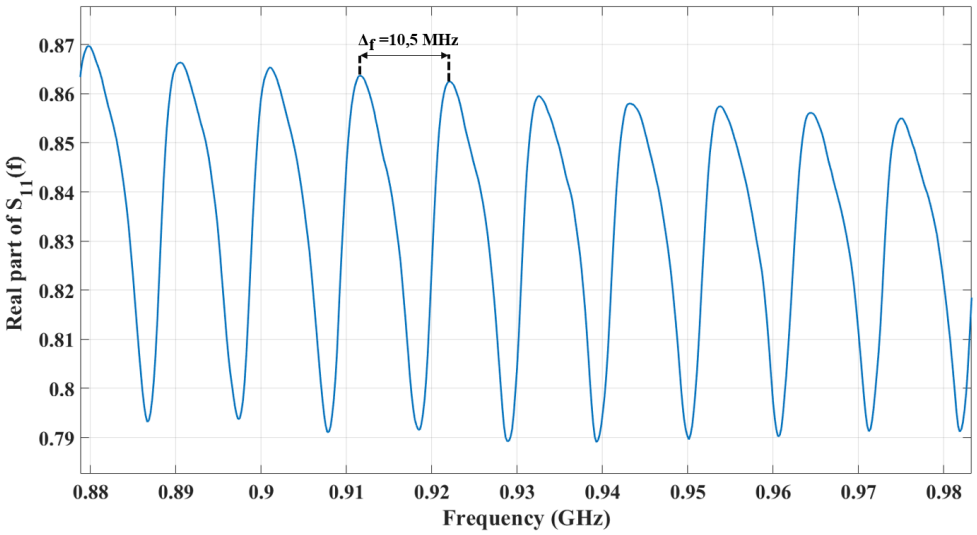


Figure II.7. Zoom around the longitudinal acoustic wave resonance of the transducer.

For the acoustic experiments, we used a hydrophobic silicon substrate. The droplet is deposited on the top side of the silicon substrate *via* a microfluidic device, then a high-frequency (1 GHz) longitudinal wave is generated by ZnO piezoelectric transducers fabricated on the backside of the classical (100) crystal orientation of the silicon substrate on which the solid−liquid interface is characterized. The diameter of the ZnO transducers is about 250 μm. The analysis has a high sensitivity at the liquid/solid interface characterization, which gives us a clear picture of the nanoparticles' deposition on the substrate.

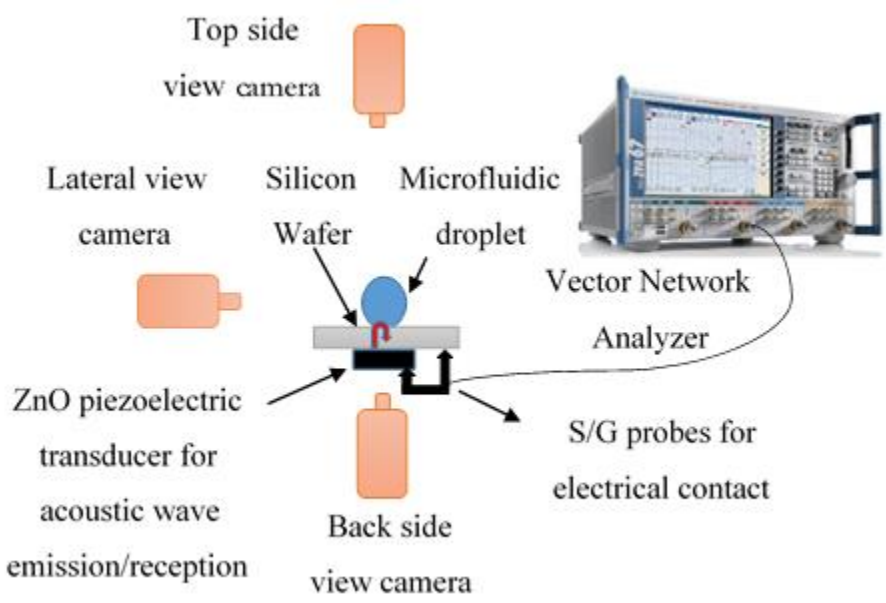


Figure II.8. Schema of the experimental setup of acoustic measurements.

The study is dependent on the mechanical properties at the interface between the silicon substrate and the droplet. It is represented by a reflection coefficient [102]. The formula in equation (3) is related to the mechanical impedance of both the substrate and the liquid deposited at the interface.

$$\left| R \right| = \left| \frac{Z_{nf} - Z_s}{Z_s + Z_{nf}} \right| \quad (3)$$

Where Z = ρC, ρ is the density of the medium, and C is the acoustic velocity of the wave propagating inside of the medium. As a first intension, we will consider only the modulus of R, so that, Z_{nf} the acoustic impedance of the 'nanofluid', and Z_s is the acoustic impedance of the (100) silicon substrate will be real.

II.2.2 Experimental results

To compare the surface properties of the two substrates investigated in our experiments, namely glass and silicon substrates treated each with PFTS, the evolution of the contact angle of a nanofluid drop evaporation on these substrates is followed using a drop shape analyzer to measure the drop contact angle. One can see on **Fig. II.9** that this parameter, measured using the same drop volume, temperature and humidity conditions, follows similar trends. This demonstrates that the two substrates treated with PFTS share the similar surface properties.

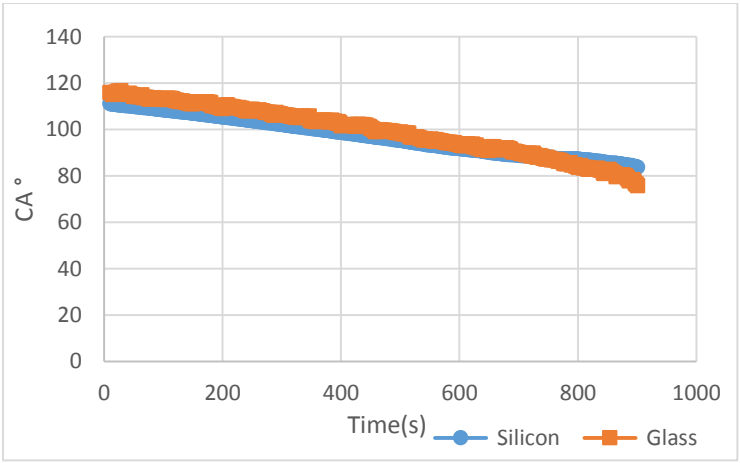


Figure II.9. Contact angle evolution of 0.05wt % CuO-water nanofluid droplet on a non-heated substrate at 22°C.

II.2.2.1 Calibration of the acoustic measurement method: Water as a reference liquid

Several precautions are taken to improve the accuracy of the measurements. Temporal drifts are minimized by the use of two identical transducers, one as a reference to air and the other one for the measurement at the silicon-liquid interface [99].

A drop of water is deposited on the hydrophobic silicon surface where the transducer (250 µm in diameter) is located. An acoustic wave is generated by the ZnO transducer through the substrate to the interface. The acoustic device is calibrated using water as a reference liquid at ambient temperature.

The acoustic reflection coefficient is calculated using equation (3) with the physical properties of water and (100) silicon substrate at 22°C as reported in **Table II.1** [103, 104]. **Table II.1** [105] is also summarized the values of the Young modulus of the two constituents of the nanofluid, namely water and copper oxide. The amplitude coefficient is determined to be 0.8595. The experimental result, as shown in **Fig. II.10**, demonstrates a good reliability of the measured amplitude coefficient $|R| = 0.8594 \pm 0.01\%$.

Fluids/ Medium	Density, ρ ($kg \cdot m^{-3}$)	Surface Tension, γ ($mN \cdot m^{-1}$)	Young Modulus, E (Gpa)	Acoustic Velocity, C_L ($m \cdot s^{-1}$)
Water	998	72.8	2.2	1488
Silicon	2330	-	-	8433
CuO	6310	-	95	3891

Table II.1. Physical properties of water, copper oxide and silicon at 22 °C.

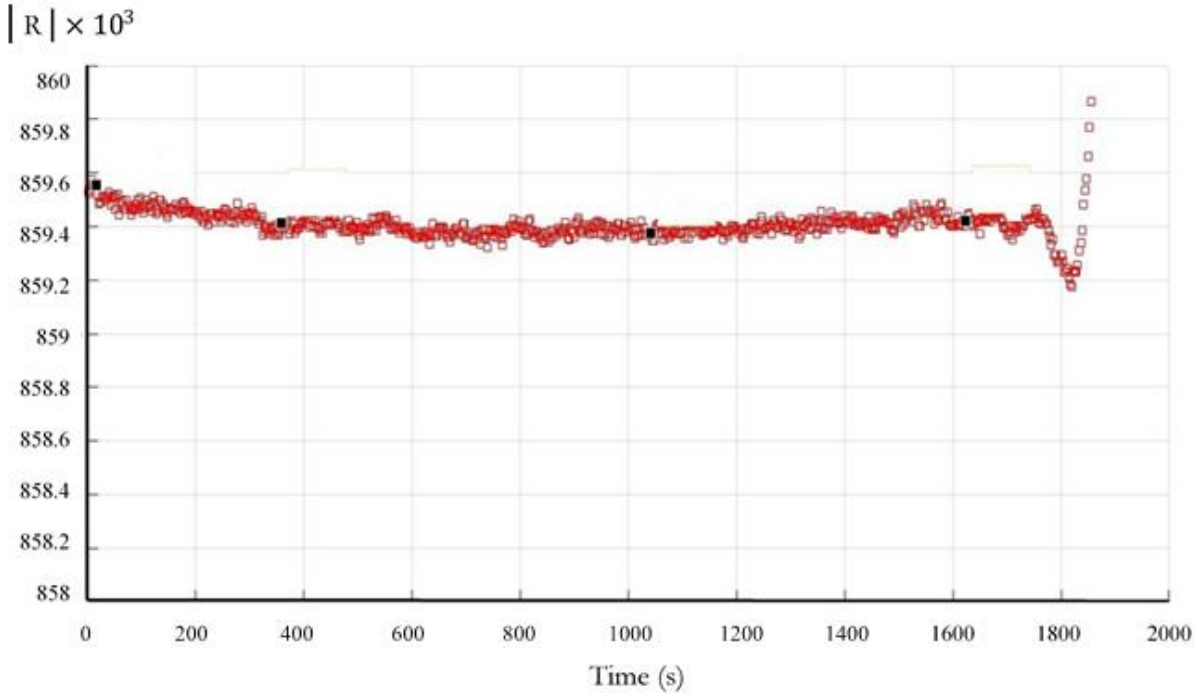


Figure II.10. Reflection coefficient evolution of a 6 µL pure droplet of water during evaporation process at 22°C.

II.2.2.2 Optical, infrared and acoustic measurements of CuO-water droplet at ambient temperature

The evaporation process of 6 µL CuO-water droplet at ambient temperature is followed from the rear side of the glass substrate to monitor the nanoparticles' deposition and predict the time from which the particles start to precipitate. A Keyence microscope with 800× magnification focused

on a surface area of 250 µm, corresponding to the area of interest of the acoustic measurements, namely the transducer diameter.

The analysis depends on the mean intensity density ($\overline{ID}$) extracted from ImageJ software at the solid-liquid interface on the one hand and on the thermal mapping at liquid-air interface on the other hand. A variation of intensity density ($\overline{ID}$) as a function of time is displayed in **Fig. II.11**.

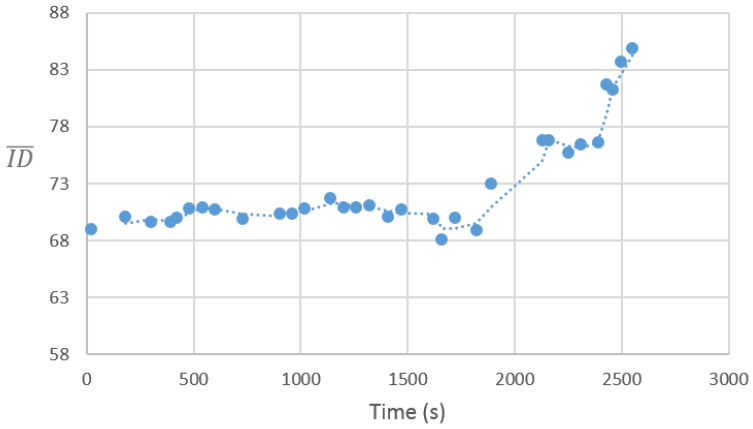


Figure II.11. Mean values of the precipitated CuO nanoparticles on the hydrophobic glass substrate at 22°C.

The graph shows a very slight change at the beginning of the droplet evaporation whereas a clear variation is evident after 1950 s. This alteration, due to CuO nanoparticles deposition on the glass substrate, occurs after a period of time corresponding to 73% of the whole evaporation process. At the same time, the infrared camera at this surface temperature did not catch any thermal variation on the surface of the droplet because of the very low temperature gradient.

Under these conditions, a final pattern shape of nanoparticles deposited on a non-heated hydrophobic substrate was observed (using Keyence microscope) and was presenting an inner deposition without any ring formation.

This shape pattern, analyzed using ImageJ software to examine the nanoparticles distribution on the glass substrate at the end of the evaporation process, is displayed in **Fig. II.12**.

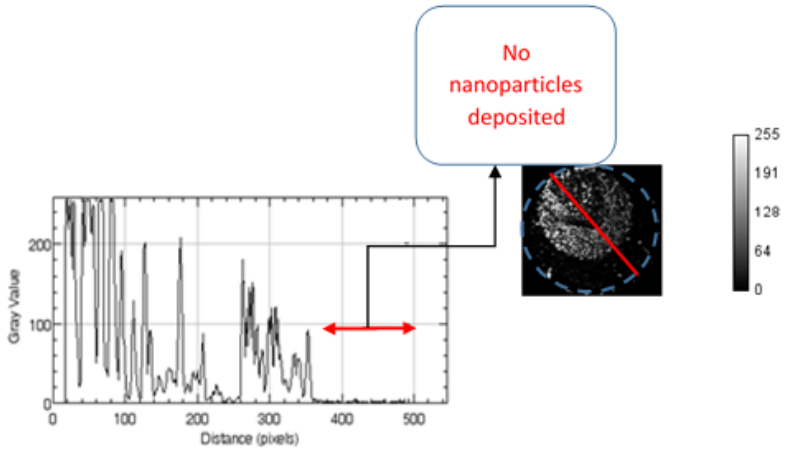


Figure II.12. Dried deposits of 0.05wt % CuO-water nanofluid droplet on a non-heated substrate (22°C) with the distribution surface profile using ImageJ software.

In the following, the optical results are compared to those obtained using the acoustic method. A drop of same volume of 6 µL (0.05% CuO/water nanofluid) is deposited on a hydrophobic silicon substrate where the transducer is located. The amplitude of the reflection coefficient is then measured during the whole process of evaporation at ambient temperature of 22°C and 50% humidity. The evaporation kinetics, analyzed through the amplitude of the reflection coefficient, is depicted in **Fig. II.13**.

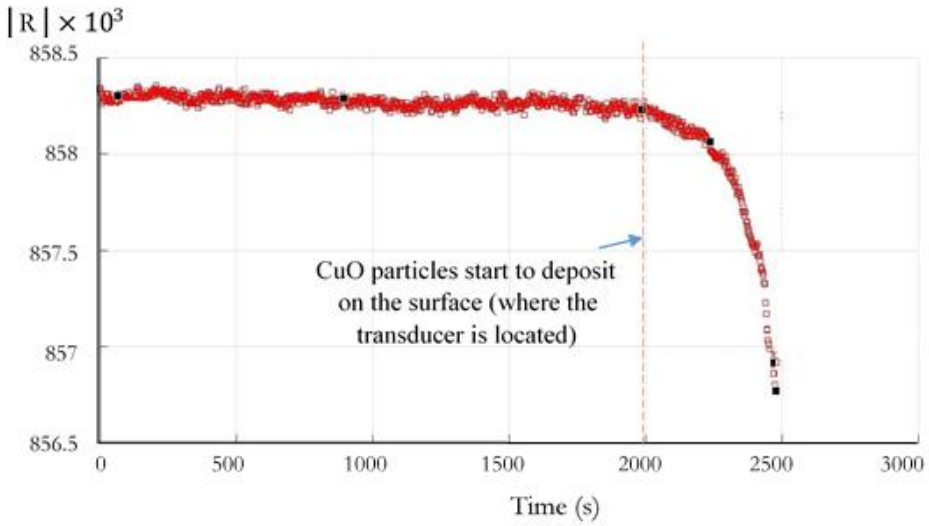


Figure II.13. Reflection coefficient evolution of 0.05wt % CuO-water nanofluid droplet on a non-heated substrate (T=22°C).

One can see that the amplitude of the reflection coefficient remains constant during about 2000 s then begins to decrease. This is primarily ascribed to a change of the physical properties of the material interacting with the ultrasounds at the interface. This rapid evolution is clearly due to the precipitation of CuO nanoparticles on the silicon substrate above the transducer. The delay of the time (2000s) before the particles begin to settle is consistent with the one deduced from the optical observation which was worth 1950s, under the same conditions.

The final deposition pattern illustrated in **Fig. II.14** gives the same deposit form as that on the hydrophobic glass substrate shown in **Fig. II.12**.

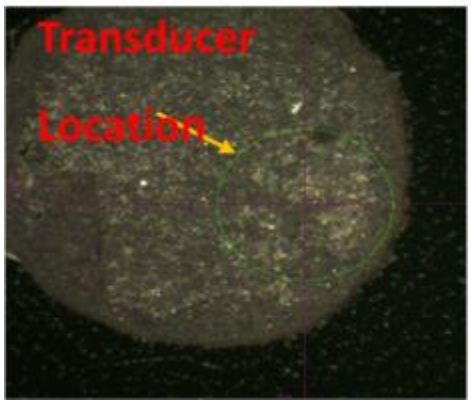


Figure II.14. Dried deposits of 0.05wt % CuO-water droplet during acoustic measurements.

The amplitude of the reflection coefficient can give access to the volume fraction of the nanoparticles v_p that settles during the evaporation of the drop. To this end, based on the assumption of a low concentration of particles, one can apply the mixed rules equation to the Young's Modulus E_{nf} as well as to the density ρ_{nf} of the nanofluid (given in equations 4 and 5), which is composed of water and copper oxide particles. Knowing that the ultrasonic velocity propagating inside the nanofluid can be expressed as a function of E_{nf} and ρ_{nf} as mentioned in equation (6), one can then introduce it in the expression of the reflection coefficient given in equation (3). The density and the Young's Modulus of the two constituents of the nanofluid, namely particles and water, are given in **Table II.1**.

$$E_{nf} = v_p \times E_p + (1 - v_p)E_\omega \quad (4)$$

$$Z_{nf} = \rho_{nf} \times C_{nf}$$

$$\rho_{nf} = v_p \times \rho_p + (1 - v_p)\rho_\omega \quad (5)$$

$$C_{nf} = \sqrt{\frac{E_{nf}}{\rho_{nf}}} \quad (6)$$

Where $\rho_{nf,}$ ρ_p, ρ_ω are the densities of nanofluid, copper oxide nanoparticles and water, respectively. From the experimental kinetics of the reflection coefficient, considering a new time reference at t=2000s, from which the particles begin to settle, one can calculate the volume fraction of particles v_p (**Table II.2**) and then deduce the evolution of v_p as a function of time during the process, as shown in **Fig. II.15**.

$\lvert R \rvert$	v_p %
0.8583	0
0.8583	0
0.85825	0.03
0.8582	0.06
0.8581	0.07
0.8569	0.15
0.8568	0.16

Table II.2. Volume fraction percentage of CuO nanoparticles as a function of the acoustic reflection coefficient.

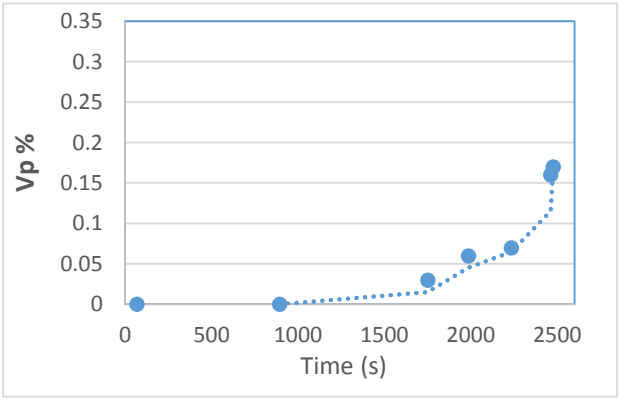


Figure II.15. Volume fraction percentage of CuO nanoparticles on the transducers during evaporation process.

In order to evaluate the accuracy of the mixed rules equation applied to the Young modulus of the nanofluid, given in equation (3), the effective Young Modulus E_{eff} of the nanofluid is calculated for each volume fraction v_p presented in **Table II.2**, using a finite element model developed on FreeFem software. The model is based on the weak formulation variation [106] of the static equilibrium equation of the mixture. The droplet is considered as a set of periodic unit cells, as shown in **Fig. II.16a**. Each unit cell contains 2 particles.

The main objective of the finite elements code is to provide the effective properties for the corresponding unit cell which contains the two phases constituting the nanofluid: water and particles, as shown in **Fig. II.16b** [107, 108].

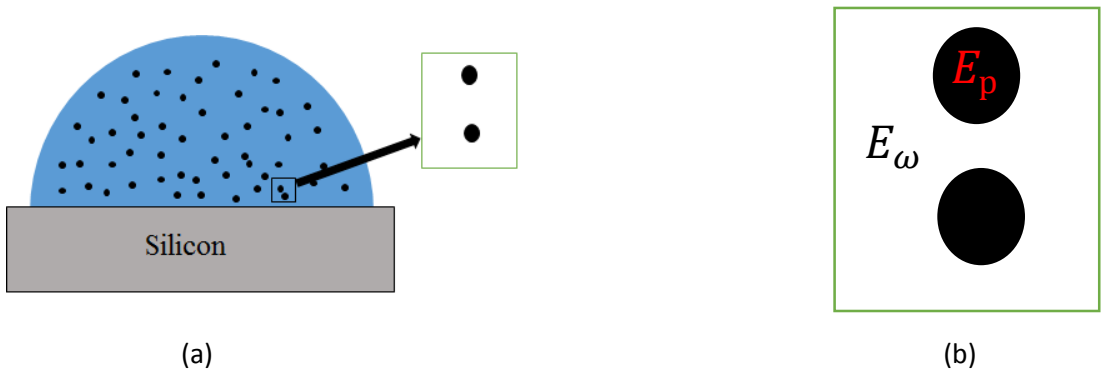


Figure II.16. (a) Periodic unit cell at the interface; (b) Unit cell representation of matrix periodic structure (water and copper oxide particles).

As can be seen from **Fig. II.17**, the evolution of the Young Modulus, E_{eff}, exhibits the same behavior and trend as the Young Modulus Enf deduced from the simple mixed rules equation. The value of the Young Modulus at the beginning of the evaporation process was 2.2 Gpa which corresponds to the one of water. After that a slight change in the values of Enf obtained from the simple mixed rules can be observed within 1% relative error. The finite element method may be considered more trustable compared to the simple mixed rule.

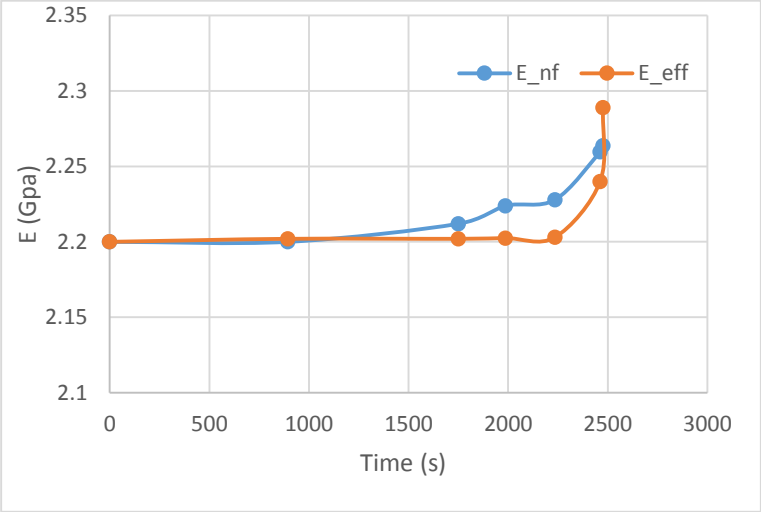


Figure II.17. Comparison between the kinetics of the Young Modulus E_{eff} obtained from a finite element model and the Young modulus E_{nf} calculated from the simple mixed rules.

II.2.2.3 Effect of substrate temperature on nanoparticles deposition

After validation of the optical method at ambient temperature, thanks to the acoustical one, the same procedure is repeated for different substrate temperatures (60, 80 and 90°C). The variation of the mean intensity density values for each substrate temperature is depicted in **Fig. II.18**. For the substrate temperature of 60°C, the nanoparticles started to deposit after 26 s which corresponding to a relative time t^* of 50% of the whole evaporation process. The relative time t^* drops to 27% and 10% for 80 and 90°C substrate temperature, respectively, as shown in **Table II.3**.

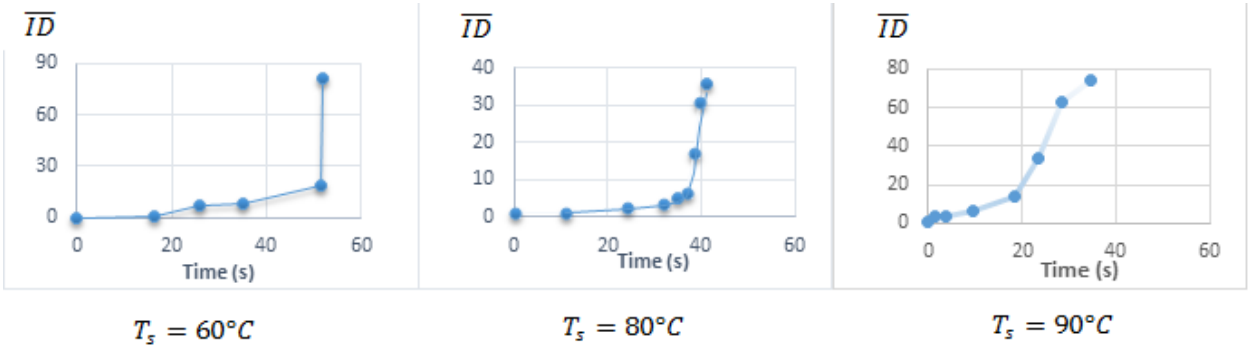


Figure II.18. Mean values of the CuO nanoparticles precipitation on the hydrophobic glass substrate during droplet evaporation at different surface temperatures (60, 80 and 90°C).

T_s	t (s)	$\overline{ID}$	t^*(%)
22	1950	70	73
60	26	7.5	50
80	11	1.3	27
90	3.5	4	10

Table II.3. Influence of the substrate temperature on the intensity density of the deposited nanoparticles and their deposition time.

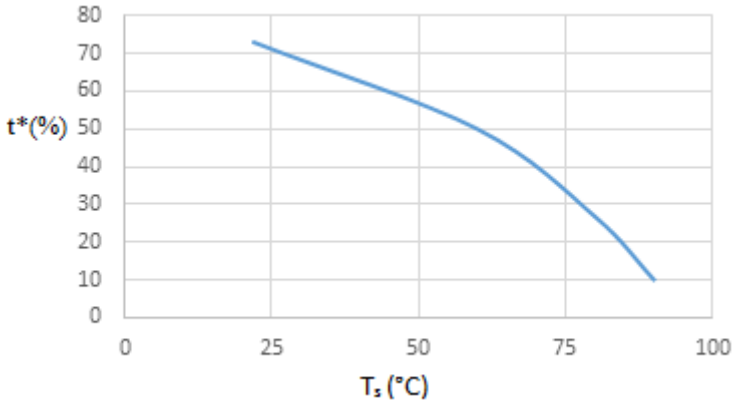
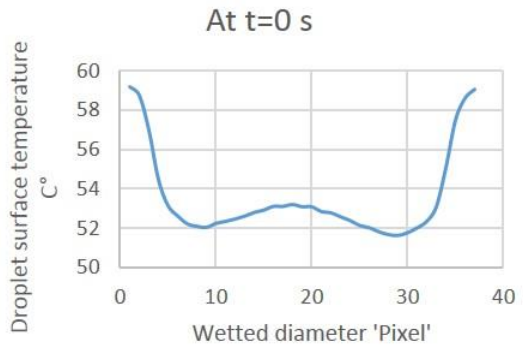
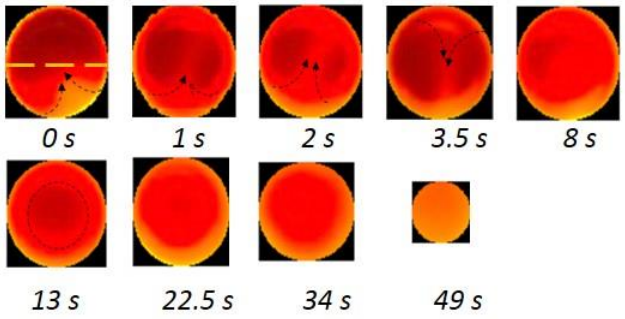


Figure II.19. t^* the percentage of time that CuO nanoparticles begin to deposit on a substrate for different substrate temperatures.

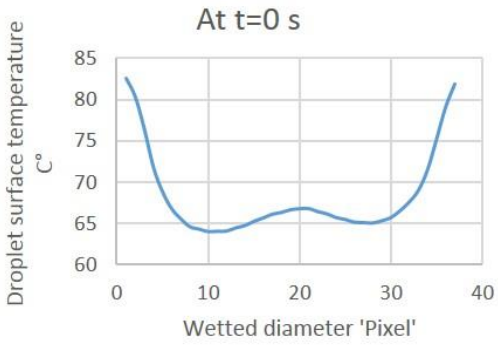
At the same time, the infrared camera made it possible to measure the surface temperature of the droplet at liquid/air interface for each substrate temperature. As illustrated in **Fig. II.20**, a gradual change in temperature distribution on the drop surface is observed. This phenomenon is assigned to convection cells inside the droplet due to thermal Marangoni effect. As illustrated from the infrared mapping in **Fig. II.20**, the Marangoni flow is represented by thermal instability at the droplet surface.

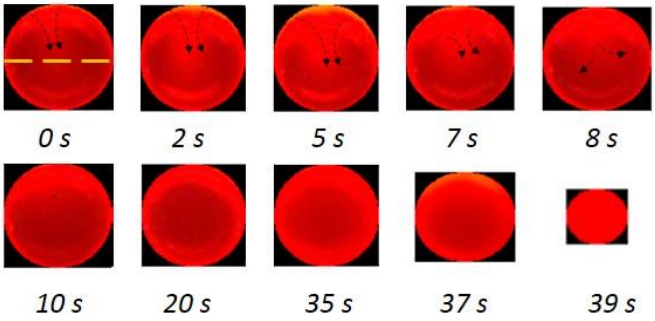




$T_s = 60°C$

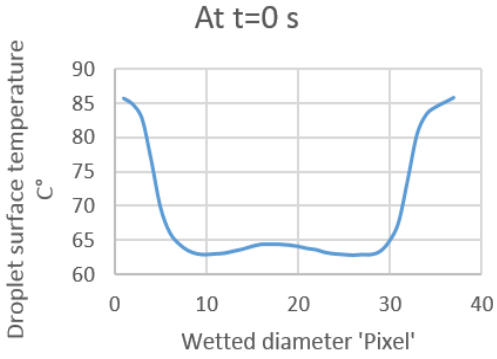
(a)

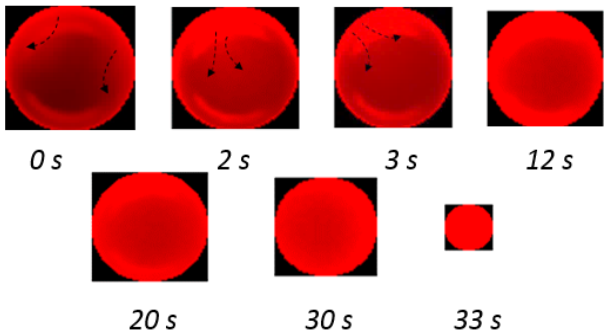




$T_s = 80°C$

(b)





$T_s = 90°C$

(c)

Figure II.20. Snapshots from an infrared video of the evaporation process of a CuO-water nanofluid droplets at different substrate temperatures (a) 60°C (b) 80°C (c) 90°C, along with droplet surface temperature distribution profiles.

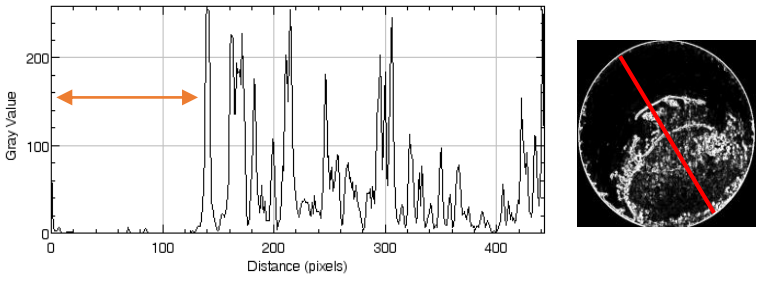
One can notice that the lifetime of the observed convections cells, is inversely related to the substrate temperature (**Table II.4**). Moreover, for each substrate temperature, the lifetime of the convection cells matches with the time after which the particles begin to deposit on the substrate, as reported in **Table II.3**. The Marangoni cells can be observed clearly from the images that present changes in the surface gradient temperature. So the life time was estimated when no more Marangoni cells were observed in the images using the infrared camera.

Ts (°C)	60	80	90
Convection cells lifetime (s)	20	10	3

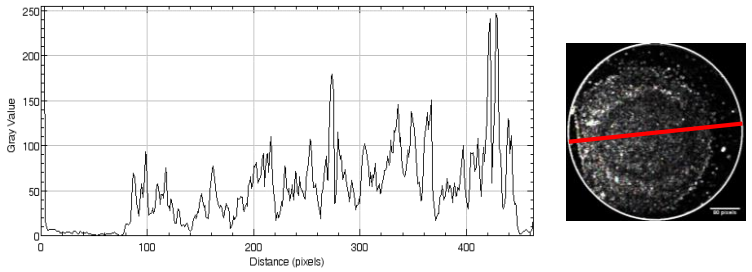
Table II.4. Lifetime of the convection cells as a function of the substrate temperature.

Convection cells, linked to the Marangoni flow, keep the nanoparticles moving in a circulation path, causing then a delay in the particles deposition during droplet evaporation.

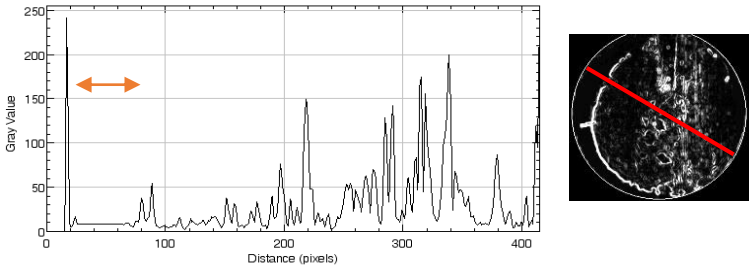
The effect of the substrate temperature on the final pattern shape of the nanoparticles is observed in **Fig. II.21a**. A ring shape with inner deposit is observed with an increase in the area D^* of the nanoparticles deposited on the surface (**Fig. II.21b**).



$T_s = 60°C$

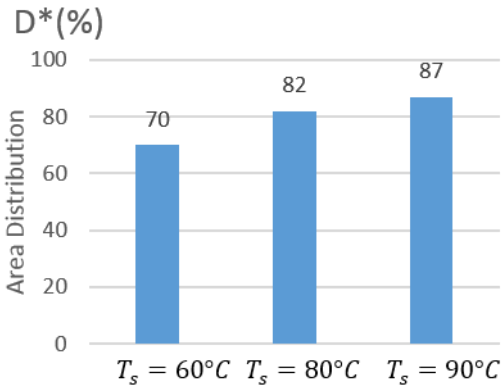


$T_s = 80°C$



$T_s = 90°C$

(a)



(b)

Figure II.21. (a) Dried deposits of 0.05wt % CuO-water nanofluid droplet at different substrate temperatures 60, 80, and 90°C with the CuO distribution using ImageJ software, scale bar from 0 to 256 pixels; (b) Nanoparticles area distribution as surface temperature increased.

II. 3 Dynamic viscosity measurements of gold nanofluids using high frequency acoustic method (≈1GHz)

The study is dependent on the mechanical properties at the interface between the silicon substrate and the droplet. It is represented by two complex reflection coefficients for the longitudinal and shear waves. The formula in **Eq. (7)** is related to the mechanical impedance of both the substrate and the liquid deposited at the interface in a complex form.

$$r^* = \frac{Z_{nf}^* - Z_s}{Z_s + Z_{nf}^*} \quad (7)$$

Where Z = ρC, ρ is the density of the medium, and C is the acoustic velocity of the wave propagating inside of the medium. In our case, Z_s is the real acoustic impedance of the (100) silicon (Crystalline orientation of the silicon crystal) [109] substrate and Z_{nf}^* is the complex acoustic impedance taking into account the attenuation in the droplet nanofluid (Viscoelastic). The complex reflection coefficient can be written as follow:

$$r^* = |r| exp(i\emptyset) \quad (8)$$

Where $|r|$ is the modulus of the reflection coefficient, ϕ the phase angle between the incident and reflected wave. We present in **Table II.5**, at room temperature, the longitudinal, shear speed of sound and the density of silicon in order to identify subsequently the acoustic impedances in each case.

Medium	Longitudinal Acoustic Velocity, C_L (m/s)	Shear Acoustic Velocity, C_T (m/s)	Density, ρ (kg.m^{-3})
Silicon	8434	5843	2300
Water	1488.319	88	998

Table II.5. Physical properties of silicon and water at ambient temperature. [110]

The reflection coefficients are determined for both longitudinal reflected waves and shear reflected waves during droplet evaporation process. The shear viscosity measurement will be obtained from the modulus and the phase angle of the shear waves. The expression of the complex shear reflection coefficient, r_{TT}^* is given in eq. (9). The complex shear wave number k_T^* is correlated to r_{TT}^* as in equation (10).

$$r_{TT}^* = \frac{Z_{nf}^* - Z_{si}}{Z_{si} + Z_{nf}^*} = \frac{\rho_{nf} C_T^* - Z_{si}}{Z_{si} + \rho_{nf} C_T^*} = \left| r \right| exp(i\emptyset) = A + iB \quad (9)$$

$$C_T^* = \omega / k_T^*$$

Where ρ_{nf} is the density of nanofluid, C_T^* is the complex shear velocity in nanofluid, ω the pulsation of the incident wave and k_T^* the complex shear wave number. From these equations, we can know the complex shear wave number in function of shear refection coefficient.

$$k_T^* = \frac{k_{si}\rho_{nf}(1 - r_{TT}^*)}{\rho_{si}(1 + r_{TT}^*)} = a - jb \quad (10)$$

Where k_T^* can be express as follow:

$$k_T^* = {}^{\omega}/_{C_T} - i\alpha_T = {}^{\omega}/_{C_T} - i\sqrt{\frac{\rho_{nf}\omega}{2\mu_s}} \quad (11)$$

Where C_T the effective shear velocity in nanofluid, α_T is the shear attenuation and μ_s is the shear viscosity . One can see that from the kinetics of both the modulus and the phase angle of the shear wave, the shear viscosity can be deduced at the interface between the substrate and the nanofluids droplet during its evaporation.

II.3.1 Experimental setup

In this work, the studied nanofluid consists of gold (Au) nanoparticles (Sigma Aldrich, 5 nm diameter, OD 1, stabilized suspension in 0.1 mM PBS, reactant free with volume concentration of 4% C_v) dissolved in distilled water and then stabilized through ultra-sonication (Elma, S 10/H) for at least 1 h before use.

The experimental set up is similar to the one used in a previous study [Zaaroura et al., 2018] [111]. Measurements are made on a high frequency echography principle and under a controlled atmosphere using an air-conditioning system. The measurements procedure is the same in the analysis of CuO nanoparticles stability at the liquid/solid interface. (See **Fig. II.22**).

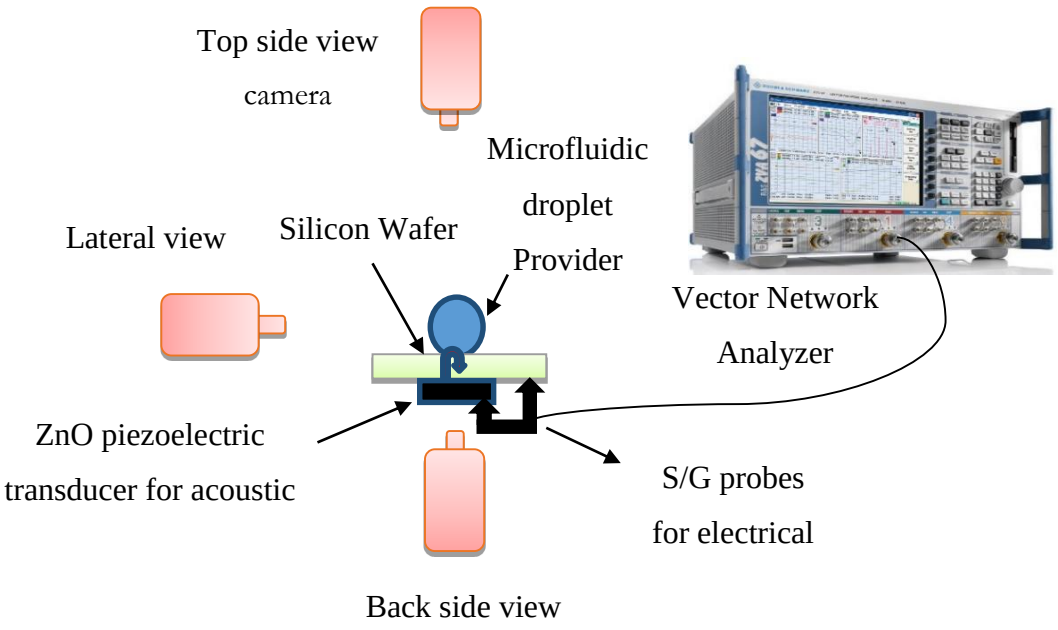


Figure II.22. Schema of the experimental setup of acoustic measurements. [111]

To ensure and verify the accuracy of our method, the used transducer was fabricated by me and at specific technique in order to generate more shear waves since it is the most sensitive parameter to extract the shear viscosity. This method known as a blind technique [112], see **Fig. II.23**, the ZnO film was deposited a wafer with the following stack: Pt (80 nm) / Ti (10 nm) / Si (400 µm) by RF magnetron sputtering technique.

The substrate was fixed in the chamber whose total pressure was 0.02 mbar. A rectangular cover is positioned between the target and the substrate, making it possible to obtain oblique incidence of the particles without having to tilt the wafer in order to locally influence the growth of the film. The blind was made of aluminum, had a height of 10 mm and a thickness of 2 mm. It was placed in the center of the substrate. The deposition rate of the ZnO films varied from 15 to 25 nm/min.

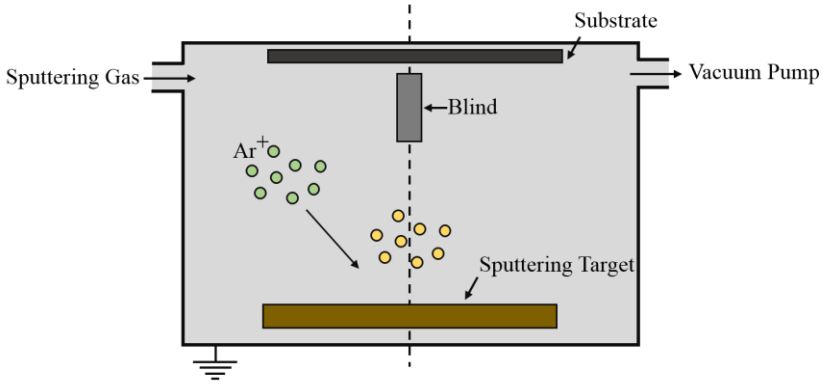


Figure II.23. Rf. magnetron sputtering system with additional blind between substrate and target.

The results presented in **Fig. II.24** and **Fig. II.25** as we can see the two distinguished downward peaks, the first one in the frequency range [0.4-0.8 GHz] which corresponds to important transversal waves response, and the other peak in the range [1-2 GHz] which corresponds to important longitudinal waves response.

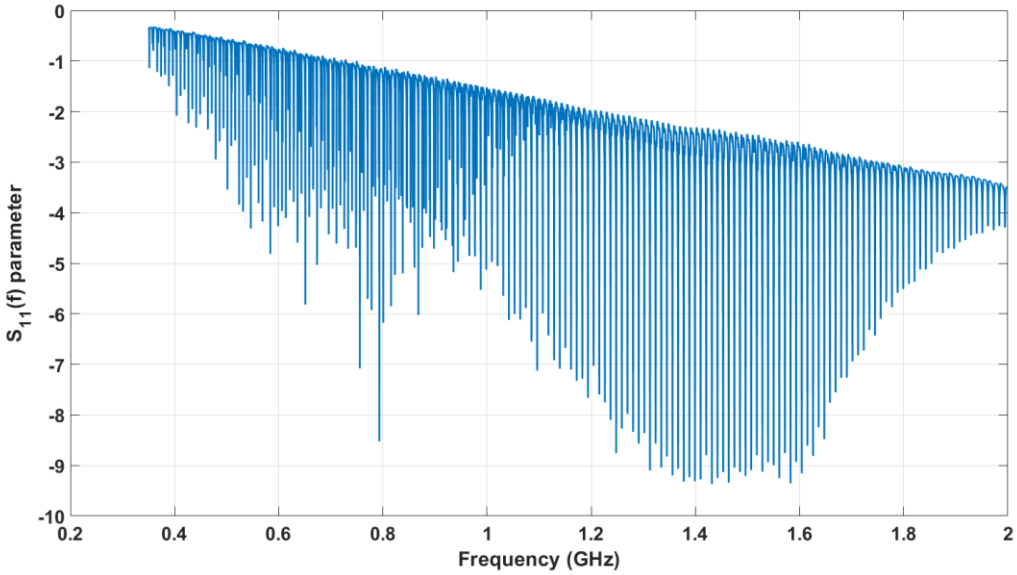
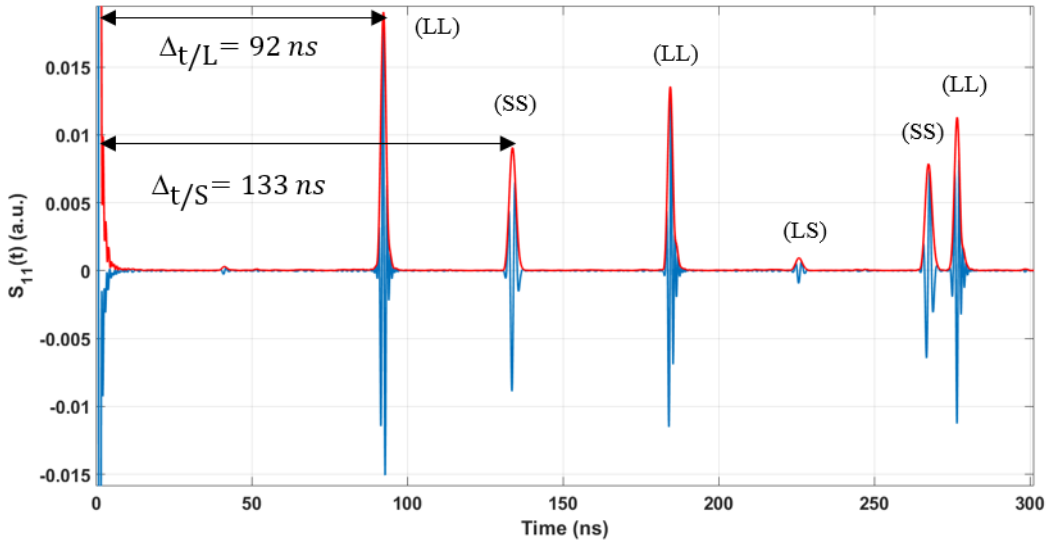
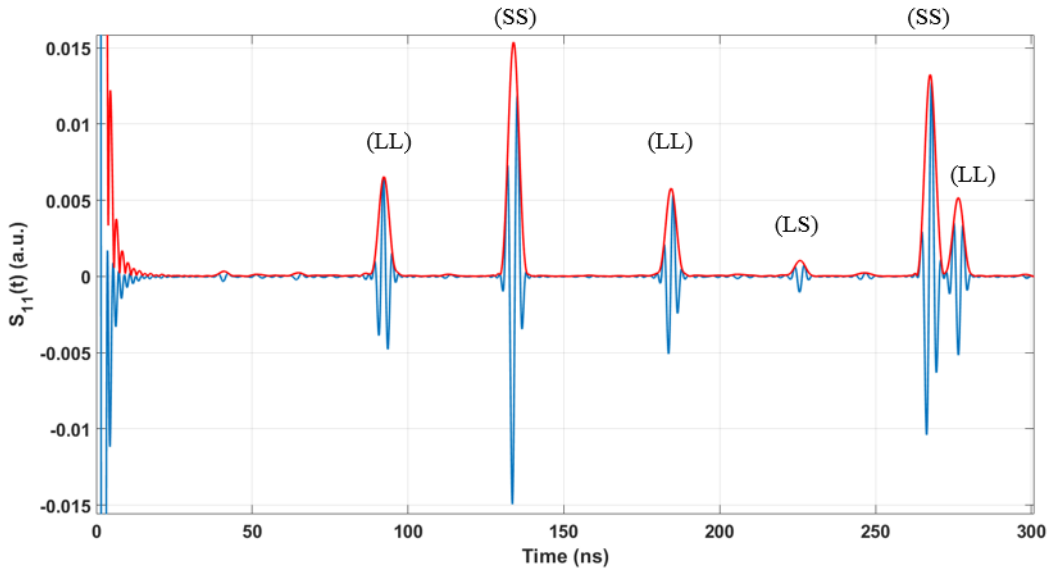


Figure II.24. Parameter S_{11} (f) measured with the network analyzer.



(a)



(b)

Figure II.25. Corresponds to the impulse response$S_{11}(t)$, the time delays $\Delta_{t/L}= 1/\Delta_{f/L}$ =92 ns and $\Delta_{t/S}= 1/\Delta_{f/S}$ =133 ns between them corresponds to the propagation delays of the longitudinal and transverse wave travelling twice the thickness of the wafer. (a) f = [0.3-2 GHz], (b) f = [0.3-0.6 GHz].

Finally, the use of the screen (blind) during the ZnO sputtering process changes the orientation of the crystal film of ZnO, thus increasing the efficiency of production of transverse waves by the deposited piezoelectric transducers, which is evident by the two peaks shown in **Fig. II.25**.

The amplitude of the reflected wave will depend on the range of operating frequencies chosen, the lower frequencies favoring the transverse waves. Therefore, the choice of frequency range should be made with caution depending on the objectives.

II.3.2 Results and discussion

II.3.2.1 Calibration of the acoustic measurements method: Water as a reference liquid

Several precautions are taken to improve the accuracy of the measurements. A drop of water is deposited on the hydrophobic silicon surface where the transducer (250 µm in diameter) is located. An acoustic wave is generated by the ZnO transducer through the substrate to the interface.

The acoustic device is calibrated using water as a reference liquid at ambient temperature. The acoustic longitudinal reflection coefficient (amplitude) is represented in **Fig. II.26** and **Fig. II.27** presents the shear and longitudinal phase angles variation.

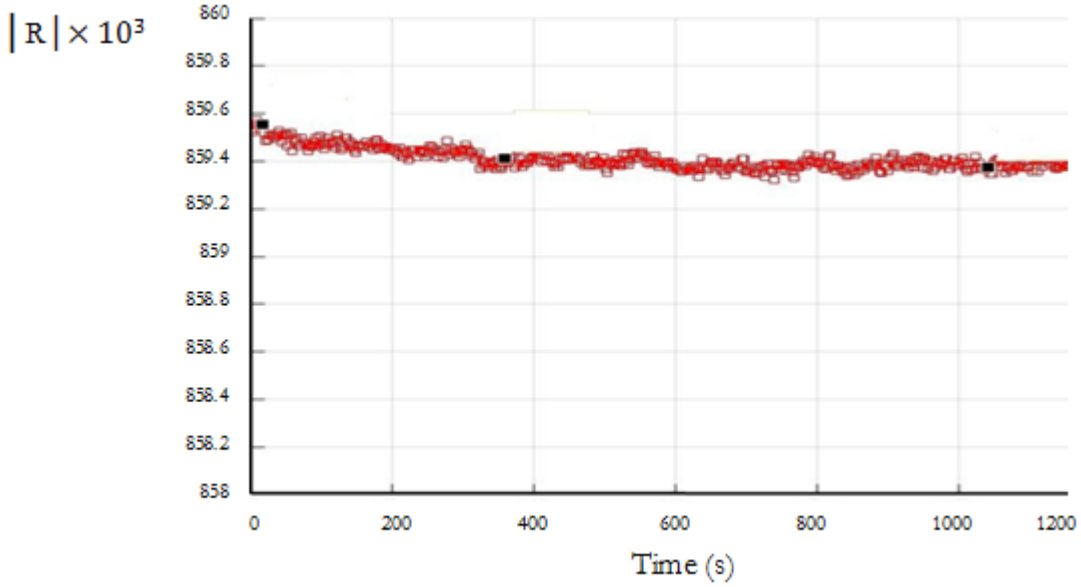


Figure II.26. Longitudinal reflection coefficient modulus evolution of pure water droplet during evaporation process at 22°C.

The amplitude coefficient is determined to be 0.8595 theoretically since we know all the physical properties of water. The experimental result, as shown in **Fig. II.26**, demonstrates a good reliability of the measured amplitude coefficient $|R| = 0.8594 \pm 0.01\%$. The longitudinal r_{LL} and shear r_{TT} phase angles are represented in **Fig. II.27**.

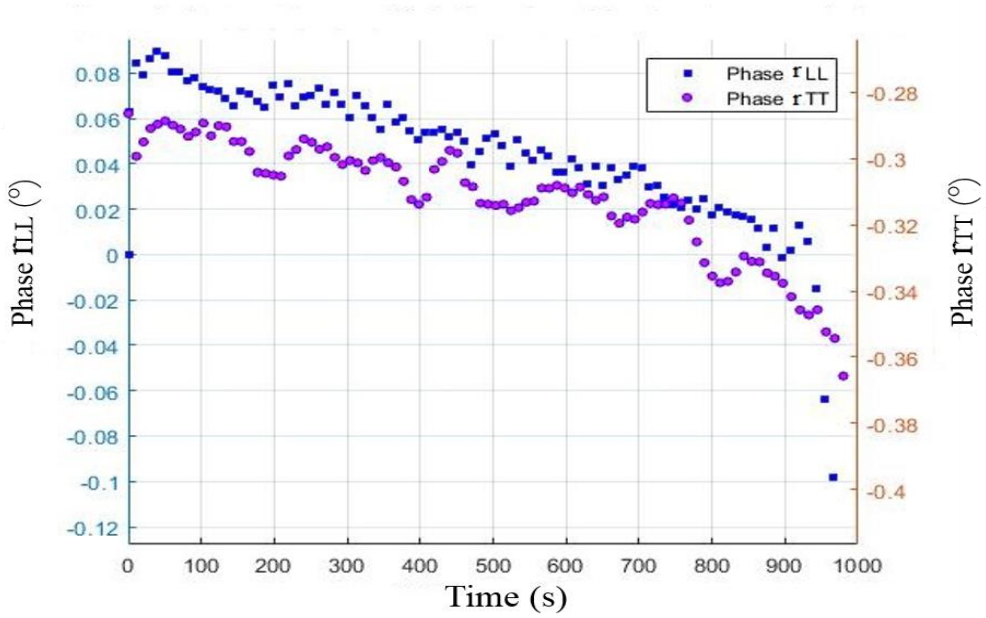


Figure II.27. Phase angles evolution of pure water droplet during evaporation process at 22 °C.

II.3.2.2 Values of dynamic viscosity of gold nanofluid during the evaporation of 4%Cv Au-water droplet

The values of the modulus and phase angle of the reflected waves (shear and longitudinal) sent to the interface was found throughout the evaporation process, **Fig. II.28** and **Fig. II.29.**

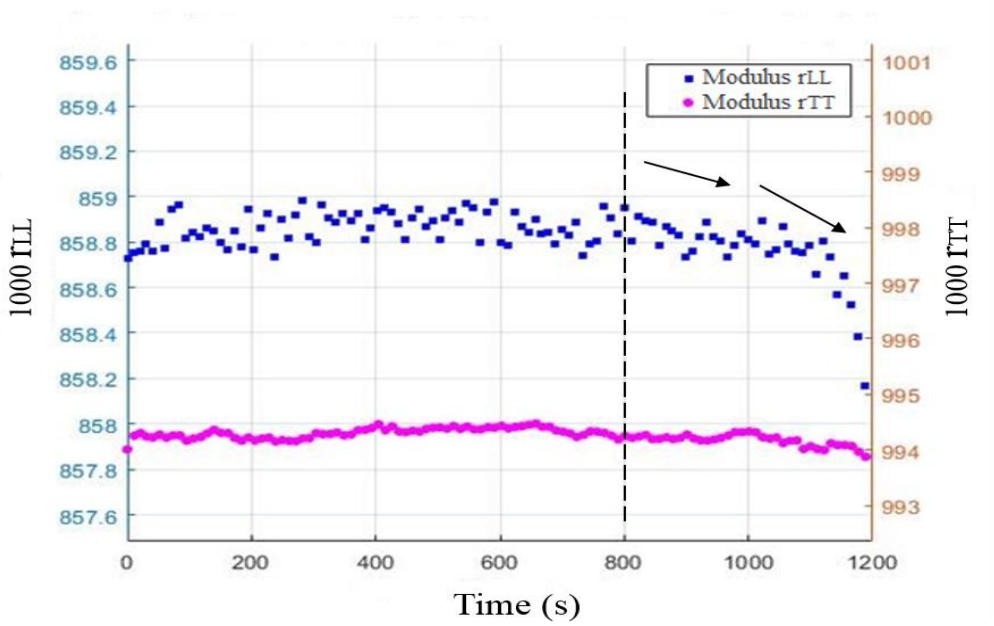


Figure II.28. Modulus reflection coefficient (r_{LL} and r_{TT}) evolution of 4% C_v Au-water nanofluid droplet on a silicon substrate at room temperature.

We can observe from **Fig. II.28** that reflection coefficients in both longitudinal and shear cases kept constant during about 800 s then begin to slight decreasing. This is primarily ascribed to a change of the physical properties of the material interacting with the ultrasounds at the interface. This evolution (after 800 s) is clearly due to the precipitation of Au nanoparticles on the silicon substrate above the transducer. The delay in the gold particles deposition due to the good stability of these particles after suspension in 0.1 mM PBS. This slight decrease refers to a low percentage of particles of gold deposited at the surface. The variation of the longitudinal reflection coefficient is clearer than shear coefficient because of a lesser sensitivity in the measurements of the shear reflected waves compared to the longitudinal ones.

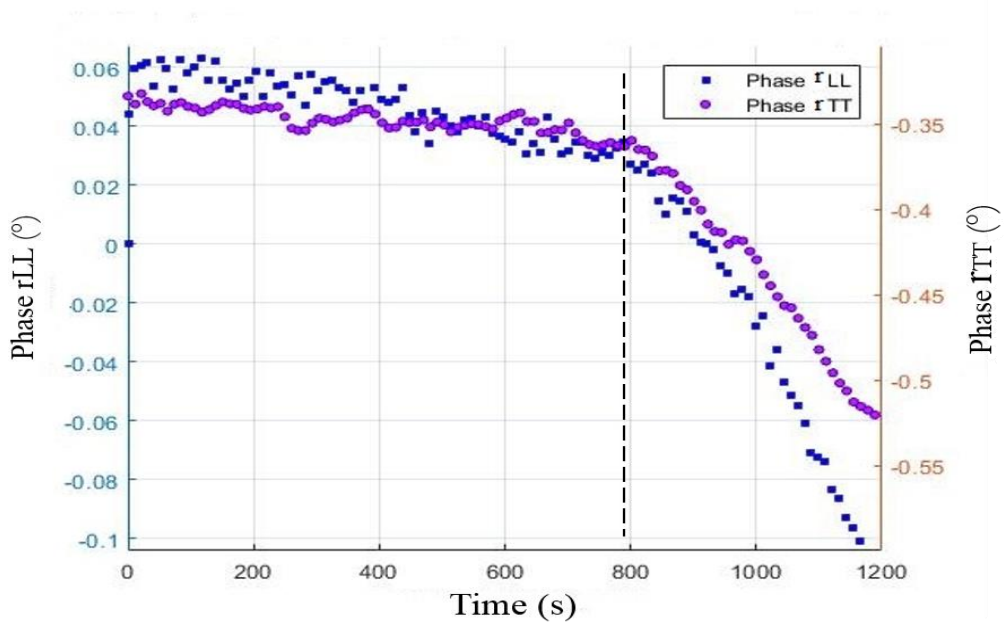


Figure II.29. Phase angle variation for the longitudinal and shear incident waves of 4 % Cv Au-water nanofluid droplet on a silicon substrate at room temperature.

In **Fig. II.29**, we represent the phase angle variation for both shear and longitudinal reflection coefficient of same gold droplet during evaporation process. These evolutions are more representative and sensitive than the modulus of the reflection coefficient. So, after 800 s, the phase angle rapidly decrease as a function of time. This sensitivity will entails higher variation in the viscosity after from t=800 s till the end of the evaporation process. From the variation of the shear phase angle in **Fig. II.29** and according to **Eqs. (9), (10) and (11)** we can obtain the variation in shear viscosity Au-water droplet during evaporation process. (See **Fig. II.30**)

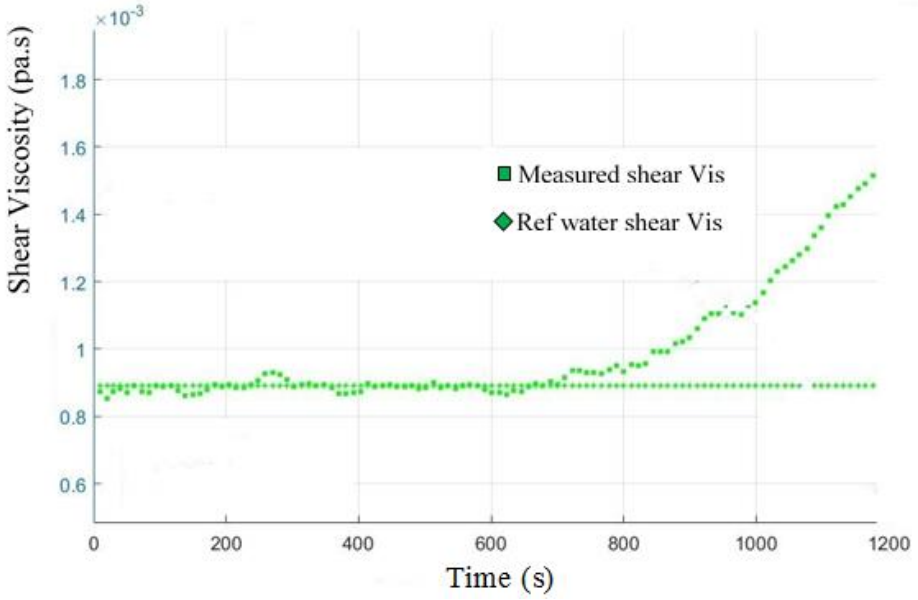


Figure II.30. Shear viscosity variation during the evaporation of 4% C_v Au-water nanofluid droplet on a silicon substrate at room temperature.

Fig. II.30 presents the variation of shear viscosity of 4% C_v Au-water nanofluid sessile droplet during its evaporation. At the beginning of the process we can see a constant variation in the shear values equal to 8.9×10^{-4} pa.s which it's the same value to the water at room temperature [113, 114] and this means and double check the accuracy about the stability of the gold nanoparticles inside the drop, also the no precipitation at the interface.

After 800 s from the time of the evaporation process an increase in the shear viscosity started to appear. The increasing in the viscosity due to the gold nanoparticles deposition on the interfaces.

II.3.2.3 Viscosity measurements as function of gold nanoparticles concentrations

Knowing the concentrations of the gold nanoparticles at each level during the evaporation process is needed. The percentage of the deposited particles on the interfaces can be extracted from the measurement of the modulus of the reflection coefficient, r_{LL}, as follows:

$$|r_{LL}|=\left|\frac{Z_s-Z_{nf}}{Z_s+Z_{nf}}\right|=\left|\frac{Z_s-\rho_{nf}C_{nf}^{L}}{Z_s+\rho_{nf}C_{nf}^{L}}\right|=\left|\frac{Z_s-\sqrt{\rho_{nf}E_{nf}}}{Z_s+\sqrt{\rho_{nf}E_{nf}}}\right|$$
$$;$$
$$\rho_{nf}=(1-\nu_p)\rho_w+\nu_p\rho_p,\quad E_{nf}=(1-\nu_p)E_w+\nu_pE_p \qquad (12)$$
$$;$$
$$\Rightarrow |r_{LL}|=\left|\frac{Z_s-\sqrt{\left((1-\nu_p)\rho_w+\nu_p\rho_p\right)\left((1-\nu_p)E_w+\nu_pE_p\right)}}{Z_s+\sqrt{\left((1-\nu_p)\rho_w+\nu_p\rho_p\right)\left((1-\nu_p)E_w+\nu_pE_p\right)}}\right|$$

Where ρ_{nf} and E_{nf} are the density and the Young modulus of the nanofluid respectively, ρ_p and E_p are the density and the Young modulus of the gold nanoparticles, ν_p is the volume fraction of the particles.

From **Eq. (12)** we can extract the percentage of the particles from the reflection coefficient variation during the evaporation process and this percentage represents the volume of the particles deposited at the interface. From **Fig. II.29** and according to **Eq. (11)** we can extract the dynamic viscosity as a function of volume fraction concentration of gold nano-particles deposit above the transducer, **Fig. II.31**.The values of the volume concentration are given also in **Table II.6** four each reflection coefficient values during Au-water 4 % C_v droplet evaporation.

t (s)	0	200	400	800	1000	1100	1200
10^{-3} x r_{LL}	858.87	858.87	858.87	858.85	858.8	858.5	858.2
Ø %	0	0	0	0.012	0.014	0.02	0.03

Table II.6. Percentage of deposited particles above the transducer as a function of time.

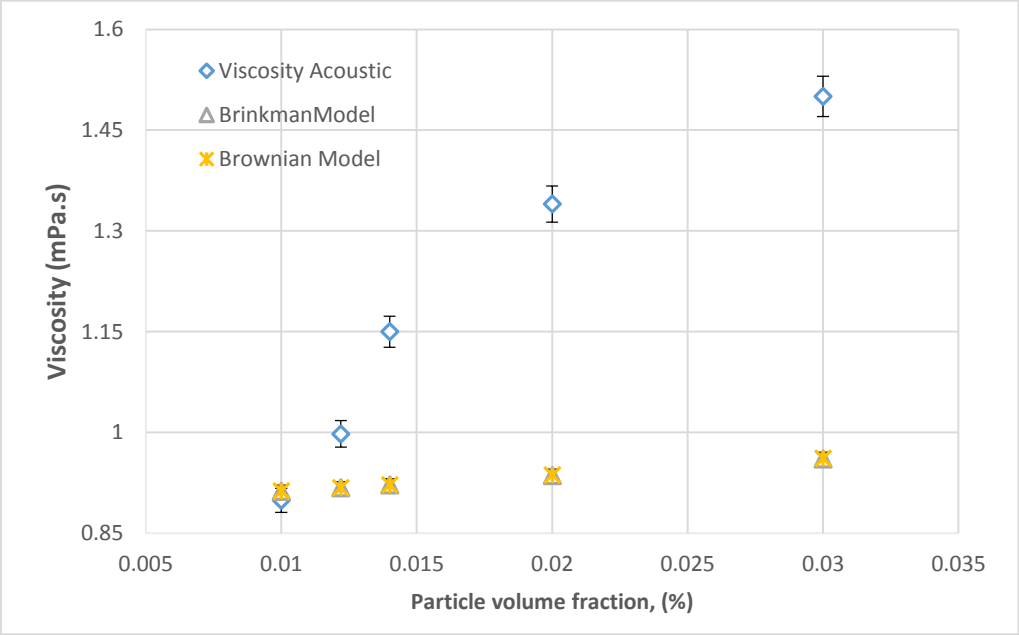


Figure II.31. Comparison of experimental viscosity of Au-water nanofluid (by acoustic method) to Brinkman and Brownian models at room temperature (±2%).

The theoretical models presented by Brinkman and Brownian gave a good representation of the results at low percentages. But as the concentration increases, these simple models are still not suitable for predicting the viscosity of nanofluids.

II. 4 Conclusion

In order to select the best nanofluids, the thermo and physical properties of nanofluids were analyzed. In this Chapter, a clear analysis of the properties of nanofluids was therefore carried out. First, the stability of copper oxide nanofluids was tested using an acoustic method to verify their stability inside a sessile droplet during evaporation. This method has been validated by an optical coupled to an infrared thermography method. The results showed that copper oxide nanoparticles are not stable inside the fluid and this affects the thermal performance of nanofluids during fluid circulation. For this reason, another type of nanofluids, gold nanoparticles, was used and studied to analyze their stability, the results showed its good stability during the evaporation process.

In addition, an experimental study, based on a high frequency reflectometry principle, provide a detailed analysis to measure one of the most important physical properties of nanofluids, which is the viscosity. This method depends on the shear waves which generated by the transducer to extract the dynamic viscosity. It was possible after the development of the transducer, using the blind technique, to increase the amplitude of the shear acoustic wave. Measuring the shear viscosity of a droplet of gold nanofluid during the evaporation process was done by measuring the mechanical impedance of the liquid, which has a complex form due to the attenuation of the sound energy produced by a nanofluids (viscoelastic losses). From shear reflected wave, an online measurement of the shear viscosity was obtained throughout all the evaporation process at the solid/liquid interface. In a conclusion, Acoustic method is giving simultaneous access to complex longitudinal and transverse reflection coefficient. We have presented the importance of the development of transducers (blind technique) to generate these two components compared with optical method.

Finally, these two method are suitable for selecting the good types of nanofluids in our application later on. So, Chapter 3 will presents the thermal performance of the selected gold nanofluids, for different nanoparticle sizes and synthesis (Citrate coating and non-coating), during droplet evaporation at different surface temperatures.

Chapter .III Experimental studies on evaporation kinetics of gold nanofluids droplets

III.1 INTRODUCTION 70
III.2 METHODOLOGY AND EXPERIMENTAL SETUP 71
III.2.1 Infrared and optical measurements 72
III.2.2 Acoustic measurements 73
III.3 EXPERIMENTAL RESULTS 74
III.3.1 Infrared and optical investigations 74
III.3.1.1 Au nanofluid (1% C_v; 0.1mM PBS, reactant free)-Water mixture, Particle size effects ..74
III.3.1.2 Au nanofluid (1% C_v; Citrate Capped-PBS)-Water mixture, Citrate effects 79
III.3.2 Acoustic investigations: Gold nanoparticles stability during droplet evaporation at ambient temperature 82
III.4 CONCLUSION 86

This Chapter is based on an article under review in the Journal of Applied Thermal Engineering (2020). The author of this thesis contributed to the Infrared and optical methods part by designing and performing experiments, analyzing experimental results and writing the section of the manuscript concerning visual investigation. Dr. J. Carlier, Dr. M. Toubal and Pro. B. Nongaillard took charge of acoustic method part experiment design and execution, experimental results analysis and manuscript writing. Prof. S. Harmand supported the author of this thesis for the writing of the manuscript and gave approval to the final version.

III.1 Introduction

In this Chapter, a series of experiments investigate the evaporation of gold nanofluid sessile droplets on a perfluorodecyltrichlorosilane (PFTS) silicon substrate heated to 77 °C. The evaporation processes of different nanofluid droplets of the same initial volume, all for a 1% C_v volume concentration prepared from the 0.1mM original suspension, are visualized to examine the size effect of different sizes of gold nanoparticles (2.2, 5 and 10 nm) and the impact of surface coating (with and without Citrate capping in phosphate buffered saline solvent) on enhancing heat transfer. This study open access to understand the size effect of gold nanoparticle in very small scale and the different types of surfactant on heat and mass transfer during the evaporation of droplet. Two methods are used to analyze the evaporation process, an optical one coupled to an infrared thermography method and an acoustic method. These complementary methods have the ability to investigate clearly the solid/liquid and liquid/vapor interfaces at the same time. From the optical observation, using a Drop Shape Analyzer (Kruss system), the evolution in time of the shape of the droplets (contact angle, base diameter and volume) are measured under controlled conditions (Humidity=50%, T_{atm}=23°C). Then, the evaporation rate is deduced from the measurements of the evolution of volume in time. At the same time, an infrared camera is used to observe the droplet surface gradient temperature, air/liquid interface, due to thermal Marangoni flow. The acoustic method, based on a high frequency echography principle, allowed to monitor the stability of nanoparticles inside the droplets (Au-water mixture) during the process of evaporation.

III.2 Methodology and experimental setup

In this work, the studied nanofluid consists of gold (Au) nanoparticles (Sigma Aldrich, Molecular weight = 196.97 g/mol with a volume concentration of 1% C_v) dissolved in distilled water (as a base fluid) and stabilized through ultrasonication (Elma, S 10/H) for at least 30 min before use. Three sizes of gold nanoparticles particle were used at 2.2, 5, and 10 nm for the citrate-capped PBS solution while 5 and 10 nm for the 0.1mM PBS, reactant free, **Table. III.1**. PBS reactant free solution is used to stabilize the nanoparticle and to prevent any change in the PH of the gold nanofluid solution presented in volume concentration (See **Fig. III.1**).



Figure III.1. Gold nanofluids of different sizes (2, 5 and 10 nm) and coating solutions (PBS and Citrate).

Nanoparticle, 1% C_v	Size (nm)	Buffer solutions	
Gold, Au	2.2	citrate-capped-PBS solution	-
Gold, Au	5	citrate-capped-PBS solution	0.1mM PBS, reactant free
Gold, Au	10	citrate-capped-PBS solution	0.1mM PBS, reactant free

Table III.1. Properties of prepared gold nanofluids.

To analyze the droplet evaporation process, two different methods are used, one using optical and infrared thermography measurements and the other one using acoustic reflection coefficient measurements at room temperature.

Nanofluids droplets are deposited, in both methods, on a silicon substrates modified with a perfluorodecyltrichlorosilane (PFTS) layer to achieve hydrophobic surfaces [115]. So, in that case, both methods have the same substrate characteristics. The optical measurements were achieved by increasing the substrate temperature from ambient to 77 °C. The calibration for the silicon substrate emissivity calibration was done using the emissivity calculator by the infrared camera. The technique is to measure the surface temperature of a known emissivity material such as a black object attached to the silicon substrate. From the known real temperature of the black object we can find the emissivity of the silicon substrate. This technique is suitable to find out the wanted substrate surface temperature. Finally, the water droplet analysis will be extracted with its known emissivity (≈0.97).

III.2.1 Infrared and optical measurements

This experimental setup allows us to calculate the evaporation rate of nanofluids droplets for each particle sizes and to visualize the convection cells caused due to Marangoni effect at high temperatures.

The substrate is heated using a joule effect by a resistance wire connected to the voltage supplier to control the temperature, **Fig III.2**. The substrate is placed above a semiconductor material to homogenize the heating medium. Calibration was performed after adjusting the voltage setting for each surface temperature. The evaporation process of droplets is observed and recorded using a high speed camera from the side view (CCD camera, Allied Vision Technologies, 780 x 580 pixels) which is connected to a backlight lighting. Then a Kruss Drop Shape analyzer is used to measure the droplets profile (Contact Angle, Volume, Base diameter, etc...). At the same time, an infrared camera (FLIR, X6580SC, 640 x512 Pixels, 15 um detector pitch) is installed on the top for the infrared thermal mapping and visualization of thermal instabilities on the surface of the droplets through a sapphire window. The evaporation process was carried out under the same conditions (Initial volume droplet V_i =1.5 µL, Substrate surface temperature: Amb to 77 °C) inside a controlled chamber (H=50%, T_{atm}=23°C).

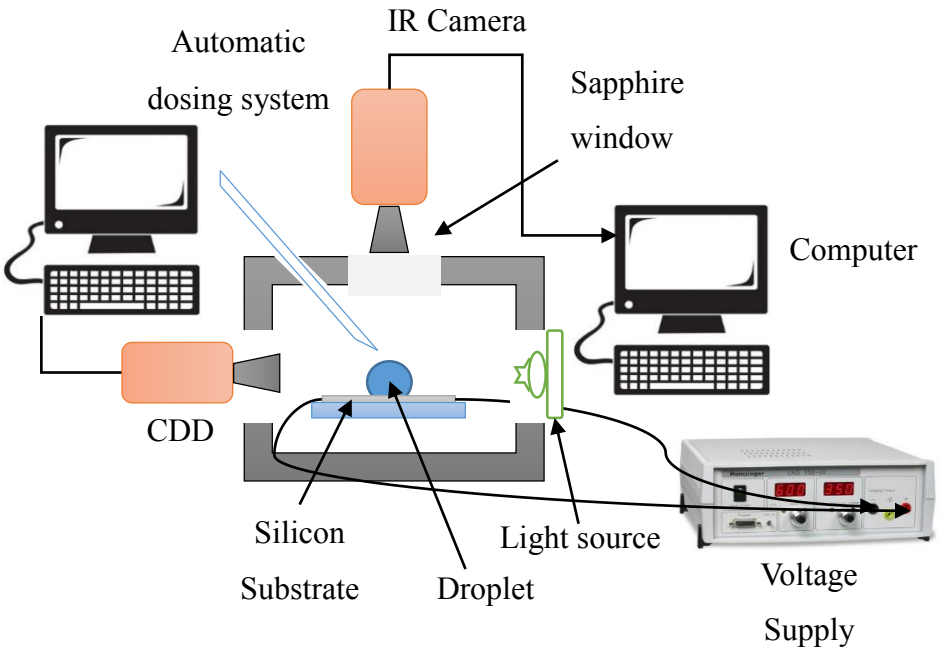


Figure III.2. Schema of the experimental setup.

III.2.2 Acoustic measurements

Measurements are carried out using the same configuration (**Fig. III.3)** and the same procedure as those used in Chapter 2. This method allows highly sensitive analysis of what occurs at the liquid-solid interface. [116]

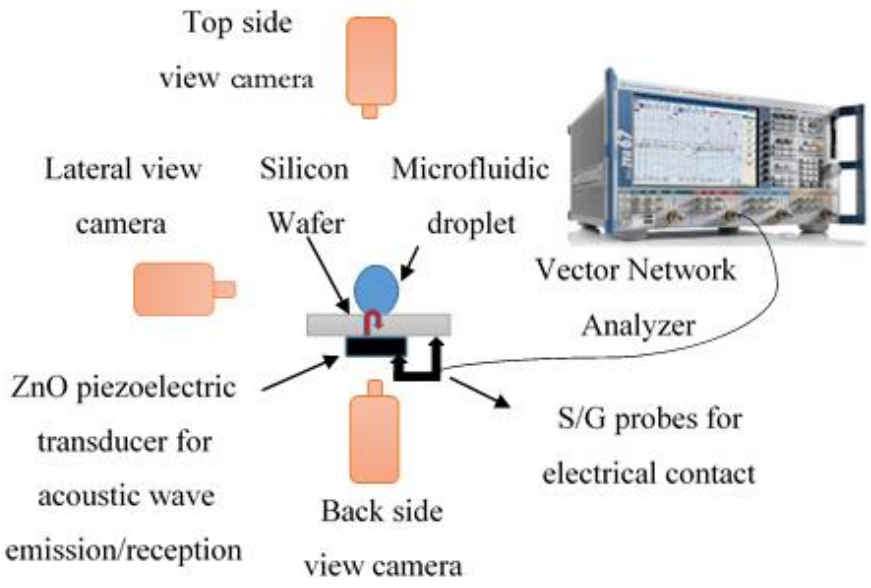


Figure III.3. Schema of the experimental setup of acoustic measurements.

III.3 Experimental results

III.3.1 Infrared and optical investigations

The optical and infrared techniques are applied to investigate the dynamic evaporation of droplets of gold nanofluid. The CCD camera records the evaporation process and then the software Kruss Drop Shape Analyzer analyzes the profile of droplets and the evolution of droplets, contact angle, volume and diameter, are accessible. Moreover, the infrared camera records the evaporation process at the top view and provides the gradient temperature distribution on the surface of the droplets.

III.3.1.1 Au nanofluid (1% C_v; 0.1mM PBS, reactant free)-Water mixture, Particle size effects

For the water-Au mixture of different particle sizes (5, 10 nm), the result was compared to that of pure water on the $V^{2/3}$ plot. **Fig. III.4** shows the evolution of $V^{2/3}$ for droplets of pure water and 1% C_v Au-water mixture of different particle sizes at different surface temperatures.

While the measured contact angle with the silicon substrate showed the same starting value for all the mixtures, **Fig. III.5**.

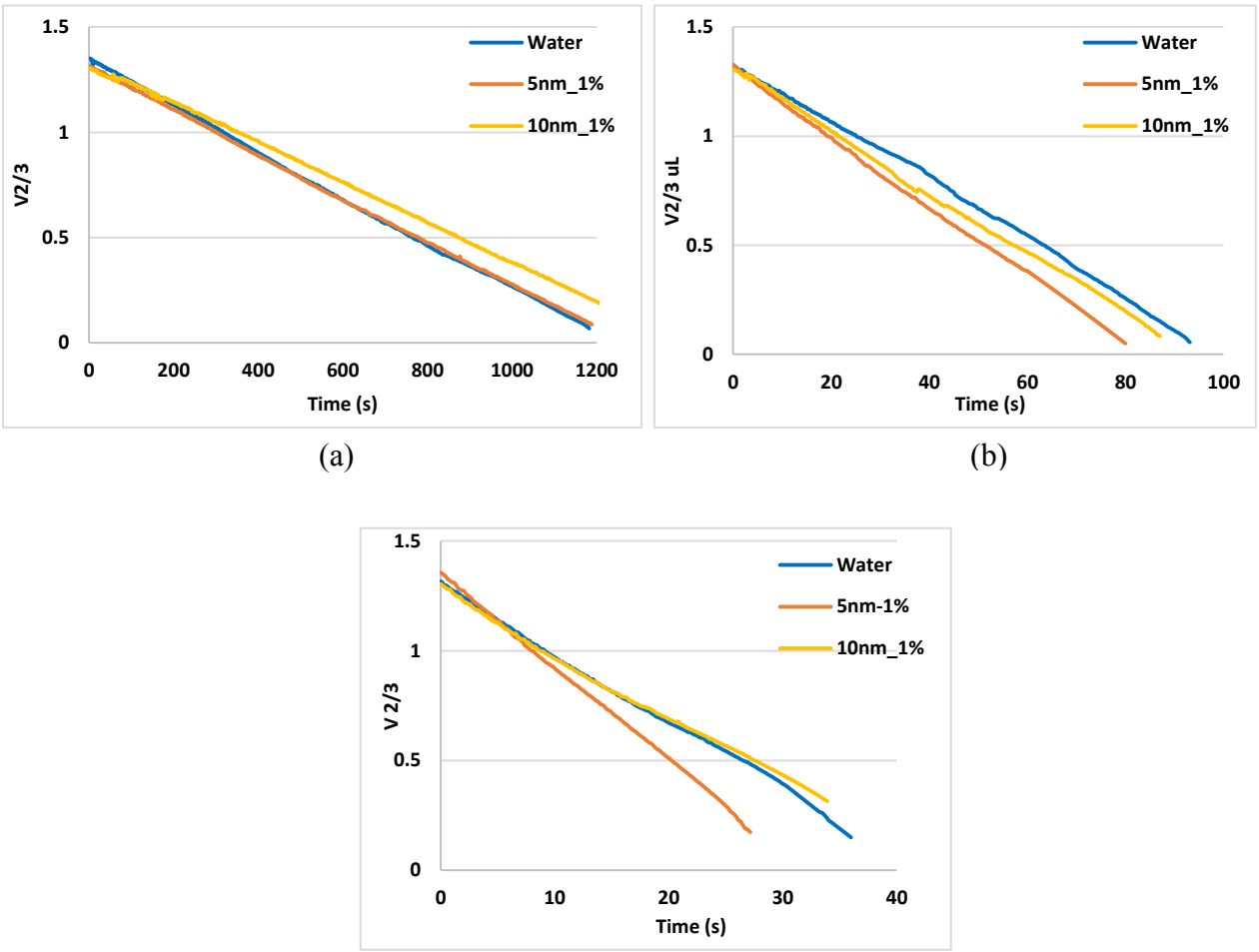


Figure III.4. Evolutions of the volume for water and gold nanofluid, with different particle sizes under substrate temperatures (a) at ambient, (b) 55 °C and (c) 77 °C (Annex A), versus time.

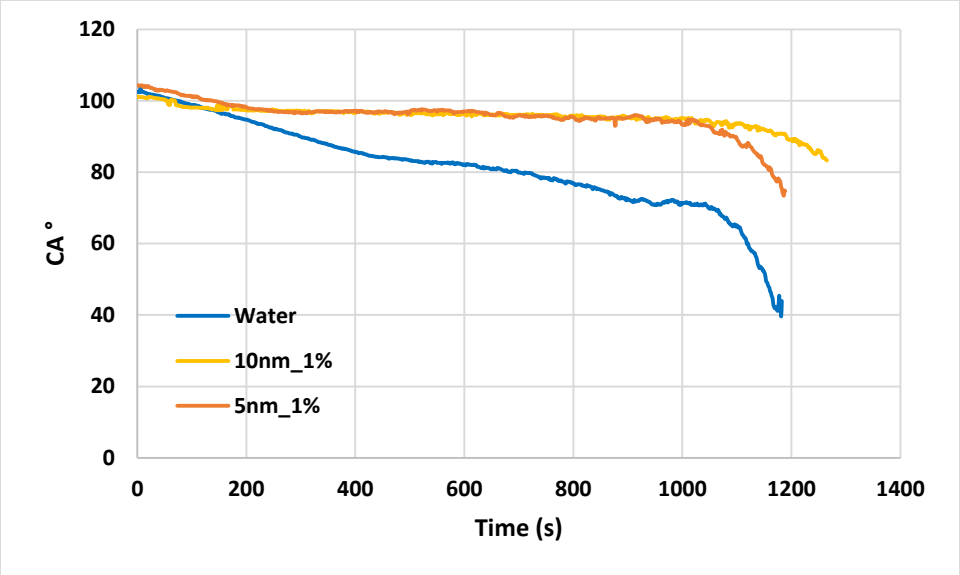


Figure III.5. Normalized contact angle for water and gold nanofluids during evaporation, with different sizes (5 and 10 nm), at ambient temperature.

The results showed that at ambient temperature, the evaporation of pure water droplets was faster than the gold nanofluids of the two different sizes. Since reducing the contact angle increase the contact area between the droplet and solid surface and also reduces droplet thickness [117]. As the liquid layer becomes thinner, heat transfer from the solid to the liquid-vapor interface is enhanced. Both effects increases the droplet evaporation rate.

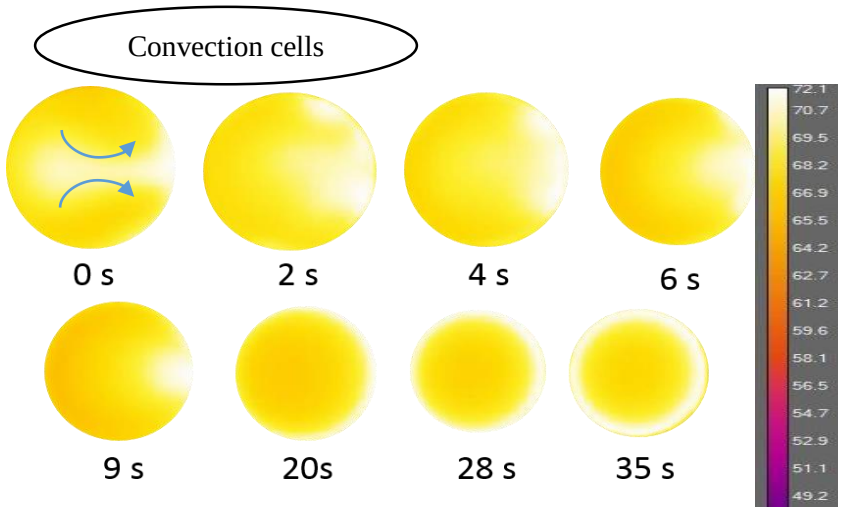
The measured contact angle of pure water showed a decrease in its values more than that of droplet gold nanofluid and this validates the enhancement in its droplet evaporation.

When the surface temperature increased to 55 °C, the evaporation process showed a higher evaporation rate of the 5 nm Gold-water mixture with 17% while 3% for the 10 nm Gold-water mixture.

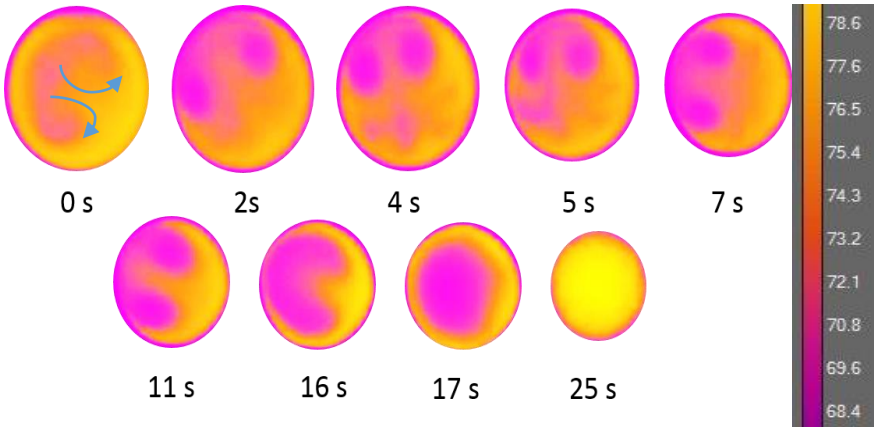
Similarly, at a surface temperature of 77 °C, the evaporation process showed a higher evaporation rate of the 5 nm Gold-water mixture with 35% whereas 2% for the 10 nm Gold-water mixture. Thus, the evaporation rate is found to depend on the size of the nanoparticles, which showed that the smallest particles size (5nm) has the greatest effect on increasing the evaporation proceeds during the droplet lifetime than the 10 nm.

This difference can be linked to different reasons, the effective surface area of 5 nm Au-water mixture is greater than the 10 nm Au-water by a factor 2 and this means a greater amount of water molecules can come into contact with a larger surface surrounding the 5nm nanoparticles, thus affecting reactivity). Furthermore, Infrared Camera images made it possible to detect the convection cells, **Fig. III.6,** due to the Marangoni effect that appeared on the surface of droplets. These convection cells have the ability to increase the vapor mass transfer at the liquid-air interfaces and to induce a faster evaporation rate [118]. The convection cells created by the thermal Marangoni can be observed on the surface of the droplets when the substrate is heated to high temperatures. The convection cells of the gold nanofluids appeared and remained longer than those of pure water and this is due to the Brownian motion of nanoparticles inside the droplet. The absorption by solid particles of gold and their flow has the ability to stay longer and to accelerate the convection liquid/vapor coefficient. These convection cells improve the evaporation process by inducing the thermal Marangoni number. For this reason, **Table. III.2** represent the life time of these cells during the evaporation process of the pure and gold-water mixture (5 and 10 nm) at 77 °C surface temperature.

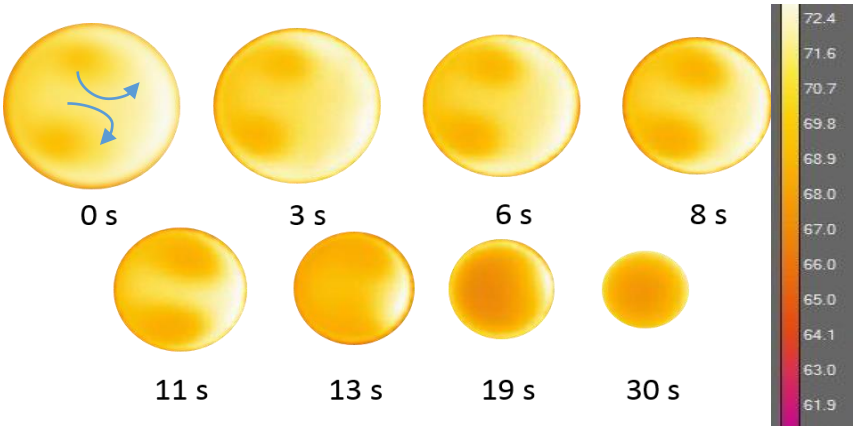
The table has shown that the higher evaporation rate has a higher convection cells life and these results validate the increase in the evaporation rate of the 5nm Gold-water droplet.



(a)



(b)



(c)

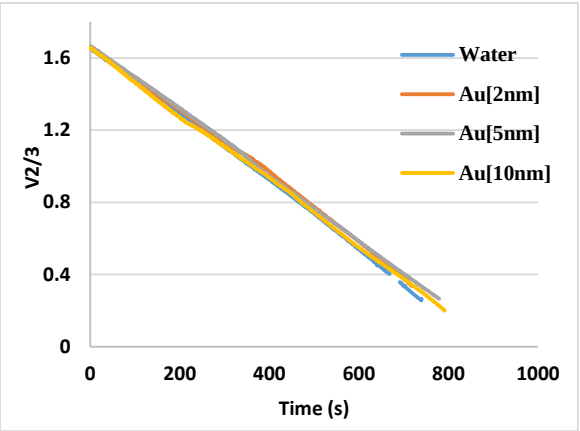
Figure III.6. Snapshots from an infrared video of the evaporation process of (a) pure water (b) 5 nm Au-water and (c) 10 nm Au-water nanofluids at 50 % relative humidity and 77 °C surface temperature, 1%C_v.

Fluids/medium	**Convection cells lifetime (%)**
Water	5 %
5 nm Au-water,1% C_v	68 %
10 nm Au-water, 1% C_v	43 %

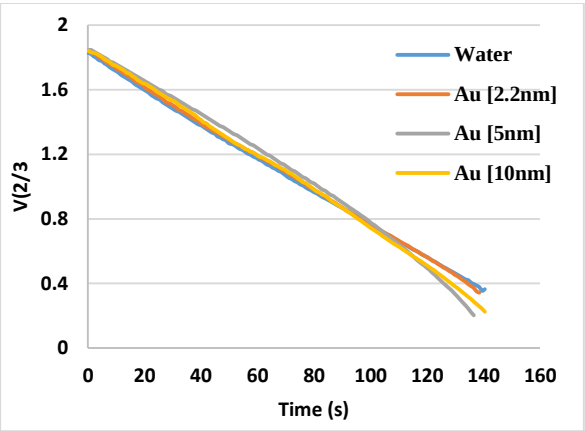
Table III.2. Lifetime of the convection cells at 77 °C substrate temperature of pure water, 5 nm Au-water and 10 nm Au-water nanofluids.

III.3.1.2 Au nanofluid (1% C_v; Citrate Capped-PBS)-Water mixture, Citrate effects

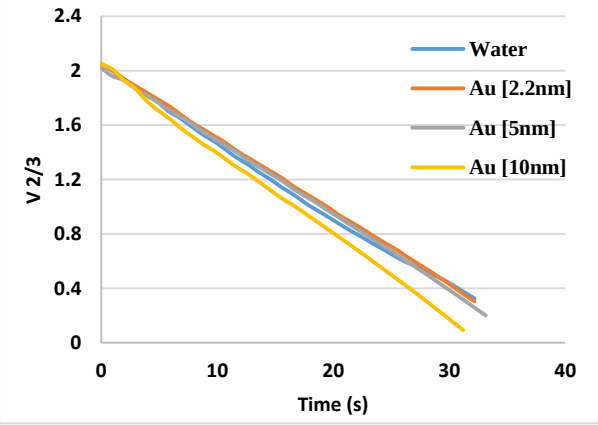
The same measurements were made for the water-Au mixture of the same particle sizes (2.2, 5, 10 nm- Citrate-Capped- PBS solution) but with synthesis of the surface of gold nanoparticles with citrate in order to study the effect of citrate capping on enhancing the evaporation process. The result was compared to that of pure water on the $V^{2/3}$ plot. **Fig. III.7** shows the evolution of $V^{2/3}$ for droplets of pure water and 1% C_v Au-water mixture of different particle sizes at different surface temperatures.



(a)



(b)



(c)

Figure III.7. Evolutions of the volume for water and gold nanofluid (Citrate capping-PBS), with different particle sizes (2.2, 5 and 10 nm) under substrate temperatures (a) at ambient, (b) 55 °C and (c) 77 °C (Annex A), versus time.

The results showed that at ambient temperature, the evaporation of pure water droplet was a little faster than the gold nanofluids of the three different sizes, with 2% more. When the surface temperature increased to 33 °C, the evaporation process showed a higher evaporation rate of the 10nm Gold-water mixture with 11% while 5% and 4% for the 2.2 and 5nm Gold-water mixtures respectively.

Similarly, at a surface temperature of 55 °C, the evaporation process showed a higher evaporation rate of the 10nm Gold-water mixture with 10% whereas 8% and 2% for the 2.2 and 5nm Gold-water mixtures respectively. Finally, the 10nm Gold-water mixture showed the highest evaporation rate at the surface temperature of 77 °C with 15% more while 1% and 2% for the 2.2 and 5nm Gold-water mixtures respectively.

Thus, the evaporation rate, **Fig. III.8**, was found to depend on the size of the nanoparticles, which showed that the largest particles size (10nm) has the greatest effect on increasing the evaporation proceeds during the droplet lifetime.

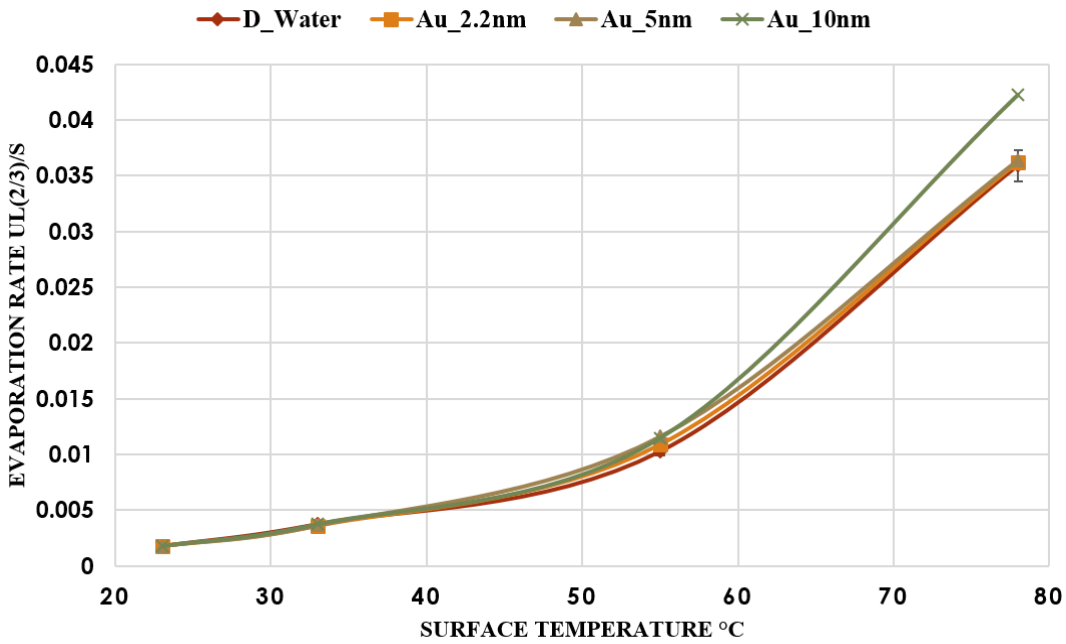
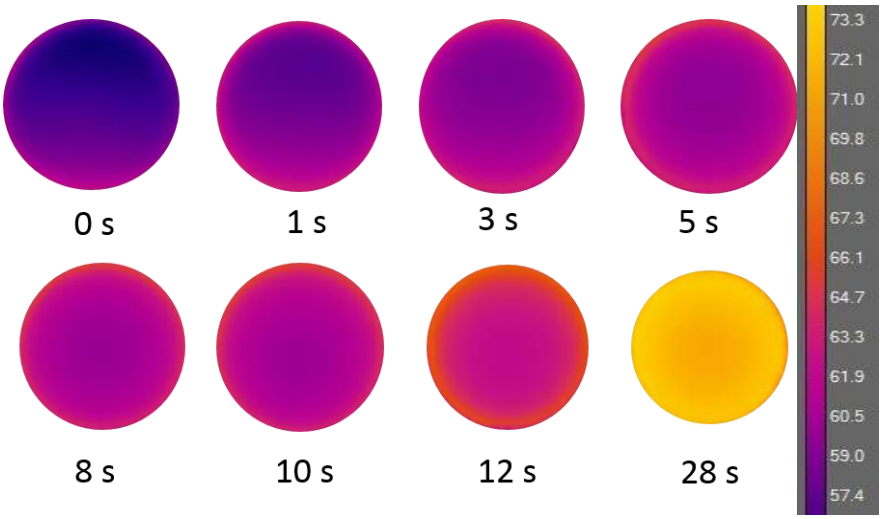
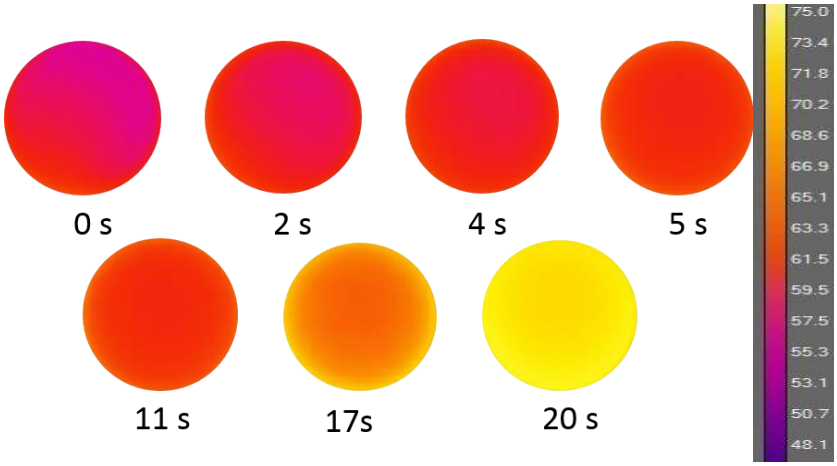


Figure III.8. Evaporation rate of the citrated gold nanoparticle sizes at different surface temperatures.

The Infrared Camera images made it possible to detect the convection cells, **Fig. III.9,** due to the Marangoni effect that appeared on the surface of droplets. These convection cells have the ability to increase the vapor mass transfer at the liquid-air interfaces and to induce a faster evaporation rate [118]. But with citrate capping, no observation of Marangoni cells detected by the infrared camera. It showed a homogenization of the temperature profile. For this reason, the life time of these cells during the evaporation process was negligible.



(a)



(b)

Figure III.9. Snapshots from an infrared video of the evaporation process of (a) Citrated capping 5 nm Au-water and (b) Citrated capping 10 nm Au-water nanofluids at 50 % relative humidity and *77* °C surface temperature, 1%$C_{v.}$

III.3.2 Acoustic investigations: Gold nanoparticles stability during droplet evaporation at ambient temperature

Several precautions are taken to improve the accuracy of the measurements. The acoustic device is calibrated using water as a reference liquid, at ambient temperature. A drop of pure water is deposited on the hydrophobic silicon surface where the transducer (250 μm in diameter) is located. An acoustic wave (Longitudinal) is generated by the ZnO transducer through the substrate to the interface. The reflection coefficient of water is represented in **Fig. III.10** during the evaporation process, demonstrates a good reliability of the measured amplitude of the coefficient $|R| = 0.8594 \pm 0.01\%$.

This method makes it possible to follow the kinetics of the nanoparticles deposition. Drops of the same initial volume (1.5μL) are deposited, at ambient temperature, on the silicon substrate under controlled conditions (H=50%, T_{atm}=23°C). Various sizes of the gold nanoparticles (2.2, 5 and 10 nm) with and without citrate capping are then compared in order to analyze the stability of the nanoparticles during the evaporation process.

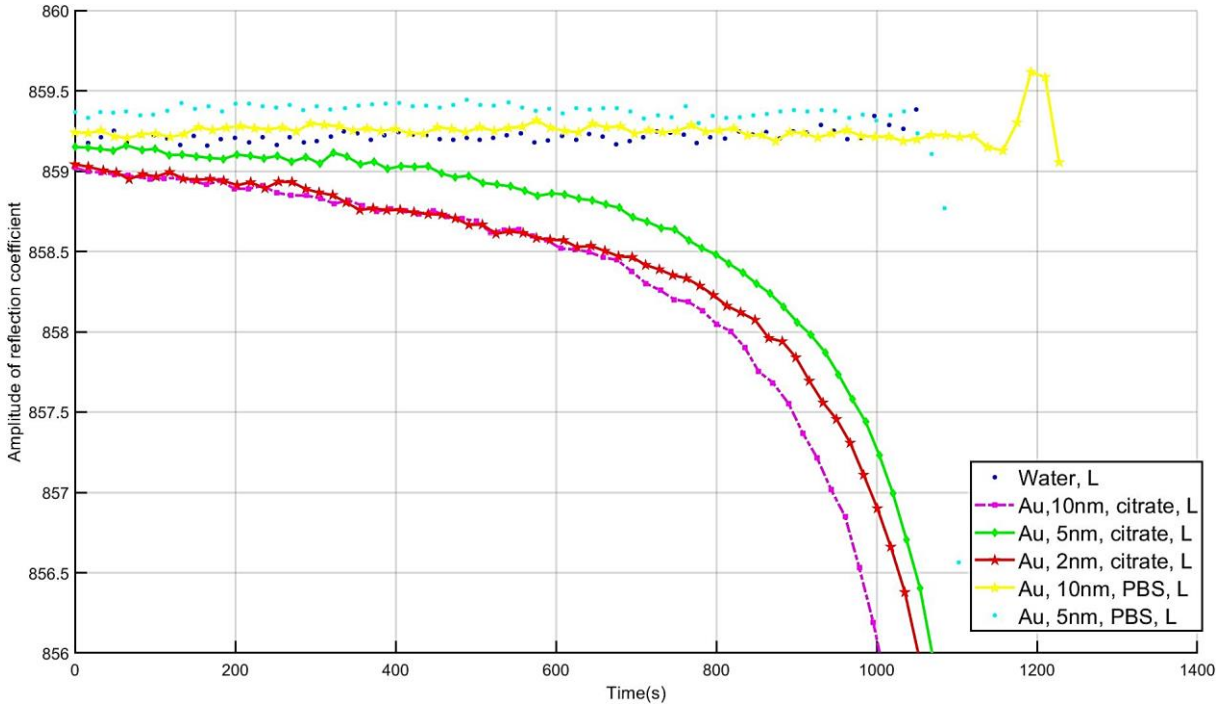


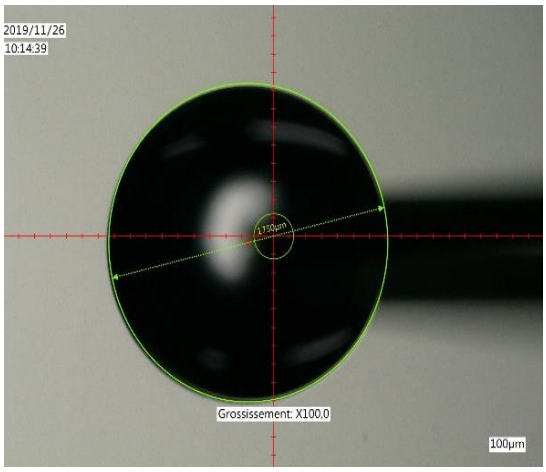
Figure III.10. Reflection coefficient evolution of pure droplet (black), Au-PBS and Au-Citrate-PBS during evaporation process at 23°C.

In **Fig. III.10**, the kinetics of the longitudinal reflection coefficient modulus for the different preparations, different sizes (2.2, 5 and 10 nm) and types of gold nanofluids (Citrate-capping PBS and PBS-reactant free), during the evaporation of a 4% C_v Gold-water mixture drop, are presented. One can notice a clear difference between the particles with and without citrate capping. Indeed, the reflection coefficient of the gold-water mixture drops with citrate capping (for all nanoparticle sizes) begins to decrease almost instantaneously until the end of the evaporation process. Whereas, for drops of gold-water mixture without citrate (for all sizes of nanoparticles) the reflection coefficient showed a constant value and began to decrease at the end of the process. As discussed in [111], the variation of the reflection coefficient ascribed to a change of the physical properties of the material interacting with the ultrasounds at the interface. So, the change in the reflection coefficient is due to the gold nanoparticles deposition on the silicon substrate above the transducer.

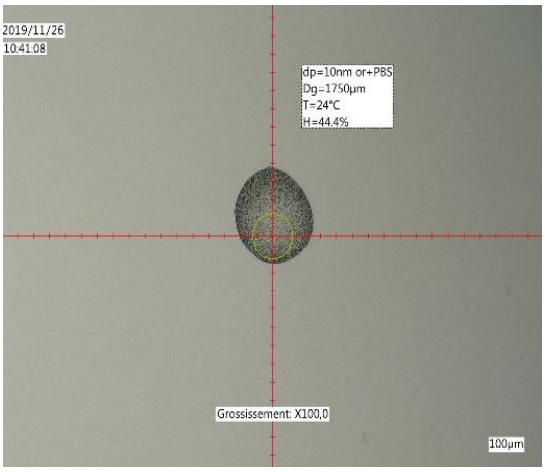
Moreover, in the previous study [111], we have also shown that the sedimentation of the nanoparticle is correlated to the life time of Marangoni cells. Here, the Marangoni cells observed by an infrared camera, (*section 3.1)*, showed no convection cells for the coated gold nanoparticles,

with citrate, during the evaporation process, this would therefore mean that the particles settle The acoustic method corroborates the link between dynamic deposition of nanoparticles and its effect on the life time of convection cells.

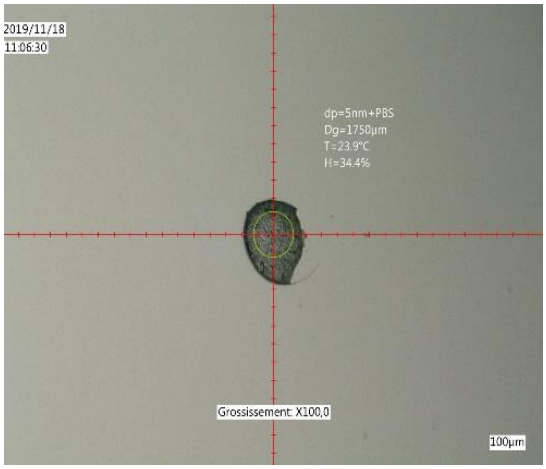
Fig. III.11, present the final shape pattern of the evaporated Au-water droplets with and without citrate capping for all sizes, 2.2, 5 and 10 nm at ambient temperature. The change in the shape of the dried gold nanoparticles between citrate coated and non-coated nanoparticles are clearly observed. For the non-coated gold nanoparticles (with PBS), a normal and uniform coverage pattern can be observed whereas a viscoelastic pattern is observed for the citrate nanoparticles.

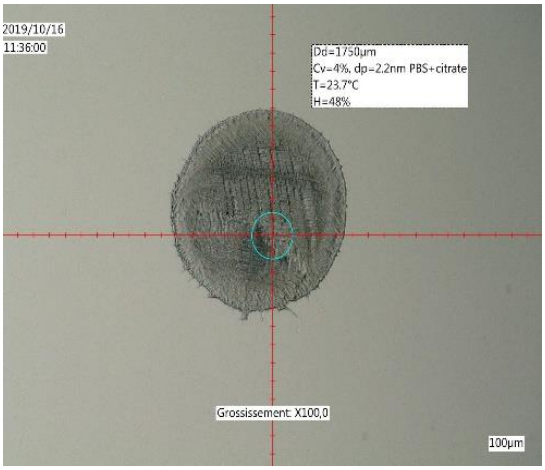


(a)

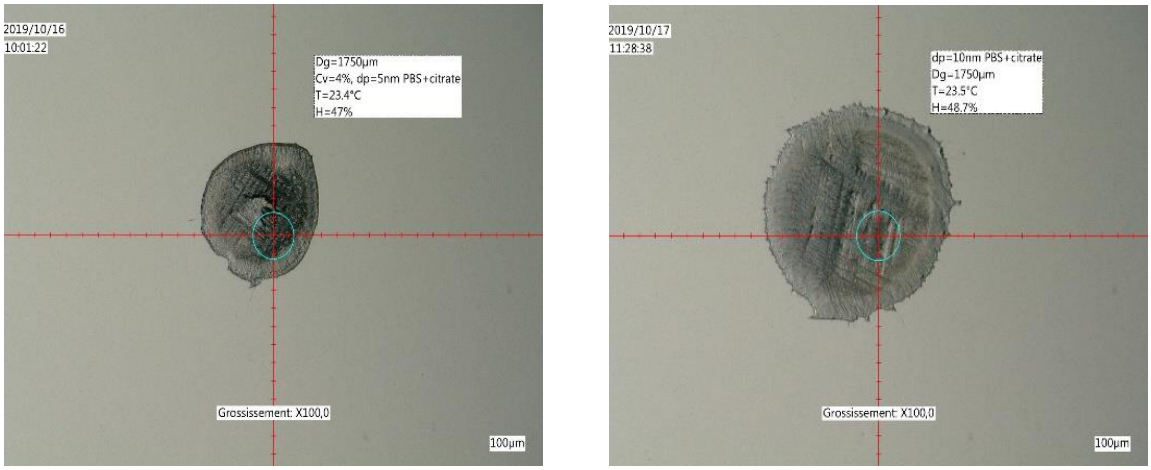


(b)





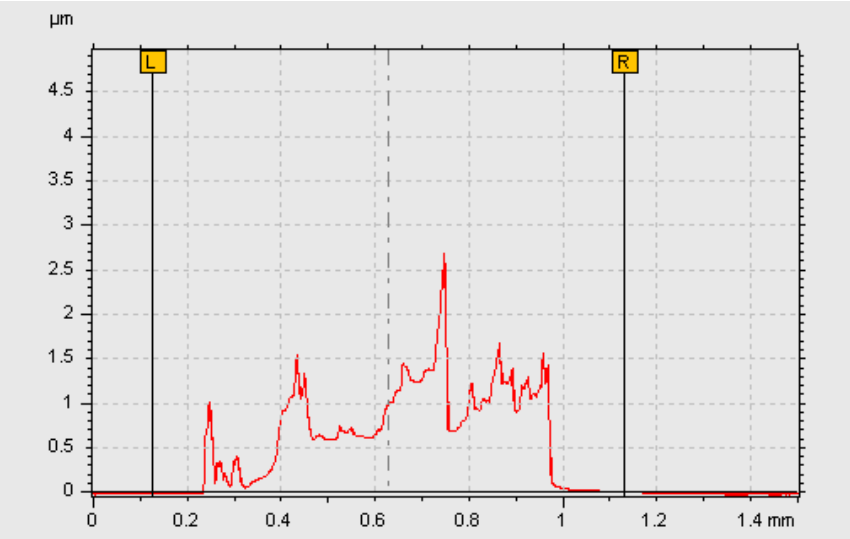
(c) (d)



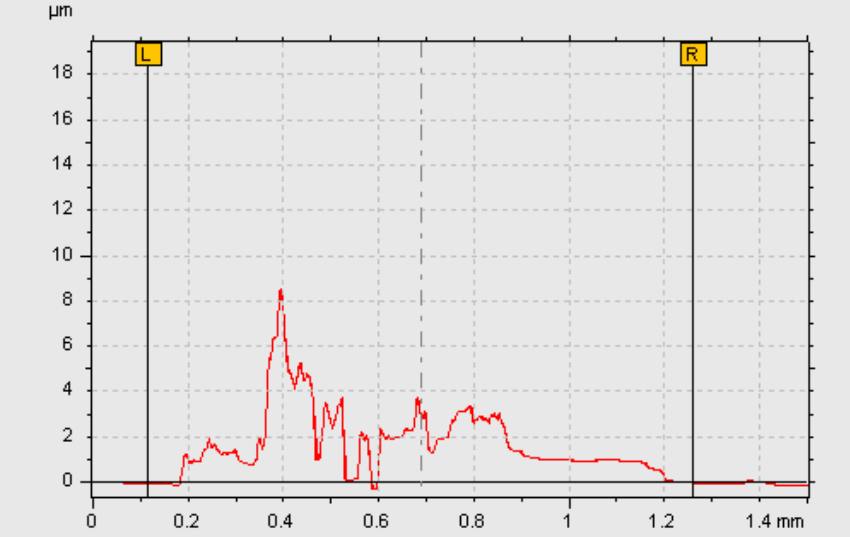
(e) (f)

Figure III.11. Gold Nanofluid Droplet deposited on silicon substrate and above the transducer (a) At starting point (b) Au-10nm- PBS (c) Au-5nm- PBS (d) Au-2.2nm-Citrate PBS (e) Au-5nm-Citrate PBS (f) Au-10nm-Citrate PBS (Nano particles Final shape pattern on the 250 µm transducer diameter).

In **Fig. III.12**, a profilometer is used to measure the thickness of the deposited nanoparticles on the silicon substrate. Fig. 10.a, a thickness profile distribution of 5nm gold nanoparticles with PBS gives a mean value of 1.3 µm while 4.5 µm height for 5nm gold nanoparticles coated with citrate and PBS. This variation due to high concentration of citrate in addition to PBS only.



(a)



(b)

Figure III.12. Thickness distribution of 5nm gold nanoparticles with 4% C_v, (a) PBS solvent (b) Citrate coating with PBS solvent.

These results are related to the infrared and optical. As explained previously, the evaporation rate of the gold nanoparticles with citrate-capping PBS was lower than that of gold nanoparticles with PBS-reactant free.

This can be explained, in addition to the thermal Marangoni effect, that the stability of the nanoparticles inside the droplet is an important factor. Since the nanoparticles begin to settle early during the evaporation process, this means that nanoparticles will lose their effectiveness by absorbing the heat flux and to transporting it to the liquid-air interface.

III.4 Conclusion

The evaporation rate of gold Au-water nanofluid sessile droplets of 1% C_v has been measured in a controlled room temperature air (H=50%, T_{atm}=23 °C) using a Drop Shape Analyzer. The size effect of gold nanoparticle (2.2, 5 and 10 nm) was studied as well as different buffer solvents (Citrate-Capping PBS and no citrate-PBS) on the evaporation characteristics of droplets. The analysis was performed using two different methods, these methods have the ability to give a very important information on the fundamentals of droplet evaporation.

An optical analysis, using Kruss system, was used to calculate the droplet evaporation rate of Au-water mixture at different surface temperatures. While, an acoustic method represented by coefficient reflection waves has shown the ability to understand the deposition phenomenon of nanofluid at the solid/liquid interface. The main conclusion of this work are:

- The gold nanofluids droplets, for both solutions, evaporate more rapidly as the surface temperature increases in comparison to the evaporation of distilled water droplets.
- The uncapped gold nanofluids with PBS solution showed that the smallest nanoparticle size (5 nm) has the greatest impact on the evaporation rate (+35% more) than the larger nanoparticle, 10nm.
- The citrate-capped gold nanofluid showed opposite results, the larger nanoparticle (10nm) has the greatest improvement on evaporation rate (+15%) but still less than the solution with PBS only.
- The origin of the different behavior for the gold nanofluid compared to the pure water comes mainly from the thermophysical properties represented by thermal conductivity.
- The thermal Marangoni plays an important role on enhancing droplet evaporation. It showed that the convection cells were observed clearly and stayed longer for the 5nm uncapped gold nanoparticle (68%) compared to the 10nm (43%) from total evaporation time.
- No convection cells were observed for the citrate-capped gold nanofluid due to nanoparticles deposition. This behavior was proved using the high-frequency waves to the interface.
- This stability showed an important factor on droplet evaporation process.

After having analyzed different types of gold nanofluids (different sizes and concentration), the gold nanofluids of 5 nm and 1% volume concentration with a PBS solution showed the best thermal performance of droplet evaporation than others. For this reason, gold nanofluid with same properties will be selected to apply it into a heat transfer system presented by two-phase heat transfer devise and a micro heat exchangers in order to investigate their thermal performance using, Chapter 4.

Chapter .IV Thermal performances of two-phase heat transfer and micro heat exchangers devices using self-rewetting nanofluids

IV.1 INTRODUCTION 89
IV.2 THERMAL PERFORMANCE OF TWO-PHASE HEAT TRANSFER DEVICES 90
IV.2.1 Experimental setup 90
IV.2.1.1 Working fluids: 90
IV.2.1.2 Procedure: 91
IV.2.1.3 Error analysis 92
IV.2.1.3 Porous media properties 93
IV.2.1.4 Thermal resistance: 93
IV.2.2 Experimental results and discussion 93
IV.2.2.1 Heat transfer characteristics 93
IV.2.2.2 Vapor pocket dynamics 95
IV.3 THERMAL PERFORMANCES OF A MICRO HEAT EXCHANGERS USING NANOFLUID AND SELF-REWETTING FLUID 99
IV.3.1 Experimental method 99
IV.3.1.1 Polydimethylsiloxane (PDMS) - based microchannel device, microfabrication and experimental facility. 99
IV.3.1.2 Microfabrication of Polydimethylsiloxane (PDMS) microchannel 100
IV.3.1.3 Surface emissivity measurements of ITO coated glass and PDMS for infrared thermography 101
IV.3.1.4 Working fluids used in the experiment 103
IV.3.2 Data reduction 105
IV.3.3 Results and discussion 107
IV.3.3.1 System calibration: Water as a reference 109
4.2 Gold nanofluid and Butanol self-rewetting liquid as a working fluids 110
IV.4 CONCLUSION 114

This Chapter is based on two articles to be submitted in a peer reviewed journals (2020). The author of this thesis contributed to the infrared method part by designing and performing experiments, analyzing experimental results and writing the section of the manuscript concerning visual investigation. Prof. S. Harmand, Dr. J. Carlier, Dr. M. Toubal and Pro. B. Nongaillard supported the author of this thesis for the writing of the manuscript and gave approval to the final version.

IV.1 Introduction

This Chapter presents an experimental analysis of the phenomenon of phase change inside a porous medium using different types of working fluids. It represents the impact of these fluids on improving the characteristics of heat and mass transfer in a Capillary Heat Pipe (CHP). In this study, gold nanoparticles (5 nm in diameter with 1% C_v), a self-rewetting binary solution (butanol with 3% C_v), and a mixture of self-rewetting butanol and gold nanofluid are considered to be the operating fluids within the CHP. The experiments are carried out after designing and developing the capillary heat pipe section. It consists of a water tank with a pump, an evaporator attached to a copper porous medium on which thermocouples and power supplies are placed. The experimental results showed the positive influence of gold nanoparticles on the thermal system's performance by reducing the thermal resistance by 13% compared to pure water as the base working fluid. In addition, a self-rewetting butanol solution showed improvement in the performance of the capillary evaporator by decreasing its casing temperature. While a mixture of self-rewetting butanol solution (3 % C_v) and gold nanofluid (1% C_v) exhibited the best performance of heat and mass transfer performance by reducing the thermal resistance of the system by approximately 22 %. To explain the mechanism for improving heat transfer, the phase change phenomenon was visualized by an infrared camera for the three working fluids. It is shown that as the applied power increases, the shape of the vapor pocket developed in the wick also increases, for pure water, until it reaches a stable form. Whereas, with respect to nanofluid and self-rewetting fluid, the shape of the vapor pockets was smaller than that of pure water allowing more efficient mass and heat transfer. The thermophysical properties of these fluids such as thermal conductivity, stability, surface tension,

Marangoni, wettability, and capillary forces were presented to ensure and validate the decrease in the vapor pocket as well as the enhancement of the CHP thermal system.

In the next section, we are presenting an experimental study of the use of different types of fluids to observe and investigates their effect on the thermal performance of heat exchanger systems. Gold nanofluids and a self-rewetting binary solution (butanol) were used in the experiment at specific volume concentrations (1% C_v and 3% C_v respectively). The small dimensions of the microchannel along with 0.15 $ml.min^{-1}$ flow rate and various heat fluxes provide very low Reynolds number (laminar flow) , reflecting practical parameters for a microfluidic cooling platform. The microchannel was fabricated by Polydimethylsiloxane PDMS sticked to ITO/glass thin substrate in order to observe clearly the flow behavior during the experiment. The heat analysis of these smart fluids has been investigated using an infrared camera focused on the ITO/glass section, because of its non-contact, three dimensional and high resolution capability for temperature profiling, to measure the wall temperature and, therefore, calculate the heat transfer coefficient. Thus, a high speed camera (CCD) was fixed to the PDMS section to present the fluid flow.

IV.2 Thermal performance of two-phase heat transfer devices

IV.2.1 Experimental setup

IV.2.1.1 Working fluids:

The studied fluids in the present work consist of: gold (Au) nanoparticles (Sigma Aldrich, Molecular weight = 196.97 g/mol with a volume concentration of 1% C_v), self-rewetting fluids (water/butanol) and a mixed of self-rewetting nanofluid dissolved in distilled water (as a base fluid) and all are stabilized through ultrasonication (Elma, S 10/H) for at least 30 min before use. The size of gold nanoparticles particle was 5nm for the 0.1mM PBS, reactant free, **Table. IV.1**.

Fluids	Size (nm)	Concentration, C*v*%	Buffer solutions
Au/water	5	1%	0.1mM PBS, reactant free
Butanol/water	-	3%	-
Au/Butanol/water	-	1%-3%	-

Table IV.1. Working fluids with concentrations used.

IV.2.1.2 Procedure:

The experiment setup is shown in **Fig. IV.1** and **Fig. IV.2**. It consists of a porous wick of a copper foam, which physical properties are given in **Table. IV.2**, and a grooves brass block in order to represent a flat evaporator section of a capillary two-phase loops. The experimental configuration also includes a transparent window of sapphire that enables the visualization of the phase change inside the porous wick with an infrared camera (FLIR, SC7210-7500/SC7300, 320 x256 Pixels, 30 µm detector pitch). The upper surface of the porous structure is heated by using a grooved brass block with cartridge heaters. The heat losses to the ambient environment can be neglected since the heating block is thermally insulated with multilayer insulation materials. The evaporator is connected to a constant-level reservoir to supply sub cooled fluid the wick under the same conditions.

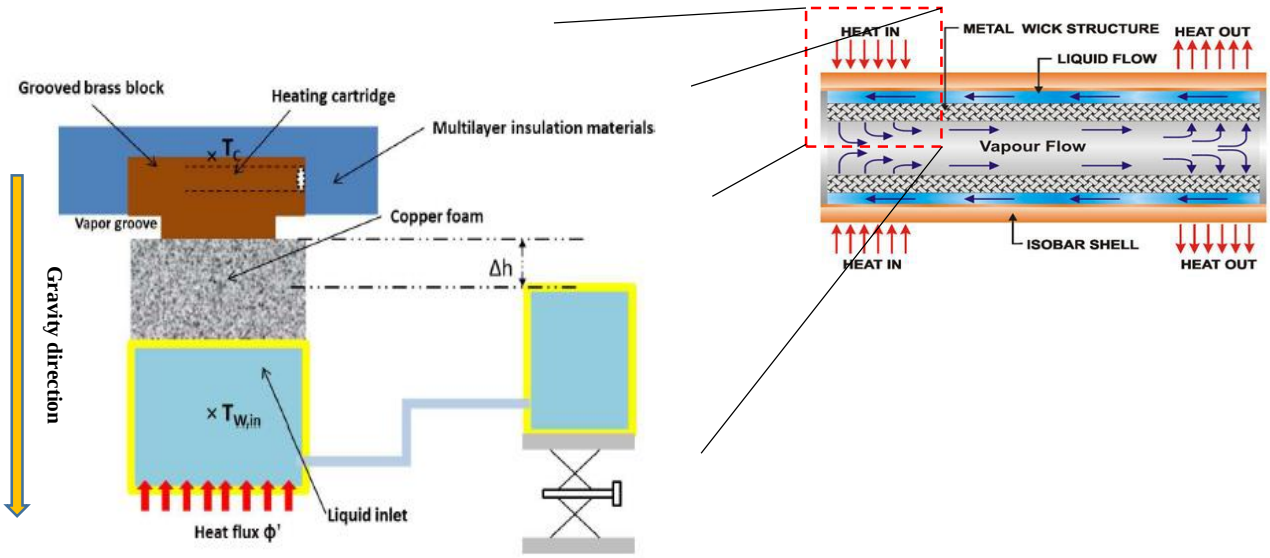


Figure IV.1. Experimental setup of the evaporation part.

The hydrostatic pressure drop is controlled by the elevation Δh, distance between the upper surface of the porous structure and water level in the reservoir. The liquid inside the reservoir is at ambient temperature and thus a heating film is used to heat the liquid before it enters the porous wick. Two K-type thermocouples are used to measure the casing temperature T_c and the temperature of the

fluid at the wick inlet $T_{w,\,in}$. The flow rate of the fluid at inlet was same and controlled by the pump during whole experiments.

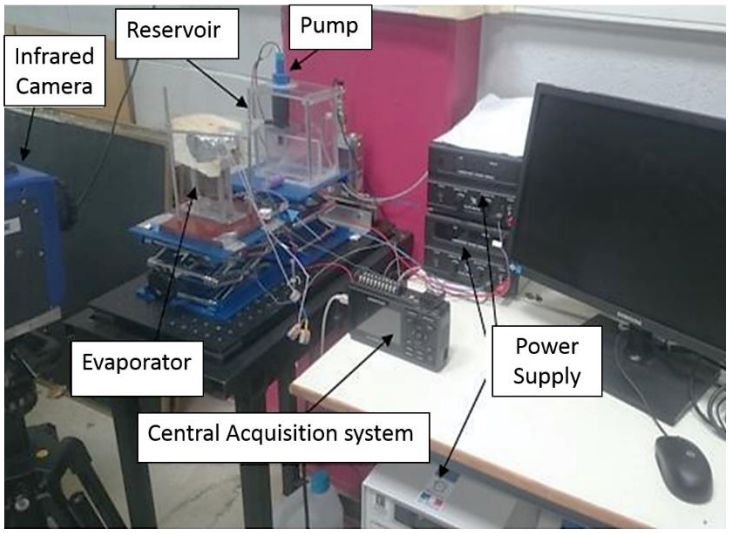


Figure IV.2. Experimental setup in real state.

IV.2.1.3 Error analysis

The temperature of the fluid at the wick inlet and the casing are measured by using K-type thermocouples. Measurement uncertainties are ±1 °C. With respect to the applied power, the relative uncertainty is estimated as 3.18% and it is determined by using following equation: [119]

$$\frac{\delta_{\emptyset}}{\varphi} = \sqrt{\left(\frac{\delta V}{V}\right)^2 + \left(\frac{\delta I}{I}\right)^2}$$

Where φ denotes the applied heat load, V is the voltage and I is the current.

IV.2.1.3 Porous media properties

The real sample of copper wick structure is shown in **Fig. IV.3**.The dimensions of the porous wick are 50 x 50 x 15 mm^2. The properties of the wick are listed in **Table. IV.2**.

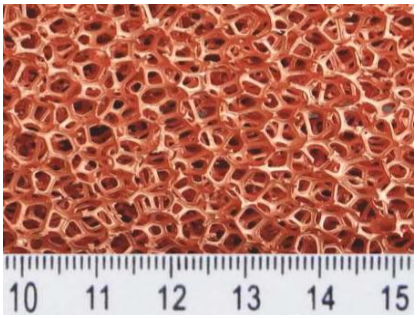


Figure IV.3. Wick image.

Mean Pore diameter (mm)	0.638
Porosity (%)	96
Permeability (m^2)	1.238 10^{-6}
Effective thermal conductivity (W/*m*K)	16.24

Table IV.2. Porous media properties.

IV.2.1.4 Thermal resistance:

In order to describe the thermal performance of the evaporator, we define the evaporator thermal resistance (Coefficient of heat transfer) as follows:

$$R_T = \frac{T_c - T_{w,in}}{\varphi}$$

Where φ refers to the heat flux applied to the evaporator, T_c is the casing temperature and $T_{w,in}$ is the liquid temperature at the wick inlet.

IV.2.2 Experimental results and discussion

IV.2.2.1 Heat transfer characteristics

Casing temperature, T_c, was measured and presented as a function of applied power for different fluids used in this experiment (Pure water, butanol solution and gold nanofluids). **Fig. IV.4** describes the temperature evolution of the casing temperature for different working fluids at steady state.

First experiment was done using pure water liquid as a reference to this work in order to observe the effect of other liquids on convective heat transfer coefficient, *h* °C/W. This figure shows that as the heat load increases, the temperature of the evaporator also increases. These values of heat load were set after the analysis done in [120] to select the good range limit compared to heat transfer coefficient and the adverse hydrostatic head. Both of gold nanofluid and butanol aqueous solution, the casing temperature is always lower than that pure water. During the operation of an evaporator filled with gold nanofluids (1% C_v), the casing temperature is approximately 145 °C whereas for the pure water the temperature is about 155 °C for a heat load of 85 W. While for the self-rewetting butanol solution with 3% C_v, the casing temperature was 140 °C which is less than the gold nanofluids. Finally, a self-rewetting gold nanofluid with 1%Au and 3%butanol % C_v exhibits the best performance with 137 °C for the same heat load 85 W. The over heat in the evaporator casing was higher for water because the vapor pocket developed inside the porous wick was large too.

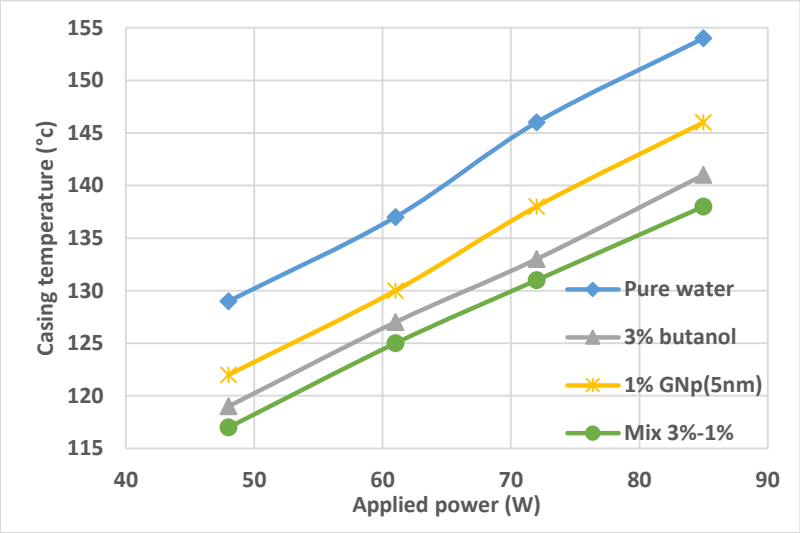


Figure IV.4. Casing temperatures variation for water, self-rewetting fluid (butanol) and gold nanofluid at each input power.

After measuring the casing temperature and the temperature at the wick inlet, the variation in the thermal resistance as a function of the applied power for the working fluids is shown in **Fig. IV.5**. It can be seen that the use of a self-rewetting or nanofluids reduce the thermal resistance of the

evaporator. Also, a mixed solution of self-rewetting gold nanofluids shows the lowest thermal resistance of 22% compared to that of pure water.

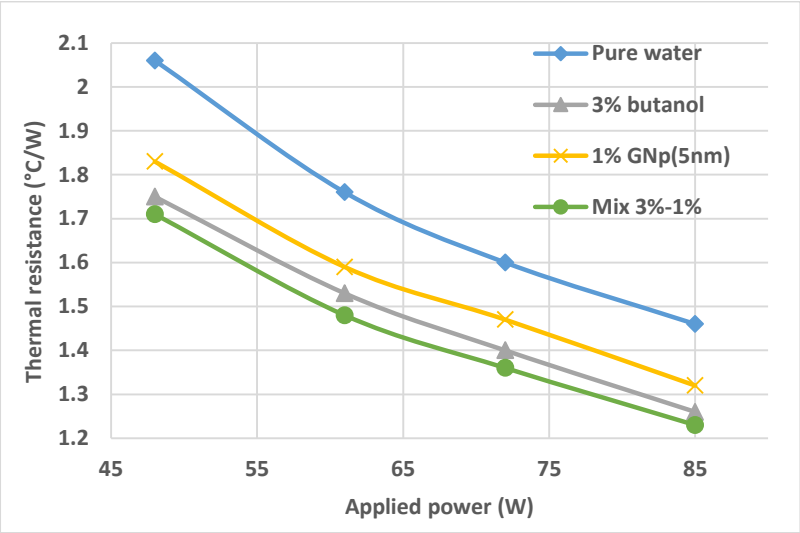


Figure IV.5. Thermal resistance for water, butanol self-rewetting and gold nanofluids.

IV.2.2.2 Vapor pocket dynamics

In order to understand the enhancement in the thermal performances of the evaporator using nanofluids and self-rewetting solution, the liquid/vapor phase change has been visualized. **Fig. IV.6**, presents the evolution of the vapor pocket as a function of the applied power for all working fluids. It can be seen that the size of the vapor pocket increases as the applied power increased. This results can be explained by the fact that the increase in the heat load causes a higher vapor mass flow rate at the outlet of the evaporator. As a results, the mass flow rate of the liquid at the outlet of the reservoir also increases, resulting in a lower liquid temperature at the inlet of the wick. Both of these effects tend to stabilize the vapor pocket within the capillary structure. This explanation is in agreement with the numerical results of Boubaker [121] and Ren [122]. So, as the vapor pocket developing inside the porous wick, means a high thermal resistance which promotes overheating of the evaporator casing and affects the thermal performance of the evaporator.

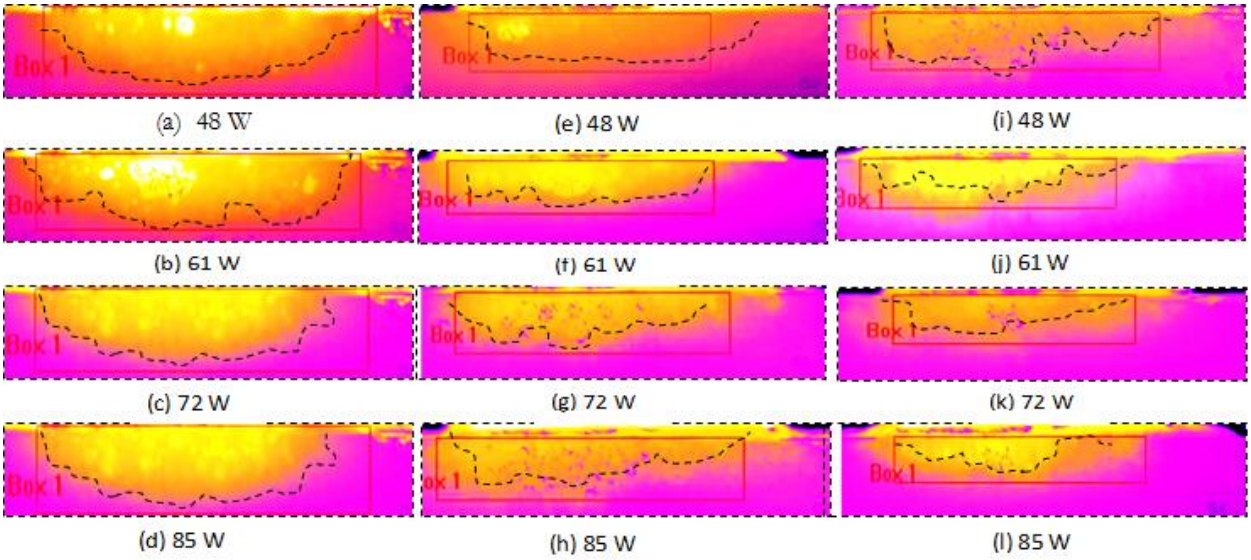


Figure IV.6. Comparison of the vapor pocket for water, gold nanofluid and self-rewetting nanofluid.

For that reason and unlike the water, the vapor zone at the liquid/vapor decrease by increasing the applied power for the gold nanofluid, butanol and self-rewetting nanofluid. The thermal resistance of the vapor pocket inside the capillary structure thus decrease, which explains the decrease in the temperature of the casing evaporator and the increase in thermal performance of the evaporator when it is filled with a self-rewetting nanofluid.

To demonstrate how these fluids improved the thermal performance of the CHP evaporator, we presented and calculated the physical properties associated with the thermal conductivity, surface tension (Marangoni forces), wettability, stability and capillarity for each fluid.

The improvement of the thermal performance of the evaporator for the water/gold nanofluid comes mainly from the stability and thermal properties of gold nanoparticles in addition to its physical phenomena associated with the marangoni forces [111]. The thermal conductivity of gold nanofluid, **Table. IV.3** was calculated after applying the model of Leong et al.

It showed the increase in thermal conductivity compared to pure water. Also, the stability of 5nm gold nanoparticles was studied, in my latest work (Zaaroura et al) [52, 111], and showed a good stability inside fluid during droplet evaporation. Moreover, the Marangoni lifetime of same type of nanofluid showed the longest period compared to pure water.

Temperature °C	Thermal conductivity (W/k.m)	
	Water	5 nm, 1% C_v Gold nanofluid
20	0.589	0.662
50	0.651	0.721
90	0.677	0.738

Table IV.3. Thermal conductivity of gold nanofluid at different temperatures.

Whereas, for butanol/water binary mixture, the measured surface tension exceed that of water when the temperature exceeds 99 ° C. From this temperature capillary pumping is more important for butanol aqueous solution (3% C_v). This explain the decrease in the size of the vapor pocket as a function of the applied heat load [123].

The Marangoni effect takes place when there is a surface tension gradient which can be the results of the existence of a temperature and/or a concentration gradients. As shown in **Fig. IV.7**, the surface tension for butanol solution has a positive gradient form 50 ° C and in this case, the reserve Marangoni flow driven liquid from cold to hot region and as results a decrease in the vapor pocket developed inside the porous section and the casing temperature is significantly reduced.

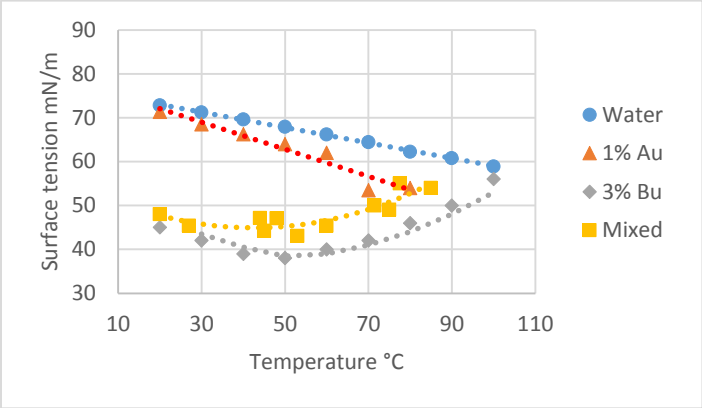


Figure IV.7. Surface tension measurements for water, butanol (3% C_v), gold (1% C_v), and a mixture of butanol self-rewetting gold nanofluid (Bu 3%-Au 1% C_v) using KRUSS Pendant method.

The wettability measurements indicates that adding alcohols, particularly butanol, decrease the contact angle and increase the contact area with metals whatever the nature of the substrate: smooth or porous substrate. It was difficult to measure the contact angle of the water/butanol mixture for porous copper oxide because of its easily and quickly spreading.

Fluids	T_{sur}= 25 °C		T_{sur}= 65 °C	
	Smooth copper	Porous copper	Smooth copper	Porous copper
Water	79.4	70.66	77	73
Gold, 1%C_v	78.3	65	75.6	<30
Butanol, 3% C_v	64	<20	56	Spontaneous spreading
Mixed solution (1%Au/3%Bu/water)	58.1	<10	60	Spontaneous spreading

Table IV.4 Contact angle measurements.

Finally, interesting results were found after a combination of the properties of the self-rewetting butanol solution and gold nanoparticles in a solution in the form of butanol self-rewetting gold nanofluid. This mixture gave the best performance by reducing the thermal resistance of the evaporator by 22 %. It can be seen that the surface tension of this mixture, see **Fig. IV.7**, increases

with respect to the butanol solution and gives the same behavior. Furthermore, its wettability was improved and maintained spreading above porous substrate.

This mixed gave the best performance by decreasing the evaporator thermal resistance by 22 %. We can find that the surface tension of this mixture increased compared to the butanol solution and provide the same profile.

IV.3 Thermal performances of a micro heat exchangers using nanofluid and self-rewetting fluid

IV.3.1 Experimental method

IV.3.1.1 Polydimethylsiloxane (PDMS) - based microchannel device, microfabrication and experimental facility.

An aspect-ratio ($a = \frac{W_{ch}}{H_{ch}} = 5.65$), rectangular cross-section (Width, W_{ch}=2.26 mm, height, H_{ch}=400 µm and length L_{ch}=20 mm) Polydimethylsiloxane (PDMS-based microchannel, with a hydraulic diameter (D_h) of 680 µm, was designed. A photograph of the PDMS microchannel device is displayed in **Fig. IV.7**. It shows the transparent PDMS microchannel device with the dimensions of the channel used for the experiment. The bottom surface is the ITO /glass and the top surface is the PDMS. The back side of the 0.4 mm thick microscope glass slide (30 x 50 mm^2) was coated with a 200 nm conductive transparent thin film of indium tin oxide (ITO), deposited using magnetron sputtering [124], to facilitate the heating of fluid in the channel. **Table IV. 3**. Summaries the dimensions of the different parts that comprise the PDMS microchannel devices.

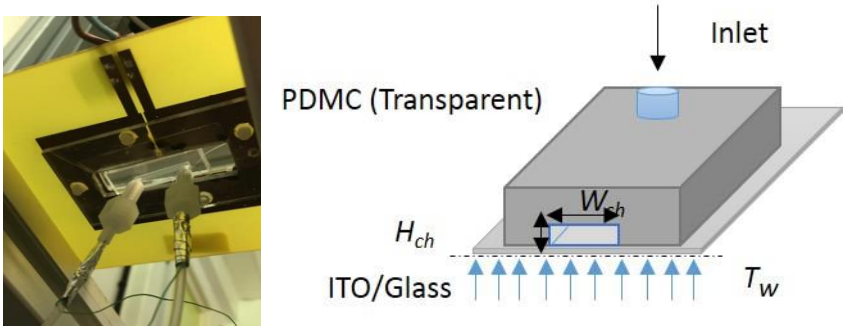


Figure IV.8. PDMS microchannel, bonded to ITO coated glass.

Materials	H_{ch} (µm)	W_{ch} (mm)	L_{ch} (mm)
Microchannel	400	2.26	20
ITO layers	200 x10^{-6}	30	50
Glass	0.4 mm	30	50
PDMS substrate	2 mm	8	40

Table IV.5. Characteristics dimensions of the different components of the microchannel device.

IV.3.1.2 Microfabrication of Polydimethylsiloxane (PDMS) microchannel

For the purpose of this work, PDMS was used to fabricate single microchannel rectangular cross section. It is the most commonly used polymer in recent years for rapid prototyping and microfluidic applications. It is easy for fabrication of microfluidic devices with casting and curing procedures. It is an inexpensive material which is transparent to both the mid-infrared spectrum and the visible spectrum. The transparency to infrared radiation of the PDMS wall allows for synchronous inner wall temperature measurements and optical visualization. **Fig. IV.8**. Present the fabrication process of PDMS microchannel done in IEMN laboratory. A mixture of PDMS and is done with 1/10 ratio quantity. Then, it was putted in a vacuum chamber, around 1 hour, to eliminate all the bubbles.

After that, the mixture is poured onto the rectangular mold and put in an oven at 70 degrees for 3 hours. After curing, the PDMS was peeled off carefully from the mold. Inlet and outlet holes of 2 mm diameter were punched into reservoirs using biopsy puncher to define the inlet and outlet for fluids. Then, the bottom of the channel was plasma treated following oxygen plasma activation and bonded to a glass slide that is not coated with ITO. Plasma activation causes the PDMS surface to reorder so that it has -OH groups oriented at the surface and these can bond easily to glass to create a tight seal.

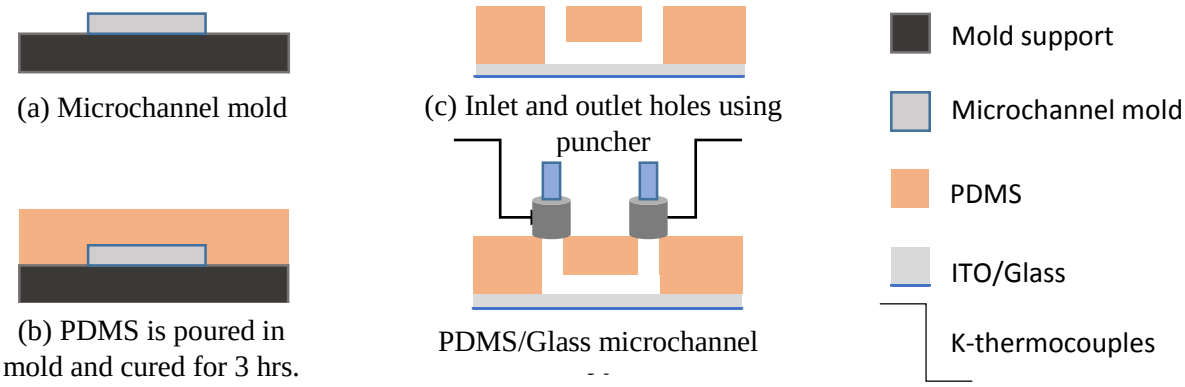
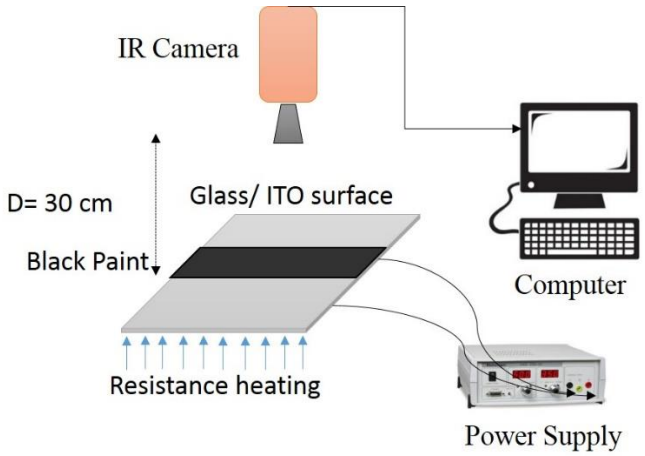


Figure IV.9. Schematic view of integration steps of the PDMS microchannel with the inlet and outlet flow.

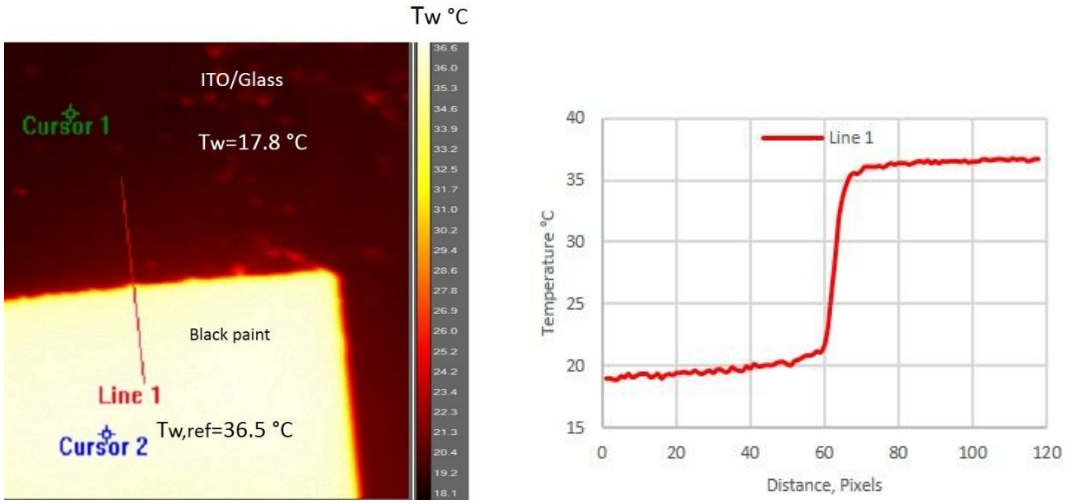
IV.3.1.3 Surface emissivity measurements of ITO coated glass and PDMS for infrared thermography

Knowing the surface emissivity is very important during measuring the temperature of the surface of an opaque object by infrared thermography. For this reason, it is necessary to know the surface emissivity of the examined object. The emissivity of ITO/glass as well as PDMS was measured following the calibration method followed by Madding et al. [125]. Figure shows the calibration setup for the emissivity measurements. High emissivity (paint=0.98) black paint is applied as a reference. The black paint is placed above the samples (ITO/glass and PDMS), **Fig. IV.9**. Then the IR camera lens (FLIR X6580 SC high-speed Infrared camera-high resolution of 640 x 512 pixel) should be adjusted to a distance of 30± 1cm from the surface of the black paint in order to be able to measure the temperature with good observation.

The samples and the copper were heated using a resistance connected with a DC power supply and as the power was increased, temperature measurements were made by capturing thermal images with the IR camera, Figure. A K-type thermocouple was attached to the sample surface in order to validate the temperature measurements obtained from the IR camera.



(a)



(b)

Figure IV.10. (a) Setup for calibration of surface emissivity and (b) Thermal image from the IR used to measure the emissivity of ITO coated glass and PDMS in reference to the emissivity of the black paint.

Fig. IV.10 shows the emissivity measurements as a function of surface temperature for the temperature range of 35 - 75 °C for the ITO coated glass, PDMS and black object.

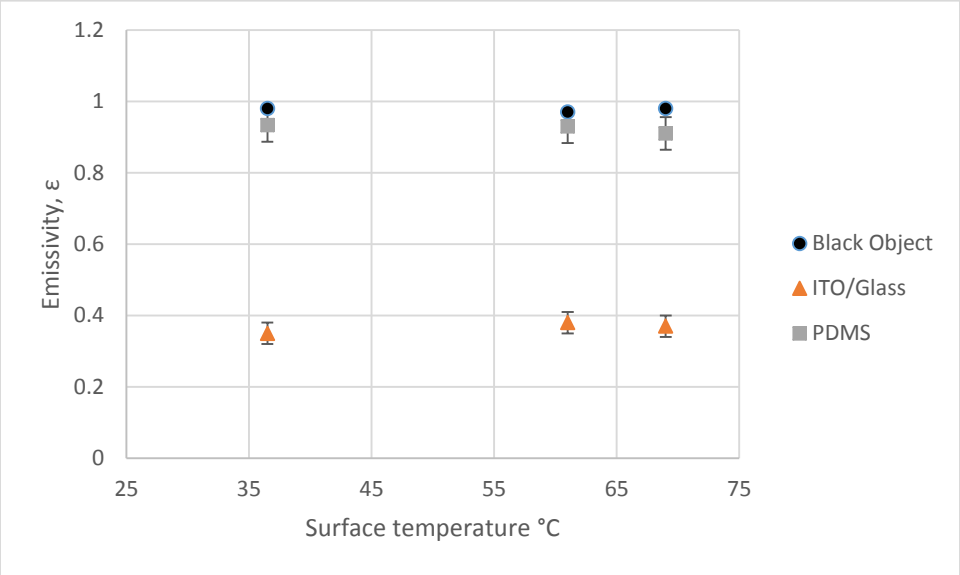


Figure IV.11. Surface emissivity measurements of ITO/glass and PDMS with increasing temperature.

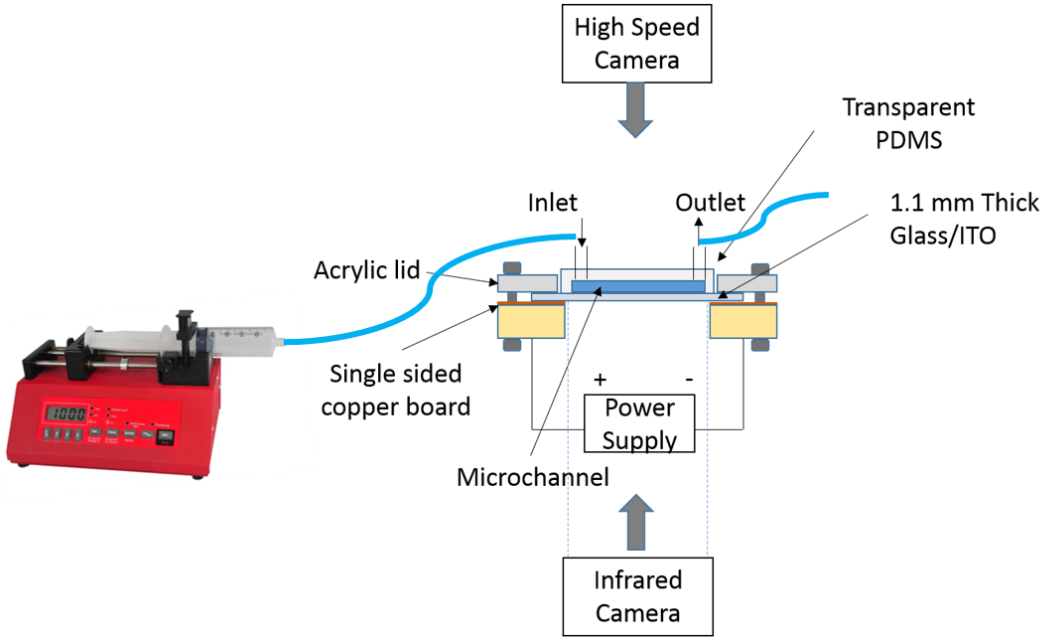
IV.3.1.4 Working fluids used in the experiment

Gold nanoparticle dispersions and self-rewetting solution were used as a working fluids in this experiment. Properties of these fluids are given in **Table IV. 4**. Samples were diluted to the necessary volume concentrations with distilled water, 1% C_v, 8% C_v for the gold nanofluid and 3% C_v for the butanol solution.

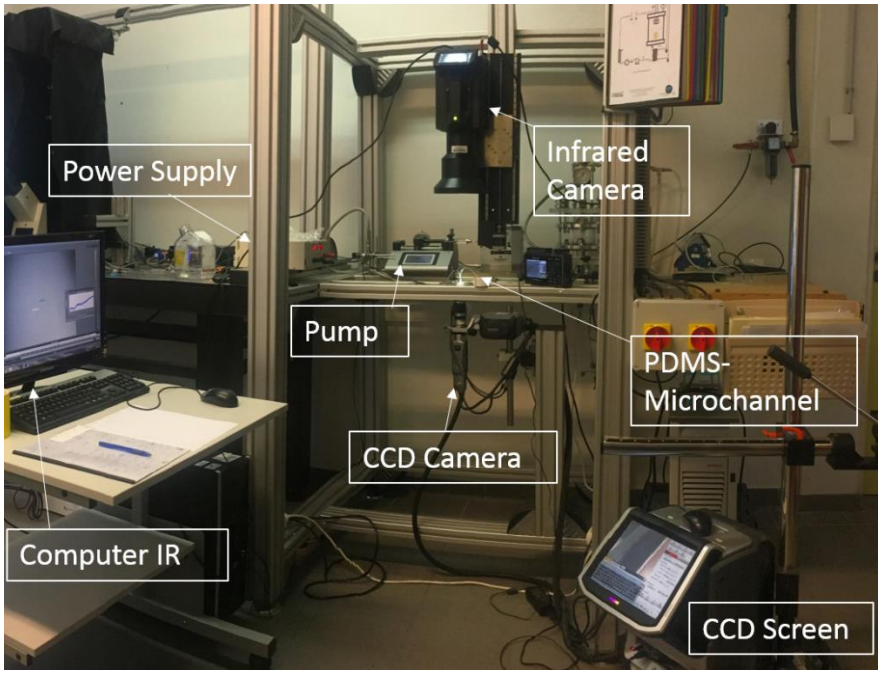
Fluids types	Density, ρ (kg/m^3)	Particles size, nm	Volume concentrations, % C_v	Thermal conductivity, k $(W/K.m)$	Heat capacity, C_p $(J/kg.k)$
Water	997	-	-	0.6	4182
Gold nanoparticles, Au	19320	5	1% and 8%	327	130
Butanol solution	810	-	3%	0.1553	2400

Table IV.6. Thermophysical properties of the working fluids at ambient temperature. [126, 127]

The constructed experiment set up is shown in **Fig. IV.11.** The apparatus consisted of three sections which are pump section, test section and data acquisition section. The liquid was taking and pumped out to the channel. Upon exciting the pump, the flow is controlled before entering the test section and settled at two different flow rates, 0.15 and 0.20 ml.min^{-1}. The connection from the pump to the channel was used a circular pipe. The fluid flow was considered to be in laminar flow. The test section is consisting of a PDMS/glass microchannel and a copper based specimen in order to heat down by adjusting the Watts amount to the heat needed (Starting from ambient to 90 °C wall temperature). Two K-thermocouples have been located at the inlet and outlet of the channel to measure the fluid temperature. In addition to an infrared camera located above the glass/ITO section to measure the wall temperature across the whole microchannel.



(a) Experimental setup.



(a) Experimental setup in real view.

Figure IV.12. Schematic of experimental apparatus.

IV.3.2 Data reduction

The temperature measurements were obtained from the channel outer wall of the glass base. The analysis of IR data showed uniform heating of the microchannel as the temperature gradient was constant, without local temporal variations of temperature in excess of 1.1 °C. The conversion factor for the IR images was 15.39 mm/ pixel and was calibrated to the width of the microchannel.

The Biot number that indicates the temperature uniformity within the channel by comparing the conduction resistance to the convection resistance was calculated as:

$$Bi = \frac{h_{conv}\tau_w}{k_{ch}} \quad (1)$$

Where τ_w is the channel wall thickness, k_{ch} the thermal conductivity of the glass and h_{conv} is the convective heat transfer coefficient calculated from Newton's cooling law:

$$Q_{eff} = h_{conv}A(T_w - T_f) \quad (2)$$

Where T_w is the outer wall temperature of the channel and T_f is the fluid temperature, A is the outer channel surface and Q_{eff} is the power transferred to the liquid (**Eq. (4)**). Since Bi was found to 0.22, which is less than 1, with ±6% uncertainty, the difference between the inner and outer wall temperature could be neglected. The heat transfer losses for single phase flow conditions were estimated from the energy balance:

$$Q_{loss} = Q_{ITO} - Q_{eff} \tag{3}$$

Where Q_{ITO} the total input power is provided to the ITO glass surface (30 x 50 mm^2), determined using Joule's first law and Q_{eff} is the effective heat transferred to the liquid in the microchannel which was estimated from:

$$Q_{eff} = \dot{m} \times C_{p,l}(T_{l,out} - T_{l,in}) \tag{4}$$

Where $T_{l,in}$ and $T_{l,out}$ are the inlet and outlet liquid temperatures, $\dot{m}$ is the mass flow rate inside the channel and $C_{p,l}$ is the specific heat capacity of liquid calculated at the mean temperature of the liquid.

The average heat flux at the wall was calculated from:

$$q(x,y) = \frac{Q_{eff}}{A} \tag{5}$$

Where A is the channel surface area ($A=W_{ch} \times L_{ch}$). The local liquid temperature was calculated based on the assumption that all the effective heat flux was used to heat up the liquid:

$$T_l(z) = \frac{q(x,y) \times W \times z}{C_{p,l} \times \dot{m}} + T_{l,in} \tag{6}$$

Where W is the channel width, z the distance from the channel inlet, $T_{l,in}$ is the inlet temperature of the liquid. The local heat transfer coefficient was calculated using:

$$h_{cv}(x,y) = \frac{q(x,y)}{(T_{w,IF} - T_l(z))} \tag{6}$$

Where $T_{w,IF}$ the wall surface temperature measured using infrared camera.

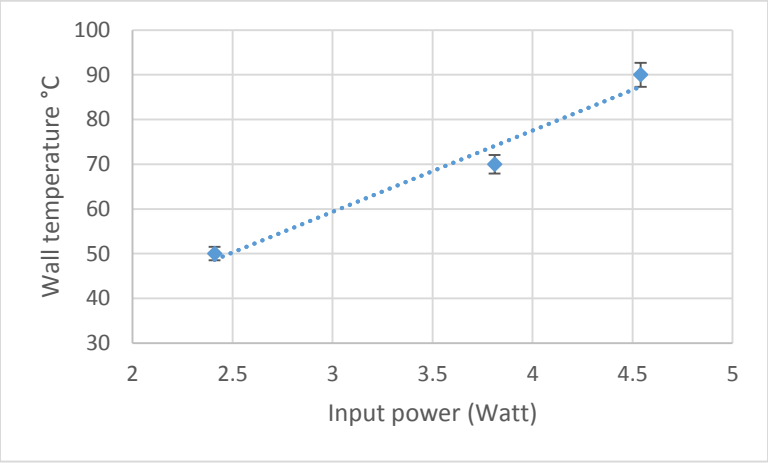
For the experiments presented in this paper, the main uncertainties are identified in **Table IV. 5**.

IV.3.3 Results and discussion

Wall temperature measurements with an infrared camera were carried out across the whole microchannel in order to evaluate the ITO/glass heating uniformity. The IR camera measured the two-dimensional wall temperature map with increasing power without any liquid in the microchannel. Input power was increased from 2.41 to 4.54 W. A linear relationship was established between the input power and spatially averaged wall temperature measurements using infrared thermography. **Fig. IV.12**, presents the wall temperature measurements obtained by infrared camera for the 0.4 mm thick glass as function of input power.

Parameter	Maximum uncertainty
Standard K-type thermocouple	± 0.7 °C
DC power supply	± 2.5 %
IR camera measured temperature	± 1.1 °C
Heat flux	± 3.5 %
Heat transfer coefficient	5%

Table IV.7. Summary of measurements uncertainties.



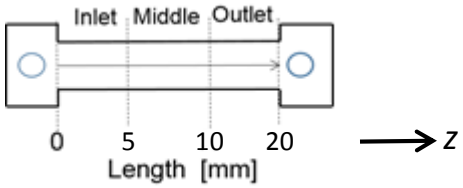


Figure IV.13. Wall temperature measurements obtained by infrared camera for 4 mm thick glass as function of input power.

The wall temperature of the microchannel is shown in **Fig. IV.13** at different input powers (**Fig. IV.14**) to prove the uniformly of the surface temperature through the channel.

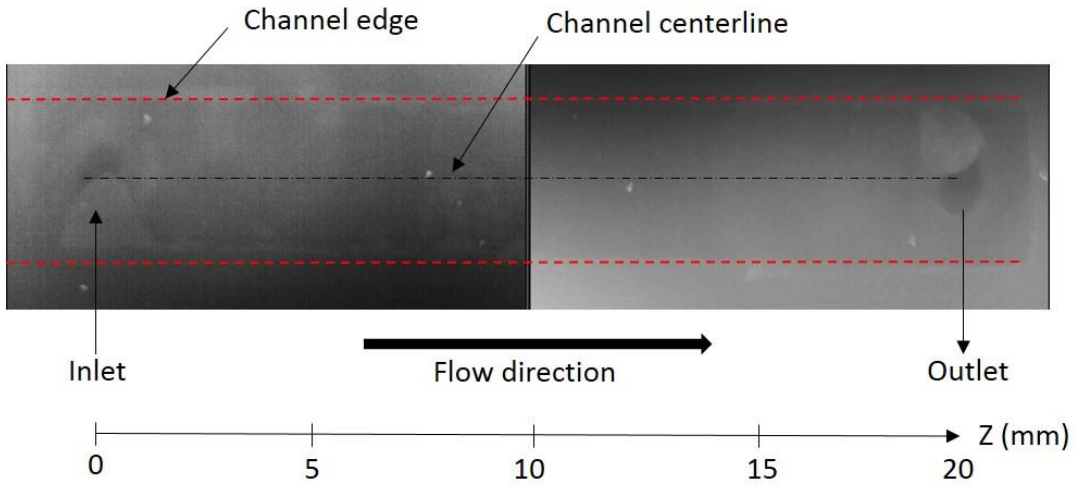
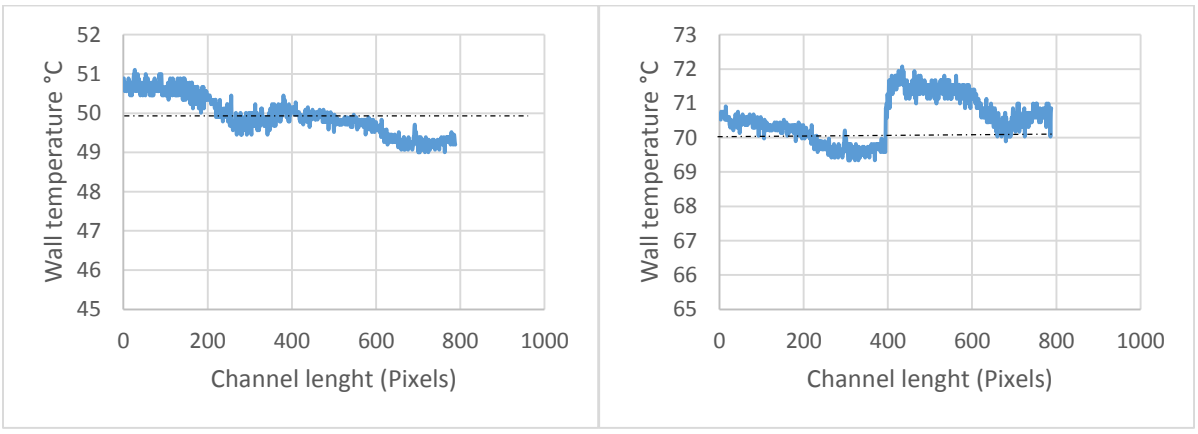
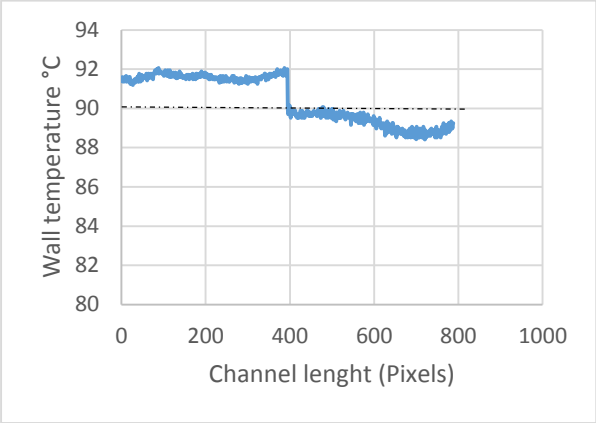


Figure IV.14. Thermal image of the microchannel using infrared camera without liquid flow.



(a) (b)



(c)

Figure IV.15. Axial microchannel temperatures, without fluid, at different input powers (a) T_w=50 °C (b) T_w=70 °C and (c) T_w=90°C.

IV.3.3.1 System calibration: Water as a reference

System calibration runs were carried out with water to check the validity of the experimental procedure before the experiments with gold nanofluid and butanol self-rewetting fluid. First, accuracy of the heat transfer measurements was tested by calculating the convection heat transfer coefficient without fluid flow inside the microchannel as a natural convection. The coefficient was found equal to 2.1 W/K.m^2 which is close to the theoretical range values for natural air convection flow [128]. The coefficient was calculated using:

$$P_{eff} = \frac{(U \times I) \times V_{ITO}}{V_{ITO} + V_{Cu}} = Q_{rad} + Q_{conv} \quad (7)$$

$$Q_{rad} = \varepsilon \sigma A_{ITO}(T_{w,IF}^4 - T_{air}^4)$$

$$Q_{conv} = hA_{ITO}(T_{w,IF} - T_{air});$$

Also, the convection coefficient was extracted from the Nusselt number correlation for microchannel rectangular section in a fully developed laminar flow [129]. This value referred to water flow inside the microchannel at specific surface temperature. The heat transfer coefficient was calculated using the following equation:

$$N_u = \frac{D_h \times h}{k}$$

Where *h* is the convection coefficient, *k* is the thermal conductivity of fluid and D_h is the hydraulic diameter. The convection heat transfer coefficient was found equal to be 5382.3 W/k.m^2 which is within the range of the experimental data.

4.2 Gold nanofluid and Butanol self-rewetting liquid as a working fluids

In order to investigate the heat transfer characteristics of nanofluid flow and self-rewetting fluid, Gold/water combination with different concentrations 1% and 8% C_v was used as the working fluid as well as Butanol/water with 3% C_v. Clearly, the thermal fluid properties of the nanofluid have to be updated. The density and specific heat calculated based on equation bellow:

$$\rho_{nf} = (1 - \emptyset)\rho_{bf} + \emptyset\rho_p \tag{8}$$

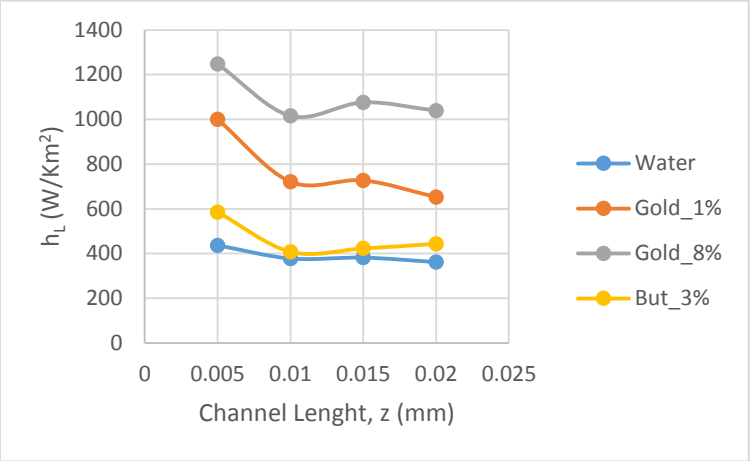
Where ρ_{bf} is the density for base fluid (water) and ρ_p is the density for particle. The specific heat for gold nanofluid is expressed:

$$C_{p,nf} = (1 - \emptyset)C_{p,bf} + \emptyset C_{p,p} \tag{9}$$

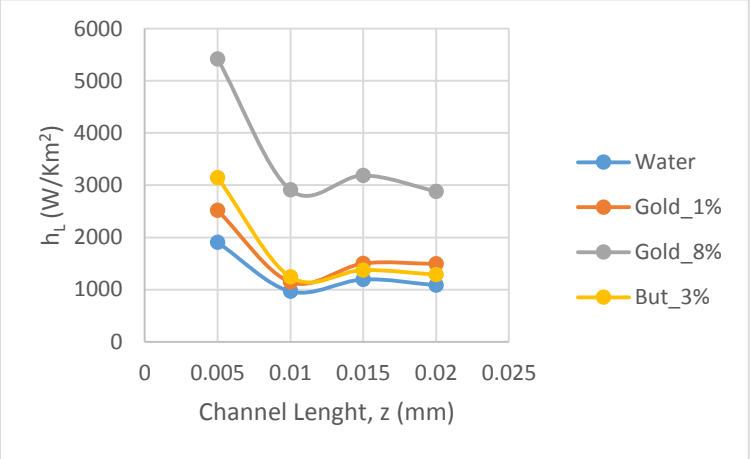
Leong et al. [130], was also used for determination of effective thermal conductivity of nanofluid as follows:

$$\begin{aligned} k_{eff} = &\Big(\big(k_p - k_{lr}\big)\emptyset_p k_{lr}\big[2\beta_l^3 - \beta^3 + 1\big] + \big(k_p - 2k_{lr}\big) \times \\ &\beta_l^3\big[\emptyset_p\beta^3\big(k_{lr} - k_f\big) + \\ &k_f\big](\beta_l^3\big(k_p + 2k_{lr}\big) - \ \big(k_p - k_{lr}\big)\emptyset_p[\beta_l^3 + \beta^3 - 1]^{-1} \end{aligned} \tag{10}$$

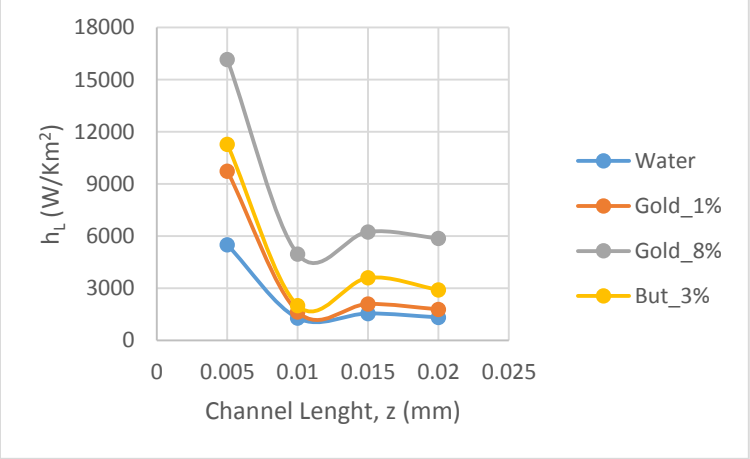
Experimental results regarding the convection heat transfer coefficient of the working fluids (Water, Gold nanofluid and butanol) flowing in a rectangular microchannel at constant flow rate (0.15 ml/min) are described in **Fig. IV.15.**



(a) P_1= 2.41 W



(b) P_2=3.81 W



(c) P_3=4.54 W

Figure IV.16. Variation of local convective heat transfer coefficient of gold nanofluid (1 and 8% C_v), Butanol (3% C_v) compared to pure water base fluid at each input power along the microchannel length.

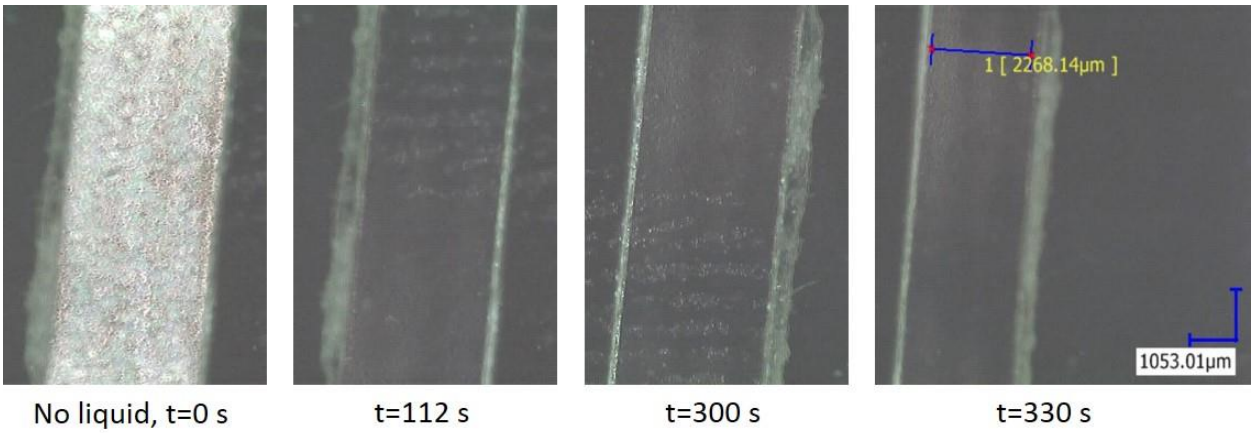
The results showed that the gold nanofluid with 8% C_v has the highest and the best thermal performance presenting by the convection heat transfer coefficient at each input powers, using (**Eq. (6)**). While, the self-rewetting fluid showed an increase in the convection heat transfer coefficient as the surface temperature increased above the 50 °C. At first input power P_1, the convection coefficient of butanol was lower than that of gold nanofluid with the two different concentrations. Whereas, as the power increased, the convection coefficient start to increased and reach values higher that the gold nanofluid with 1% C_v. These variations are due to the change in thermal properties for each fluid. The thermal conductivity of gold nanofluid showed the highest value with 8% C_v compared to 1% C_v, water, and butanol (**Table IV.6**).These values were calculated using **Eq. (10)**. Also, self-rewetting fluids showed a good performance due to its properties at a certain temperature (starting from 60 °C) by enhancing the thermal and solutal marangoni forces. This behavior can clearly observed by the increase in the convection coefficient at input power P_2 and P_3 (70 and 90 °C surface temperatures). **Fig. IV.13** shows the IR images of the microchannel from the transparent ITO/glass section to detect and measure the wall temperature of the microchannel during the operation.

Temperature, °C	Thermal Conductivity, k (W/k.m)		
	Water	Gold, 1%	Gold, 8%
20	0.598	0.662	1.15
50	0.651	0.721	1.25
90	0.677	0.738	1.29

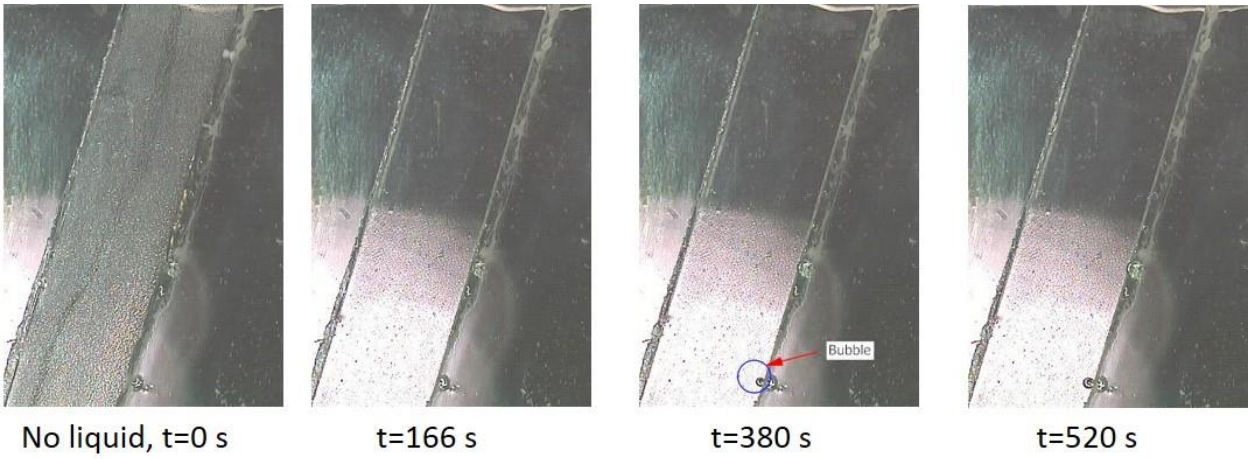
Table IV.8. Thermal conductivity of water and gold nanofluids as a function of volume concentrations and at different temperatures.

At the same time, the high speed camera (Keyence) was used to detect if any deposition could be happen due to instability of nanoparticles during the flow. **Fig. IV. 16** presents, at different times, the snapshots from the PDMS side during the flow of water and gold nanofluid (1% C_v).

The results showed no particles deposition during fluid flow which improved the enhancement in the convection coefficient. Since it is known that the effect of nanoparticles deposition on thermal performance. Analysis on the dynamic deposition of same type of gold nanofluid (5nm) has been analyzed as a local deposition during droplet evaporation (Chapter 3).



(a)



(b)

Figure IV.17. Sequence of optical images that reveal the typical flow regimes of the microchannel. (a) The optical images for pure water flow at P_1 input power (b) The optical images for 1% gold/water nanofluid flow at P_1 input power.

The comparison was based compared to pure water flow at the same conditions. Also, No bubbles formed during the flow of fluids, only with very small formation at the edge for the gold nanofluids. This little variation can be neglected.

It is clear from **Fig. IV.17** that the local convection coefficient, for the pure water, is increased as the Reynolds number increases due to decrease in the wall temperature of the microchannel. The Reynolds number was calculated as follow:

$$Re = \frac{D_h \dot{m}}{A_c \mu} \tag{11}$$

In **Fig. IV.17** the variation in the local convection coefficient of the microchannels at different Reynolds number is presented.

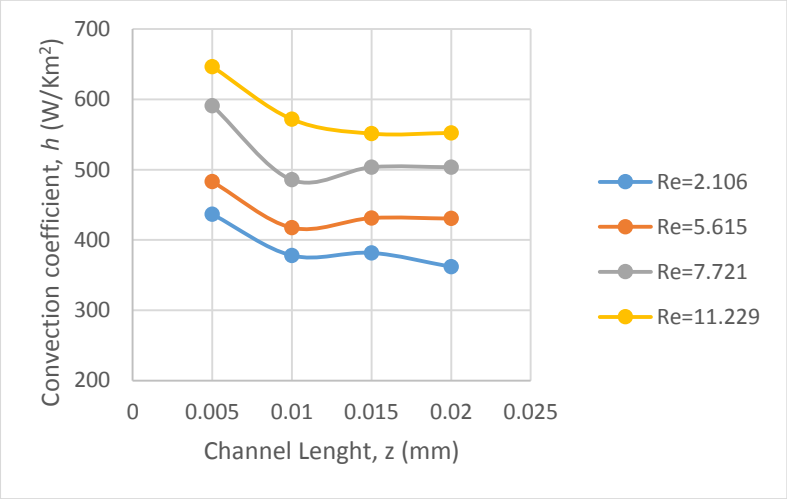


Figure IV.18. Variation of local convective heat transfer coefficient of pure water along the microchannel length.

IV.4 Conclusion

In this chapter, effect of using gold nanofluid and self-rewetting fluids (butanol) was investigated experimentally to observe their impact on the heat and mass transfer in a porous media of two-phase heat transfer device. Several specifications of nanofluids are influential in heat transfer behavior like stability, concentration and the type of nanoparticles.

It is found that gold nanofluid (5 nm with 1% $C_{v)}$, in this experiment, exhibits a very good characteristics in thermal behavior of CHP. Also, the average thermal resistance of the evaporator is reduced by 13 % compared to pure water. Whereas, the self-rewetting fluid (3% C_v butanol) observed a better performance of heat transfer by 16% reducing in thermal resistance.

Finally, a mixture is made of self-rewetting gold nanofluids (1%Au, 3%Butanol /water) in order to see the combination impact on thermal performance. Lower thermal resistance of 22% is finally observed and the best performance is obtained in CHP compared to pure water. The reasons for thermal performance improvement of the CHP with these fluids are due their thermophysical properties, wettability, capillary, and marangoni forces.

At the same time, an experimental investigation examine the heat transfer behavior of Gold nanofluid and butanol self-rewetting fluid in a micro PDMS heat exchanger. The tested fluids was 1% and 8% C_v for gold nanofluid and 3% C_v for butanol solution with water. The fluid flows inside the microchannel (hydraulic diameter (D_h) of 680 μm) using a mechanical pump at constant flow rate (0.15ml/min) for all the experiments. A high speed infrared camera has been adjusted to visualize and measure the wall temperature from the ITO/glass side where as an optical CCD camera fixed from the PDMS section for particles detection deposition and any special behavior such as bubbles formation. The local convection heat transfer coefficient was calculated for each types of fluid through the microchannel. The results showed that the highest heat transfer enhancement is observed for the gold nanofluid with 8% C_v with water. This change, compared to 1% C_v and butanol self-rewetting is due to the increase in the properties of fluid presenting by thermal conductivity. In addition to the stability behavior that observed and detected by the Keyence high speed camera during the flow.

Butanol self-rewetting solution showed an increase in the local convection coefficient as the input power increased (from 70 °C surface temperature). This increase due to the thermal properties defined by thermal and solutal marangoni forces. Reynolds effect was also presented for water on the local convection coefficient that showed an increasing in the convection heat transfer coefficient as the Reynolds increased due to the decreasing in the wall temperature.

Chapter .V General conclusion and perspectives

V.1 Conclusion and perspectives

We have seen in this work that improving performance and efficiency energy of an industrial thermal system comes down to working on a new smart fluids to be used as working fluids, namely nanofluids and self-rewetting fluids.

In Chapter 2, the analysis first focused on the stability of nanoparticles inside sessile droplets during their evaporation. The results showed that copper oxide nanoparticles cannot be used as an effective nanofluids due to its non-stability inside the fluids. This instability affected the thermal performance since the effective thermal conductivity is deteriorated. The analysis was conducted using optical and infrared methods as well as an acoustic method which showed some promise to follow any kinetics deposition due to its high sensitivity at the solid/liquid interface. Consequently, the acoustic method, presented by modulus of longitudinal reflection coefficient, open access as a first interest to study the dynamic deposition of nanoparticles at the liquid-solid interface. This convergence of results, obtained from two different techniques, constitutes a very important step for understanding the deposition phenomenon of nanofluids. Nanoparticle concentrations have also been estimated from the acoustic method from the longitudinal reflection coefficient. Moreover, the infrared camera permitted to observe convection cells at the droplets surface caused by Marangoni effect due to the big contact angle of the droplet. This behavior is noticed by the change in the gradient temperature of the droplet surface. The results showed the effect of Marangoni flow on the delay time of the nanoparticles deposited on the substrate, but also an increase in the surface temperature causing an increase in the area of the dried nanoparticles distribution on the substrate, forming a ring shape with inner deposition.

The acoustic method, based on a high frequency reflectometry principle, provide a detailed analysis to measure one of the most important physical properties of nanofluids, namely the shear viscosity. Measuring the shear viscosity of a droplet of gold nanofluid (5 nm) during the evaporation process was done by measuring the mechanical impedance of the liquid, which has a complex form due to the attenuation of the sound energy propagating inside the nanofluids (viscoelastic losses). From shear reflected wave, an online measurement of the shear viscosity was obtained throughout all the evaporation process. The viscosity of 5 nm gold nanofluid has been extracted as a function of volume concentrations of nanoparticles.

These measurements occurred after the development of the used transducer by a blind technique which changes the orientation of the ZnO deposition on the silicon substrate and as a results a higher shear reflection coefficient can be generated.

In Chapter 3, other types of nanofluids, specifically gold nanoparticle have been selected to investigate their thermal performance during droplet evaporation. The effect of nanoparticles sizes (2.2 to 10 nm) and different buffer solvents (Citrate-Capping PBS and PBS only) were also studied. The results showed that, in comparison to the evaporation of distilled water droplets, the nanofluids droplets evaporate more rapidly as the surface temperature increases for both solutions. In addition, gold nanofluids with PBS solution showed that the smallest nanoparticle size (5 nm) has the greatest impact on the evaporation rate (+35% more) than the larger nanoparticle while the addition of citrate solution showed opposite results, the larger nanoparticle have the greatest improvement on evaporation rate but still less than the solution with PBS only (+15%). This variation with the citrate solution is due to the non-stability of nanoparticle inside the droplet detected by high frequency acoustic waves at the substrate /droplet interface compared to gold nanoparticles with PBS solvent that showed a stability inside the droplets during the evaporation process. This stability and non-stability showed its effect on the appearance and disappearance of the convection cells on droplet surface.

In Chapter 4, we studied experimentally the impact of using the best selected gold nanoparticle of 5 nm in diameter and 1% C_v volume concentration on thermal performance of two-phase heat transfer device. Also, a self-rewetting fluid of 1-butanol solution was also used as a working fluid for this system. It is found that a gold nanofluid (5 nm with 1% $C_{v),}$ in this experiment, exhibits very good characteristics in thermal behavior of CHP. Also, the average thermal resistance of the evaporator is reduced by 13 % compared to pure water. Whereas, with the self-rewetting fluid (3% C_v butanol), we observed a better performance of heat transfer by an order of 16% reducing in thermal resistance. Finally, a mixture is made of self-rewetting gold nanofluids (1%Au, 3%Butanol /water) in order to see the combination impact on thermal performance. Lower thermal resistance of 22% is finally observed and the best performance is obtained in CHP compared to pure water. The reasons for thermal performance improvement of the CHP with these fluids are due their thermophysical properties, wettability, capillary, and marangoni forces.

Furthermore, Chapter 4 presented the thermal investigation, same fluids used in the two-phase heat transfer device, inside a micro heat exchanger. The results showed the improvement in the convection heat transfer coefficient after using gold nanofluids and self-rewetting fluids.

Subsequently, we will carry out tests with these fluids on a full heat pipe system. Also, tests using other types of fluids, such as lubricant, silicon oil, will used to investigate their performance on motor cooling.

References

[1] C. T. Nguyen, G. Roy, C. Gauthier, N. Galanis, Heat transfer enhancement using Al_2O_3-water nanofluid for an electronic liquid cooling system, Appl. Therm. Eng, 27 (2006), 1501-1506.

[2] P. Imani Mofrad, S. Zeinali Heris, M. Shanbedi, Experimental investigation of the effect of different nanofluids on the thermal performance of a wet cooling tower using a new method for equalization of ambient conditions, Energy Convers Manage, 158 (2018), 23-35.

[3] M. Rafati, A.A. Hamidi, M.S. Niaser, Application of nanofluids in computer cooling systems (Heat transfer performance of nanofluids), Appl. Therm. Eng, 45(46), (2012) 9-14.

[4] S. Jafarmadar, N. Azizinia, N. Razmara, F. Mobadersani, Thermal analysis and entropy generation of pulsating heat pipes using nanofluids, Appl. Therm. Eng, 103 (2016) 356-364.

[5] U. Choi, Enhancing thermal conductivity of fluids with nanoparticles, ASME Fluid Eng. Div. 231 (1995) 99–105.

[6] N. S. Akbar, M. Raza, R. Ellahi, Copper oxide nanoparticles analysis with water as base fluid for peristaltic flow in permeable tube with heat transfer, Computer Methods and Programs in Biomedicine, 130 (2016) 22-30.

[7] M. P. Beck, T. Sun, A. S. Teja, The thermal conductivity of alumina nanoparticles dispersed in ethylene glycol, Fluid Phase Equilibria, 260 (2007), 275-278.

[8] S. Simpson, A. Schelfhout, C. Golden, S. Vafaei, Nanofluid thermal Conductivity and Effect Parameters, Appli. Sci, 9(1) (2019) 87.

[9] M. Karimzadehkhouei, M. Shojaeian, K. Sendur, M.P. Menguc, A. Kosar, The effect of nanoparticles type and nanoparticle mass fraction on heat transfer enhancement in pool boiling, Int. J. Heat Mass Transfer 109 (2017) 157-166.

[10] Y. Xuan, Q. Li, Heat transfer enhancement of nanofluids, Int. J. Heat Fluid Flow 21 (2000) 58-64.

[11] L. Dongliang, P. Hao, L. Deqing, Thermal Conductivity Enhancement of Clathrate Hydrate with Nanoparticles, Int. J. Heat Mass Transfer 104 **(2017)** 566-573.

[12] S. Simpson, A. Schelfhout, C. Golden, S. Vafaei, nanofluid thermal Conductivity and Effect Parameters, Appli. Sci, 9(1) (2019) 87.

[13] M. Karimzadehkhouei, M. Shojaeian, K. Sendur, M.P. Menguc, A. Kosar, The effect of nanoparticles type and nanoparticle mass fraction on heat transfer enhancement in pool boiling, Int. J. Heat Mass Transfer 109 (2017) 157-166.

[14] G. A. Longo, C. Zilio, E. Ceseracciu, M. Reggiani, Application of artificial neural network (ANN) for the prediction of thermal conductivity of oxide-water nanofluids, Nano Energy, 1(2012), 290-296.

[15] L. Dongliang, P. Hao, L. Deqing, Thermal Conductivity Enhancement of Clathrate Hydrate with Nanoparticles, Int. J. Heat Mass Transfer 104 **(2017)** 566-573.

[16] S. Jafarmadar, N. Azizinia, N. Razmara, F. Mobadersani, Thermal analysis and entropy generation of pulsating heat pipes using nanofluids, Appl. Therm. Eng, 103 (2016) 356-364.

[17] A. Sozen, M. Guru, A. Khanlari, E. Ciftci, Experimental and numerical study on enhancement of heat transfer characteristics of a heat pipe utilizing aqueous clinoptilolite nanofluid, Appl. Therm. Eng, 160 (2019) 114001.

[18] R. Sureshkumar, S.T. Mohideen, N. Nethaji, Heat transfer characteristics of nanofluids in heat pipes: A review, Renewable and sustainable energy reviews 20 (2013) 397-410.

[19] E. Pouzet, J.L. Joly, V. Platel, J.-Y. Grandpeix, C. Butto, Dynamic response of a capillary Pumped loop subjected to various heat load transients, Int. J. Heat Mass Transfer 47 (10) (2004) 2293-2316.

[20] R. Boubaker, V. Platel, Dynamic model of capillary pumped loop with unsaturated porous wick for terrestrial application, Energy 111 (2016) 402-413.

[21] Y. Maydanik, Loop heat pipes, Appl. Therm. Eng 25 (5) (2005) 635-657.

[22] H. T. Zhu, Y.-S. Lin, and Y.-S. Yin (2004). A Novel One-Step Chemical Method for Preparation of Copper Nano-fluids. Journal of Colloid and Interface Science 277: 100–103.

[23] Indranil Manna, Synthesis, Characterization and application of nano-fluids An Overview, 2009.

[24] Sarit, K. Das., Stephen U. S. Choi, A Review of Heat Transfer in Nanofluids, 2009.

[25] B.C. Pak, Y. Cho, Hydrodynamic and heat transfer study of dispersed fluids with submicron metallic oxide particles, Exp. Heat Transfer 11 (1998) 151-170.

[26] Y. Xuan, Q. Li, Investigation on convective heat transfer and flow features of nanofluids, J. Heat Transfer 125 (2003) 151-155.

[27] M. Karimzadehkhouei, M. Shojaeian, K. Sendur, M.P. Menguc, A. Kosar, The effect of nanoparticles type and nanoparticle mass fraction on heat transfer enchancment in pool boiling, Int. J. Heat Mass Transfer 109 (2017) 157-166.

[28] L. Dongliang, P. Hao, L. Deqing, Thermal Conductivity Enhancement of Clathrate Hydrate with Nanoparticles, Int. J. Heat Mass Transfer 104 (2017) 566-573.

[29] Y. Hu, H. Li, Y. He, Z. liu, Y. Zhao, Effect of Nanoparticles Size and Concentration on Boiling Performances of SiO2 Nanofluid, Int. J. Heat Mass Transfer 107 (2017) 820-828.

[30] A.K. Singh, Thermal Conductivity of Nanofluids, Defence Sci. J 85(5) (2008) 600-607.

[31] Engineering ToolBox, (2005). Thermal Conductivity of Metals, Metallic Elements and Alloys. [online] Available at: https://www.engineeringtoolbox.com/thermal-conductivity-metals-d_858.html [18. 06. 2020].

[32] Yu W, France DM, Routbort JL, Choi SUS (2008) Review and comparison of nanofluid thermal conductivity and heat transfer enhancements. Heat Transf Eng 29:432–460.

[33]R. Hamilton, O. Crosser, Thermal conductivity of heterogeneous two-component systems, Ind. Eng. Chem. Fundam. 1 (3) (1962) 187–191.

[34] Einstein A. investigation on the theory of Brownian motion. New York: doverr; (1956).

[35] Brinkman, H.C., The Viscosity of Concentrated Suspensions and Solutions. The Journal of Chemical Physics, 1952. 20(4): p. 571-571.

[36] Corcione M (2011) Empirical correlating equations for predicting the effective thermal conductivity and dynamic viscosity of nanofluids. Energy Convers Manage 52:789–793.

[37] Rudyak VY (2013) Viscosity of nanofluids: why it is not described by the classical theories. Adv Nanoparticles 2:266–279.

[38] Pak BC, Cho YI. Hydrodynamic and heat transfer study of dispersed fluids with submicron metallic oxide particles. Experimental Heat Transfer 1998l 11: 151-70.

[39] Hasan. S, A Review on Nanoparticles: Their Synthesis and Types Biosynthesis: Mechanism 4 (2015) 9–11.

[40] Assessment R, Nanoparticles in the Environment (2007).

[41] Cho E J, Holback H, Liu K C, Abouelmagd S A, Park J and Yeo Y, Nanoparticle characterization : State of the art , challenges , and emerging technologies, (2013).

[42] S. Suresh, M. Chandrasekar, Synthesis of Al_2O_3–Cu/water hybrid nanofluids using two step method and its thermo physical properties, Colloids and surfaces A: Physicochemical and engineering aspects, 388 (2011) 41-48.

[43] W. Yu, H. Xie, A Review on Nanofluids: Preparation, Stability Mechanisms, and Applications, J. Nanomater, (2012) 435873, 1-17.

[44] L. C.H, G.P Peterson, Experimental investigation of temperature and volume fraction variations on the effective thermal conductivity of nanoparticle suspensions (nanofluids), J. Appl. Phys, 99 (2006) 084314.

[45] MAOUASSI AMMAR "Intensification of heat exchanges through the use of nanofluids", Mémoire Magister, Université M'hamed Bougara Boumerdes, Faculty of Hydrocarbons and Chemistry, 2012.

[46] Das SK, Choi SUS, Patel HE (2006) Heat transfer in nanofluids a review. Heat Transfer Eng 27:3–19. doi:10.1080/01457630600904593.

[47] N. S. Akbar, M. Raza, R. Ellahi, Copper oxide nanoparticles analysis with water as base fluid for peristaltic flow in permeable tube with heat transfer, Computer Methods and Programs in Biomedicine, 130 (2016) 22-30.

[48] M. P. Beck, T. Sun, A. S. Teja, The thermal conductivity of alumina nanoparticles dispersed in ethylene glycol, Fluid Phase Equilibria, 260 (2007), 275-278.

[49] S. Simpson, A. Schelfhout, C. Golden, S. Vafaei, Nanofluid thermal Conductivity and Effect Parameters, Appli. Sci, 9(1) (2019) 87.

[50] R. Saidur, K.Y. Leong. H.A. Mohammad, A review on applications and challenges of nanofluids, Renewabl and sustainable energy review, 15 (2011) 1646-1668.

[51] Wang XQ, Mujumdar AS. Review on nanofluids. Part II: experiments and applications. Braz J Chem Eng 2008;25 (October–December (04)):631–48.

[52] I. Zaaroura, M.Toubal, H. Reda, J. Carlier, S. Harmand, R. Boukherroub, A. Fasquelle, B. Nongaillard "Evaporation of nanofluid sessile drops: Infrared and acoustic methods to track the dynamic deposition of copper oxide nanoparticles", Int. J. Heat Mass Transfer 127, Part B (2018) 1168-1177.

[53] J. Lee, I. Mudawar, Assessment of the effectiveness of nanofluids for single-phase and two-phase heat transfer in micro-channels, Int. J. Heat Mass Transfer, 50 (2007) 452-463.

[54] Routbort, J., Argonne National Lab, Michellin North America, St. Gobain Corp., (2009).

[55] Han, Z. H., Cao, F. Y., and Yang, B. , "Synthesis and thermal characterization of phase-changeable indium/polyalphaolefin nanofluids," Applied Physics Letters, vol. 92, no. 24, 3, (2008).

[56] H. Peng, G. Ding, W. Jiang, H.Hu, Y.Gao, Heat transfer characteristics of refrigerant-based nanofluid flow boiling inside a horizontal smooth tube, Physics, (2009).

[57] V. Vasu, K. R. Krishna, A.C.S. Kumar, Materials Heat transfer with nanofluids for electronic cooling, Science (2009).

[58] Young, T. (1805). An essay on the cohesion of fluids. Philosophical Transactions of the Royal Society of London, 95, 65-87.

[59] Contact Angle 2017 Wikipedia.
https://en.wikipedia.org/w/index.php?title=Contact_angle&oldid=809158542, accessed November 24, 2017.

[60] M. Kaya, Experimental Study on Active Cooling Systems Used for Thermal Management of High-Power Multichip Light-Emitting Diodes, volume (2014) ID 563805.

[61] Marangoni, C. (1865). Sull'espansione delle goccie d'un liquido galleggianti sulla superfice di altro liquido.

[62] Hendarto, E., & Gianchandani, Y. B. (2013). Size sorting of floating spheres based on Marangoni forces in evaporating droplets. Journal of Micromechanics and Microengineering, 23(7), 075016.

[63] Savino, R., & Fico, S. (2004). Transient Marangoni convection in hanging evaporating drops. Physics of Fluids, 16(10), 3738-3754.

[64] Buffone, C., & Sefiane, K. (2004). Investigation of thermocapillary convective patterns and their role in the enhancement of evaporation from pores. International Journal of Multiphase Flow, 30(9), 1071-1091

[65] Y. Zhao, B. Zou, C. Li, Y. Ding, Active cooling based battery thermal management using composite phase change materials, Energy Procedia, 158 (2019), 4933-4940.

[66] Amrid MAMMERI "Improving the energy performance of industrial cooling systems: Application to computer servers", doctoral thesis, Institut de Technologie de Paris, June 2014.

[67] Hasna Souahlia (LUCAS), Sébastien Yon (AREELIS Technologies), "Heat dissipation in electronic components / systems", July 2015.

[68] H. Auracher, M. Buchholz, Experiments on the fundamental mechanisms of boiling heat transfer, J. Braz. Soc. Mech. Sci. & Eng, 27 (2005).

[69] Y. Zhang, A. Faghri, Advances and Unsolved Issues in Pulsating Heat Pipes, Heat transfer Engineering, 29 (2008).

[70] H. Joujara, A. Chauhan, T. Nannou, S. Almahmoud, B. Delpech, L.C. Wrobelm Heat pipe based systems - Advances and applications, Energy, 128 (2017), 729-754.

[71] Benjamin Siedel. Analysis of heat transfer and flow patterns in a loop heat pipe: Modelling byanalytical and numerical approaches and experimental observations. Other [cond-mat.other]. INSAde Lyon, 2014. English. NNT: 2014ISAL0092.

[72] T.P. Cotter, Principles and prospects for micro heat pipes, Conference: 5. international heat pipe conference, Tsukuba, Ibaraki, Japan, 14 May 1984.

[73] E. Pouzet, J.-L. Joly, V. Platel, J.-Y. Grandpeix, C. Butto, Dynamic response of a capillary pumped loop subjected to various heat load transients, International Journal of Heat and Mass Transfer 47 (10) (2004) 2293-2316.

[74] C. ROMESTANT, "Theoretical and experimental studies of heat pipes and thermo siphons subjected to strong accelerations", Doctoral thesis, University of Potters, November (2000).

[75]M. Shafahi, V. Bianco, K. Vafai, O. Manca, An investigation of the thermal performance of cylindrical heat pipes using nanofluids, Int. J. Heat Mass Transfer 53 (1–3) (2010) 376–383.

[76] M. Shafahi, V. Bianco, K. Vafai, O. Manca, Thermal performance of flat-shaped heat pipes using nanofluids, Int. J. Heat Mass Transfer 53 (7–8) (2010) 1438–1445.

[77] K. Vafai, W. Wang, Analysis of flow and heat transfer characteristics of an asymmetrical flat plate heat pipe, Int. J. Heat Mass Transfer 35 (9) (1992)2087–2099.

[78] K. Vafai, N. Zhu, W. Wang, Analysis of asymmetric disk-shaped and flat-plate heat pipes, J. Heat Transfer 117 (1) (1995) 209–218.

[79] Y. Wang, K. Vafai, Transient characterization of flat plate heat pipes during startup and shut down operations, Int. J. Heat Mass Transfer 43 (15) (2000)2641–2655.

[80] Y. Wang, K. Vafai, An experimental investigation of the thermal performance of an asymmetrical flat plate heat pipe, Int. J. Heat Mass Transfer 43 (15) (2000)2657–2668.

[81] Y. Wang, K. Vafai, An experimental investigation of the transient characteristics on a flat-plate heat pipe during startup and shut down operations, J. Heat Transfer 122 (3) (2000) 525–535.

[82] X.F. Yang et al., Heat transfer performance of a horizontal micro-grooved heat pipe using CuO nanofluid, J. Micromech. Microeng. 18 (3) (2008) 035038.

[83] N. Zhu, K. Vafai, The effects of liquid–vapor coupling and non-Darcian transport on asymmetrical disk-shaped heat pipes, Int. J. Heat Mass Transfer39 (10) (1996) 2095–2113.

[84] N. Zhu, K. Vafai, Numerical and analytical investigation of vapor flow in a disk-shaped heat pipe incorporating secondary flow, Int. J. Heat Mass Transfer 40(12) (1997) 2887–2900.

[85] A. Faghri, Heat Pipe Science and Technology, Taylor & Francis, 1995.

[86] J.M. Tournier, M.S. El-Genk, A heat pipe transient analysis model, Int. J. Heat Mass Transfer 37 (5) (1994) 753–762.

[87] W.S. Chang, G.T. Colwell, Mathematical modeling of the transient operating characteristics of a low-temperature heat pipe, Numer. Heat Transfer 8 (2)(1985) 169–186.

[88] S.-Q. Zhou, R. Ni, Measurement of the specific heat capacity of water-basedAl2O3nanofluid, Appl. Phys. Lett. 92 (9) (2008) 093123.

[89] S.U.S. Choi, J.A. Eastman, Enhancing thermal conductivity of fluids with nanoparticles.

[90] B.C. Pak, Y.I. Cho, Hydrodynamic and heat transfer study of dispersed fluids with submicron metallic oxide particles, Exp. Heat Transfer 11 (2) (1998) 151–170.

[91] H.C. Brinkman, The viscosity of concentrated suspensions and solutions, J.Chem. Phys. 20 (4) (1952) 571.

[92] Z.-h. Liu, J.-g. Xiong, R. Bao, Boiling heat transfer characteristics of nanofluids in a flat heat pipe evaporator with micro-grooved heating surface, Int. J.Multiphase Flow 33 (12) (2007) 1284–1295.

[93] R.R. Rieh l, Analysis of loop heat pipe behavior using nanofluid, in: Heat Powered Cycles International Conference (HPC), New Castle, UK, Paper 06102, (2006).

[94] P. Gunnasegaran, M. Z. Abdullah, M. Z. Yusoff, Effect of Al_2O_3-H_2O nanofluid concentration on heat transfer in a loop heat pipe, Procedia Materials science 5 (2014) 137-146 .

[95] K. Alizard, K. Vafai, M. Shafahi, Thermal performance and operational attributes of the startup characteristics of flat-shaped heat pipes using nanofluids, Int. J. Heat Mass Transfer 55 (2012)140-155.

[96] Y. F. Niu, W. L. Zhao, Y. Y. Gong, Experimental investigation of thermal performance of miniature heat pipe using SiO_2-water nanofluids, J. Nanosci. Nanotechnol, 15 (2015) 2932-2938.

[97] W. Yu, H. Xie, A Review on Nanofluids: Preparation and Stability, Mechanisms and Applications, *J. Nanomater.* **(2011)**, 435873, 1-17.

[98] M. He, H. Qiu, Internal Flow Patterns of an Evaporating Multicomponent Droplet on a Flat Surface, *Int. J. Thermal Sci.* 100 **(2016)** 10-19.

[99] P. Chen, M. Toubal, J. Carlier, S. Harmand, B. Nongaillard, M. Bigerelle, Evaporation of Binary Sessile Drops: Infrared and Acoustic Methods, *Langmuir* 32 **(2016)** 9836-9845.

[100] Y. Deblock, P. Campistron, M. Lippert, and C. Bruneel, Electrical characterization of plate piezoelectric transducers bonded to a finite substrate. Acoustical Society of America, Vol. 111, No. 6, June 2002.

[101] L. Korson, W. Drost-Hansen, F. J. Millero, Viscosity of water at various temperatures, J. Phys. Chem. 73 (1969) 34-39.

[102] E.E. Franco, J.C. Adamowski, R.T. Higuti, F. Buiochi, Experimental Study of the Complex Reflection Coefficient of Shear, *Phys. Procedia.* 3(1) **(2010)** 803-809.

[103] N. Bilaniuk, G.S.K. Wong, Speed of Sound in Pure Water as a Function of Temperature, *J. Acoust. Soc. Am.* 93(3) **(1993)** 1609-1612.

[104] S.P. Nikanorov, Y.A. Burenkov, A.V. Stepanov, Elastic Properties of Silicon, *Sov. Phys. Solid State*. 13 **(1972)** 2516-2518.

[105] C.V. Nielsen, W. Zhang, L.M. Alyes, N. Bay, P. Martins, Modeling of Thermo-Electro-Mechanical Manufacturing Processes, *Springer-Verlag; London, UK*, **(2013)** 1-120.

[106] E.S. Palencia, A. Zaoui, Homogenization Techniques for Composite Media, *Lecture Notes in Pysics, Springer-Verlag: Udine, Italy,* 272 (**1987)** 226–230.

[107] E.P. Sanchez, Non Homogeneous Media and Vibration Theory, *Lecture Notes in Physics. Springer*: Berlin, Germany 127 **(1980)** 84–128.

[108] D. Begis, A. Bestango, G. Duvaut, A. Hassim, M. Nuc, A New Method of Computing Global Elastic Moduli for Composite Materials, *RR-0195, INRIA.* **(1983)**, <inria-00076363>

[109] M. Trempaa, C. Reimannab, J. Friedrichab, G. Müllera, D. Oriwolc, Mono-crystalline growth in directional solidification of silicon with different orientation and splitting of seed crystals, J. Cryst. Growth 351 (2012) 131-140; https://doi.org/10.1016/j.jcrysgro.2012.04.035

[110] S.P. Nikanorov, Y.A. Burenkov, A.V. Stepanov, Elastic properties of silicon, Sov. Phys. Solid State. 13 (1972) 2516–2518.

[111] I. Zaaroura, S. Harmand, J. Carlier, M. Toubal, A. Fasquelle, B. Nongaillard, Experimental studies on evaporation kinetics of gold nanofluid droplets: Influence of nanoparticle sizes and coating on thermal performance, Appl. Therm. Eng., 183 (2021) 116180.

[112] S. Takayanagi, T. Yanagitani, M. Matsukawa. Wideband Multimode Transducer Consisting of c-Axis Tilted ZnO/c-Axis Normal ZnO Multilayer. Japanese Journal of Applied Physics **51** (July 2012).

[113] L. Korson, W. Drost-Hansen, F. J. Millero, Viscosity of water at various temperatures, J. Phys. Chem. 73 (1969) 34-39; DOI: 10.1021/j100721a006

[114] R. A. Horne, D. S. Johnson, The Viscosity of Water under Pressure, J. Phys. Chem. 70 (1966) 2182-2190; DOI: 10.1021/j100879a018.

[115] S. Breisch, B.D. Heij, M. Lohr, M. Stelzle, Selective Chemical Surface Modification of Fluidic Microsystems and Characterization Studies, J. Micromech. Microeng. 14 **(2004)** 497-505.

[116] S. Li, J. Carlier, M. Toubal, H. Liu, P. Campistron, D. Callens; G. Nassar, B. Nongaillard, S. Guo, High Frequency Acoustic on-Chip Integration for Particle Characterization and Manipulation in Microfluidics. Appl. Phys. Lett. 111 (2017) 163503.

[117] S. Chandra, M. di Marzo, Y. M. Qiao and P. Tartarini, Effect of Liquid-Solid Angle on Droplet Evaporation, Fire Safty Journal 27 (1996) 141-158.

[118] P. Chen, S. Harmand, S. Ouenzerfi, J. Schiffler, Marangoni Flow Induced Evaporation Enhancement on Binary Sessile Drops, J. Phys. Chem, B, 121(23) (2017) 5824-5834.

[119] R. J. Moffat, Describing the uncertainties in experimental results, Experimental Thermal and Fluid Science 1 (1) (1988) 3-17.

[120] R. Boubaker, S. Harmand, V. Platel, Experimental study of the liquid/vapor phase change in a porous media of two-phase heat transfer devices, Appl. Therm. Eng, 143 (2018) 275-282.

[121] R. Boubaker, V. Platel, Vapor pocket behavior inside the porous wick of a capillary pumped Loop for terrestrial application, Applied Thermal Engineering 84 (2015) 420-428.

[122] C. Ren, Q.S. Wu, M.B. Hu, Heat transfer with flow and evaporation in loop heat pipes wick at low or moderate heat fluxes, Int. J. Heat Mass Transfer 50 (11) (2007) 2296-2308.

[123] P. Chen, S. Harmand, S. Ouenzerfi, J. Schiffler, Marangoni Flow Induced Evaporation Enhancement on Binary Sessile Drops, J. Phys. Chem, B, 121(23) (2017) 5824-5834.

[124] A. V. Mudryi, A. V. Ivaniukovich, A. G. Ulyashin, Deposition by magnetron sputtering and characterization of indium tin oxide thin films, Thin Solid Films, (2007), 515, 6489-6492.

[125] Madding, R.P. Emissivity measurement and temperature correction accuracy considerations. 1999.

[126] Kuo, L. S., and Qiu, T., 1996, "Microscale Energy Transfer During Picosecond Laser Melting of Metal Films," ASME National Heat Transfer Conference,Vol. 1, pp. 149–157.

[127] J. Safarov, B. Ahmadov, S. Mirzayev, A. Shahverdiyev, E. Hassel, Thermophysical properties of 1-butanol over a wide range of temperatures and pressures up to 200Mps, Journal of Molecular Liquids, (2015) 209, 465-479.

[128] Engineering ToolBox, (2003). Convective Heat Transfer. [online] Available at: https://www.engineeringtoolbox.com/convective-heat-transfer-d_430.html [Accessed 2 3. 2019].

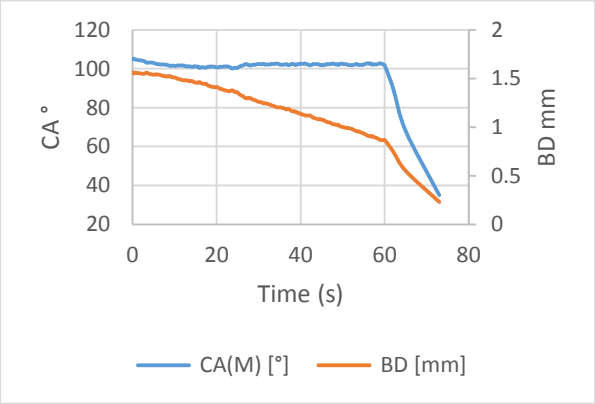
[129] E. Sadeghl. N. Djllall, M. Bahrami, Estimation of Nusselt number in microchannels of arbitrary cross-section with constant axial heat flux, Heat Transfer Engineering (2010),

[130] K.C. Leong, C. Yang, S.M.S. Murshed, A model for the thermal conductivity of nanofluids-the effect of interfacial layer, J. Nanoparticle Res., 8 (2) (2006), pp. 245-254.

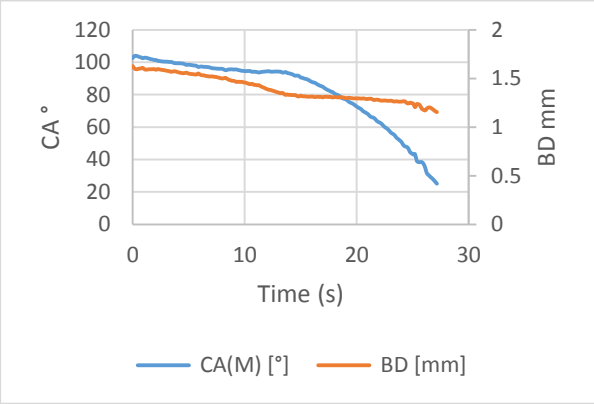
ANNEX A

1- Volume and wetting base diameter evolutions during droplets evaporation of pure water and uncapped gold nanofluid-PBS (5 and 10 nm).

a- 5 nm gold nanoparticle

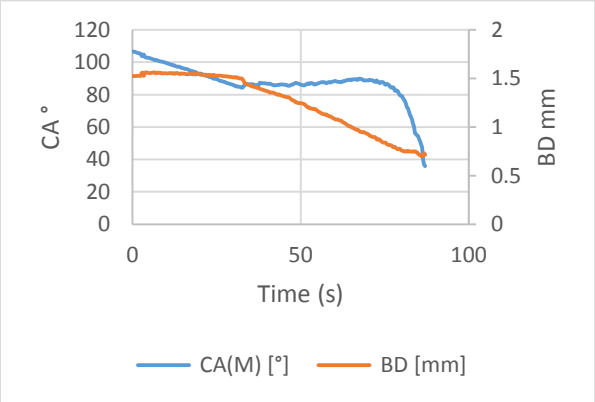


(b) T_s = 55 °C

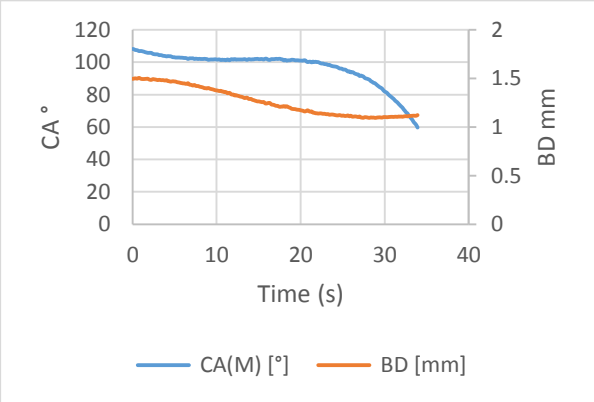


(a) T_s = 77 °C T_s

b- 10 nm gold nanoparticle

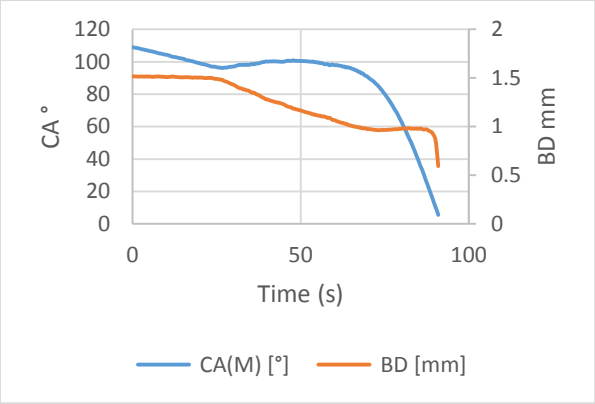


(a) T_s = 55 °C

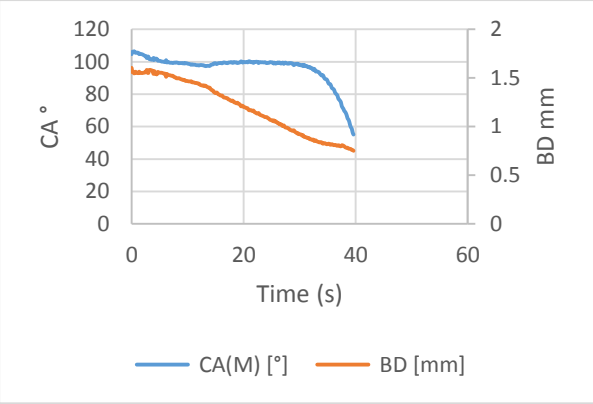


(b) T_s = 77 °C

c- Water droplet



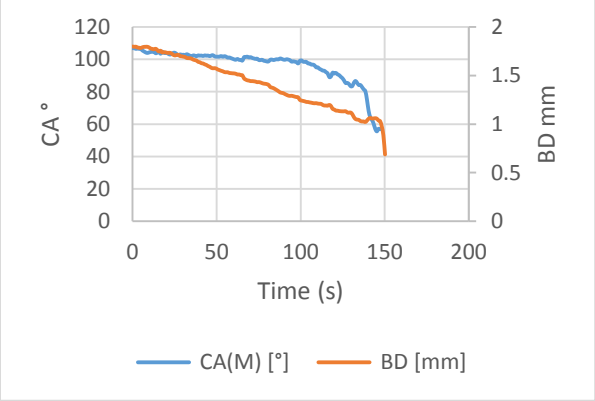
(a) T_s = 55 °C



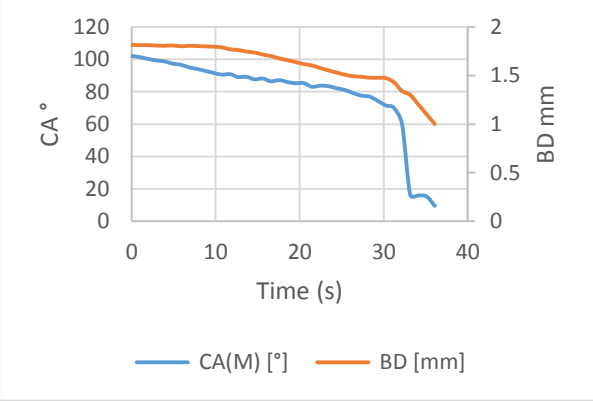
(b) T_s = 77 °C

2- Volume and wetting base diameter evolutions during droplets evaporation of pure water and citrate-capped gold nanofluid-PBS (5 and 10 nm).

a- Pure water

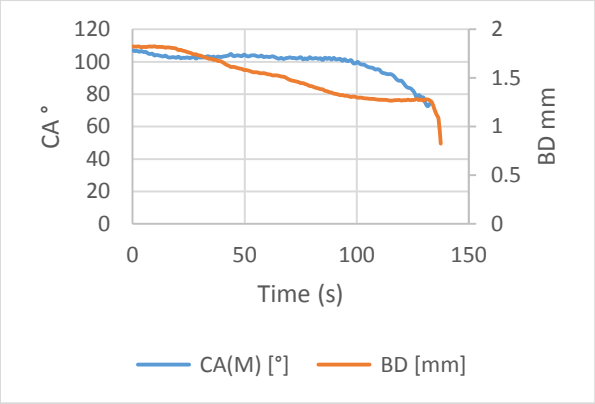


(b) T_s = 55 °C

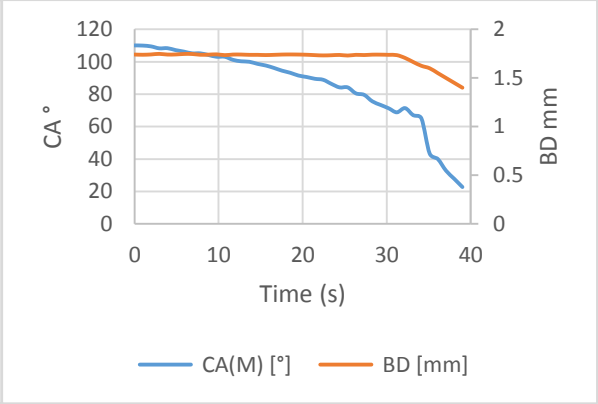


(a) T_s = 77 °C

b- 2 nm gold nanoparticle

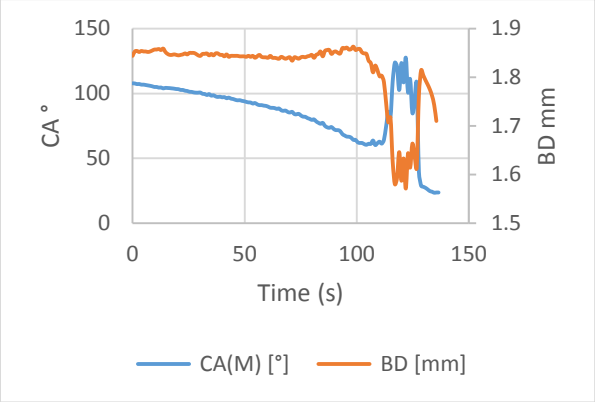


(a) T_s = 55 °C

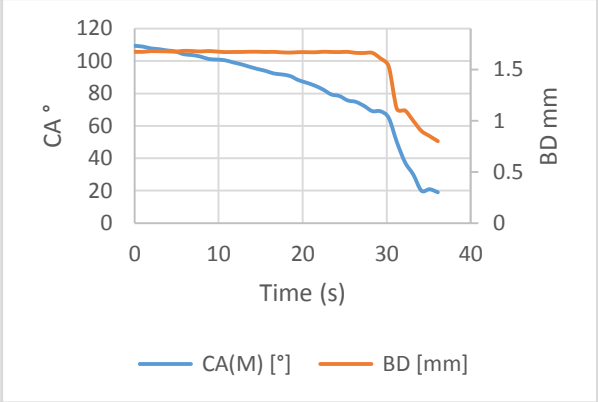


(b) T_s = 77 °C

c- 5 nm gold nanoparticle

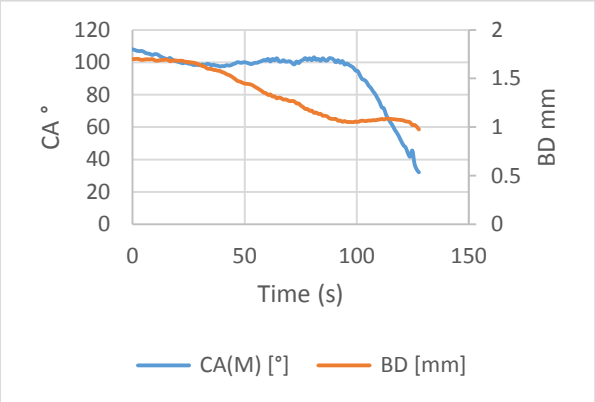


(a) T_s = 55 °C

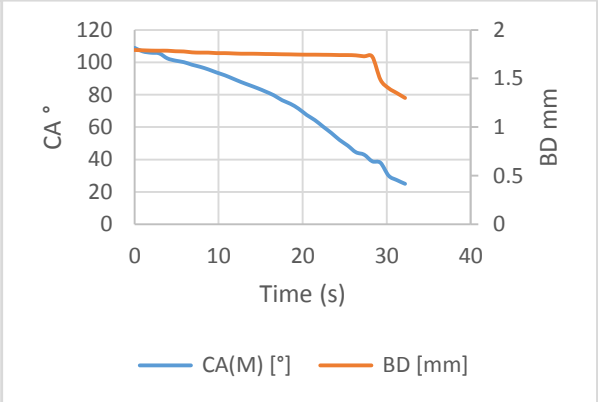


(b) T_s = 77 °C

d- 10 nm gold nanoparticle



(a) T_s = 55 °C



(b) T_s = 77 °C

ANNEX B

Repeatability at 77 °C surface temperature.

1- Pure water

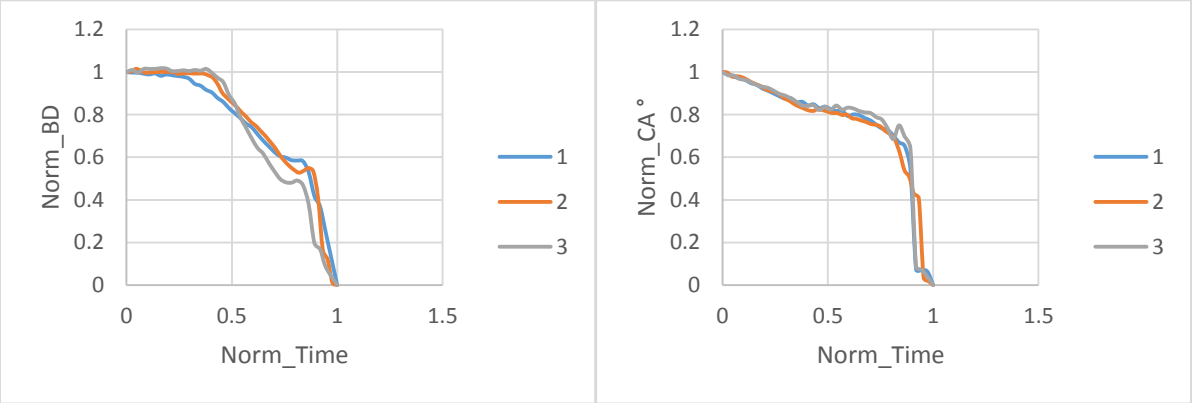


Figure 1. The repeatability of the Contact angle and base diameter variations of pure water droplet at 77 °C surface temperature.

2- 2 nm Citrate-PBS gold nanofluid.

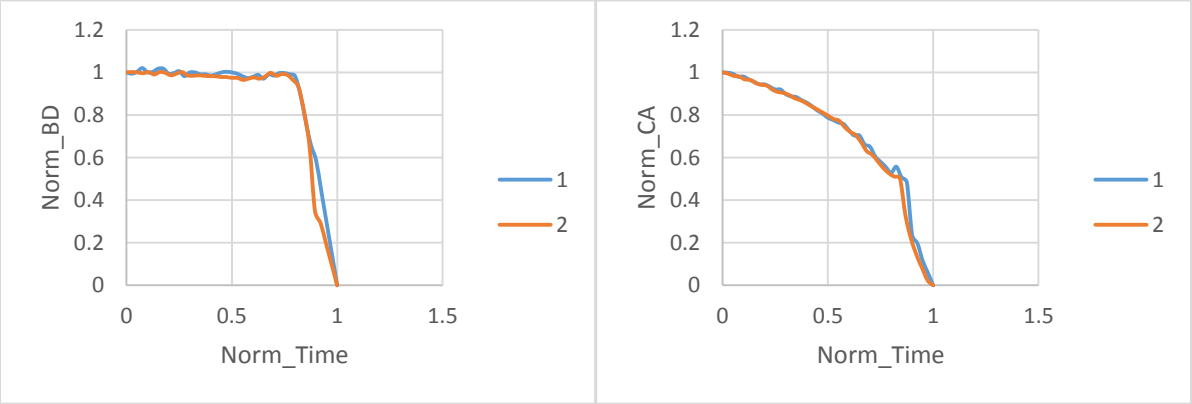


Figure 2. The repeatability of the contact angle and base diameter variations of 2nm citrate-PBS gold/ water droplet at 77 °C surface temperature.

3- 5 nm Citrate-PBS gold nanofluid.

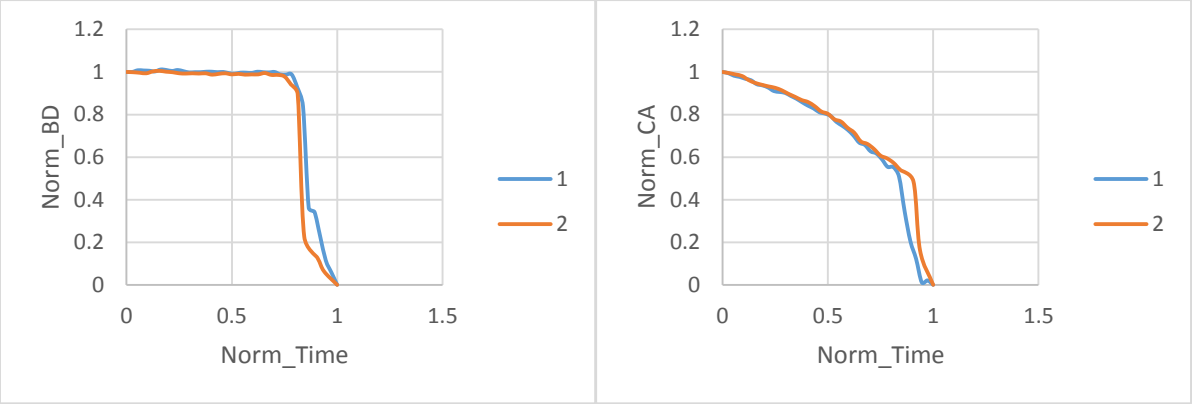


Figure 3. The repeatability of the contact angle and base diameter variations of 5nm citrate-PBS gold/ water droplet at 77 °C surface temperature.

4- 10 nm Citrate-PBS gold nanofluid.

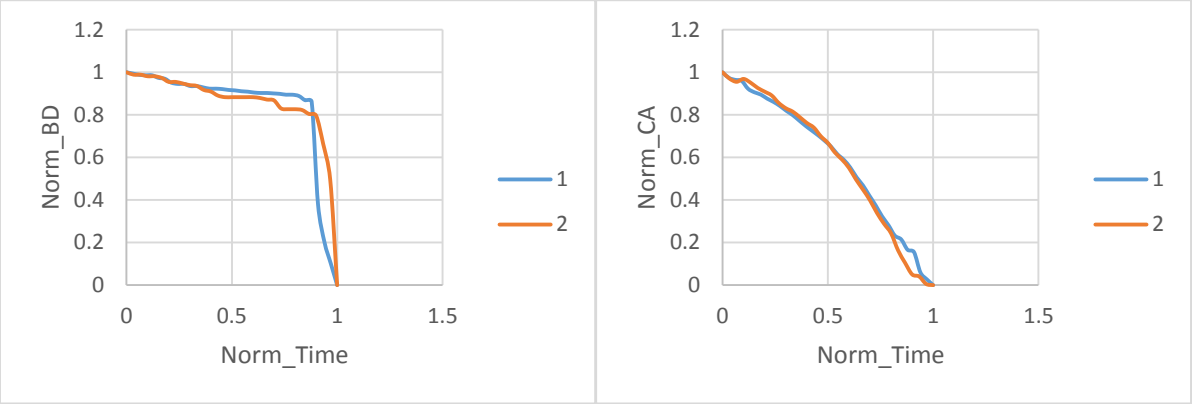


Figure 4. The repeatability of the contact angle and base diameter variations of 10nm citrate-PBS gold/ water droplet at 77 °C surface temperature.

ANNEX C



System Overview	SC7210-7500 / SC7300
Waveband	MW
Sensor type	InSb / MCT
Pixel Resolution	320x256
Pixel Pitch	30µm
Spectral ranges	1.5 - 5.1 µm for InSb (BB)
Measurement	
NETD	<20mK for InSb
Standard Camera Calibration Range	5ºC to 300ºC for InSb
Optional Camera Calibration Range	-20°C to 300ºC
Digital Full Frame rate	InSb: 190 Hz - 380 Hz full frame up to 3 kHz - 39.8 kHz with windowing

Figure 5. Technical FLIR specification (for Two-phase heat transfer device analysis).

FLIR X-Series

High-end cameras with 640x512 resolution stirling-cooled sensors for non-destructive testing and process control of very fast processes.



Product properties

640x512 pixel The X6000sc-Series have a high resolution 640x512 detector that provides outstanding image accuracy.
High-Speed-IR-Windowing The FLIR X-Series features a high-speed windowing mode for recording speeds of up to a few kHz.
Camera synchronization for real-time processing with digital I / O and image markers.
Analog value acquisition with image-synchronous mapping for real-time acquisition of external measurements.
Analog value output with image-synchronous mapping for control of external processes.
Extremely high sensitivity < 20 mK for finest image details and capturing of smallest temperature differences.
Display on the camera for easy operation and adjustment.
GigE Vision™ standard for data transfer over long distances and to laptops.
CamLink™ interface for robust industry-standard data transfer.

High-resolution infrared cameras with sensitive quantum detectors.

Figure 6. Technical FLIR specification (for Microchannel analysis).

List of Publications:

A- Journal Publications:

1- Experimental studies on evaporation kinetics of gold nanofluid droplets: Influence of nanoparticle sizes and coating on thermal performance, Appl. Therm. Eng., 183 (**IF 4.725 Q1**) **(2021)** 116180. **I. Zaaroura**, S. Harmand, J. Carlier, M. Toubal, A. Fasquelle, B. Nongaillard.

2- Evaporation of nanofluids sessile drops: Infrared and acoustic methods to track the dynamic deposition of copper oxide nanoparticles. Aug **(2018),** International Journal of Heat and Mass Transfer (**IF 4.947 Q1**) **(2018)**. **I. Zaaroura**, M. Toubal, H. Reda, J. Carlier, S. Harmand, R. Boukherroub, A. Fasquelle, B. Nongaillard.

3- Modeling and prediction of the dynamic viscosity of nanofluids by a homogenization method. The European Physical Journal Plus **(2020) (Under review)** (**IF 3.228 Q1**) **(2020) I. Zaaroura**, H. Reda, F. Lefebvre, J. Carlier, M. Toubal, S. Harmand, B. Nongaillard, H. Lakiss.

4- Experimental and numerical study of the surface tension impact on the capillary liquid bridge evolution during the coalescence of a pendant and a sessile water drop submerging in another viscous fluid. Langmuir **(2020)** (**Under review**) (**IF 3.863 Q1**). M. Brik, S. Harmand, **I. Zaaroura**, A. Saboni.

5- Study and favor longitudinal and shear modes of high frequency ZnO Piezoelectric transducers. Application of viscosity measurement using ultrasound. Advances in Science, Technology and Engineering Systems Journal **(2020) (Accepted)** H. Dahmani, **I. Zaaroura**, A. Salhab, P. Campistron, J. Carlier, M. Toubal, B. Nongaillard.

B- International Conferences:

1. Evaporation of Gold Nanofluids Sessile Drops on Heated Substrate. Jun (2019), TechConnect World Innovation Conference and Expo in Boston, United States, USA. **I. Zaaroura**, S. Harmand, J. Carlier, R. Boukherroub. **(2019)**

2. Study of a dual longitudinal and shear acoustic wave ZnO transducer in the gigahertz frequency range: Application to viscosity measurement and first step for device integration. May (2019), International Conference on Design and Test of Integrated Micro and Nano-systems In Gammarth, Tunisia (**Best Presentation Award**). H. Dahmani, **I. Zaaroura**, P. Campistron, J. Carlier, M. Toubal, B. Nongaillard. **(2019)**

C- To be submitted (In Journals):

1. Thermal performance of self-rewetting gold nanofluids: Application to two-phase heat transfer devices. **I. Zaaroura**, S. Harmand, J. Carlier, M. Toubal, A. Fasquelle, B. Nongaillard.
2. Online shear viscosity measurements of gold nanofluids: using a high frequency acoustic method and compared to a finite element model, **I. Zaaroura**, H. Reda, J. Carlier, M. Toubal, S. Harmand, B. Nongaillard.

3. Numerical study for the impact of the pendant drop radius on the initial stage of the surface tension driven coalescence in liquid-liquid systems. M. Brik, S. Harmand, **I. Zaaroura**, A. Saboni.